Università degli Studi di Napoli Federico II

DOTTORATO DI RICERCA IN

FISICA

Ciclo XXXVI

Coordinatore: prof. Vincenzo Canale

Characterization of EJ-309 organic liquid scintillators for the SHADES experiment

Settore Scientifico Disciplinare FIS/04

Dottorando
Chemseddine ANANNA

Tutors
Proff. Gianluca IMBRIANI
Andreas BEST

Anni 2021/2023

Abstract

This thesis belongs to the direct experimental measurement of the astrophysically significant ^{22}Ne(α,n)^{25}Mg nuclear reaction framework. Improving the state-of-the-art results requires overcoming several technical challenges such as the background activity of the detectors and the low cross-section of the reaction. The present work contributes to this by performing a full characterization of EJ-309 organic liquid scintillators used in the SHADES experimental setup in preparation for the reaction measurement with the newly commissioned LUNA-MV accelerator, located at the deep-underground facility of Laboratori Nazionali del Gran Sasso (AQ), Italy. The characterization procedure starts by gain matching the 12 EJ-309 liquid scintillators of the detection array, then identifying and quantifying the internal background of each. A full study of the detectors response to γ, α, and neutrons is conducted, establishing light-output-to-energy calibration for each particle type. The internal activity of the detectors is quantified by placing the liquid scintillators under 5 cm of lead inside the underground facility in August 2021. The collected data showed the typical ^{238}U α-activity in the detectors' walls. Time coincidence analysis confirmed its origin, incidentally providing a new estimate of ^{214}Po half-life. A Monte-Carlo simulation allowed explain the contamination scenario and quantify ^{238}U/^{232}Th decay chains' contribution to the observed activity. This result is to be used after the ^{22}Ne(α,n)^{25}Mg measurement to exclude α-counts, indistinguishable from neutrons in the scintillators. A neutron energy calibration adapted to the ^{22}Ne(α,n)^{25}Mg measurement (i.e. optimized for low energies) is established in this work. It is a result of a series of neutron beam measurements performed at the Goethe University of Frankfurt Germany in July 2022, using a simplified array of 1 scintillator and 6 ^{3}He counters. Including the counters allowed the investigation of efficiency improvement through active shielding using coincidence information between the two detector types, preparing the ground for the ^{22}Ne(α,n)^{25}Mg measurement.

This work is organized such as Chapter 1 describes the ^{22}Ne(α,n)^{25}Mg astrophysical scenario, providing insights on stellar evolution and AGB stars. Following, the reaction's state-of-the-art is reported, focusing on the experimental challenges hindering the measurement of its cross-section. Chapter 2 then describes the SHADES experimental setup, discussing neutron detection with EJ-309 scintillators and ^{3}He counters. Chapter 3 reports the experimental procedure followed to gain match the scintillators and achieve a high level of particle-type separation between neutrons and γ-rays through optimized Pulse Shape Discrimination (PSD). The internal background of the scintillators and the environmental background at the underground facility are investigated in Chapter 4, reporting the different means and techniques used to achieve it, noticeably the PSD optimization discussed in the previous chapter. Chapter 5 is dedicated to the Frankfurt measurement, discussing data acquisition and analysis methodology while also presenting the PSD and calibration results. The last part of Chapter 5 is an investigation of the active shielding performance and its direct and indirect impacts on the SHADES experiment.

Dedication

In memory of my deceased parents.

Acknowledgements

Contents

Table of Acronyms

Notation	Description
H-R	Hertzsprung-Russell.
AGB	Asymptotic Giant Branch star.
TP-AGB	Thermally Pulsing AGB star.
ToF	Time-of-flight.
AmBe	Americium-Berylium.
PSD	Pulse Shape Discrimination.
SHADES	Scintillator-^{3}He Array for Deep-underground s-process experiment.
ChETEC-INFRA	Chemical Elements as Tracers of the Evolution of the Cosmos Infrastructures for Nuclear Astrophysics.
FoM	Figure of Merit.
LNGS	Laboratori Nazionali del Gran Sasso.
VdG	Van de Graaff accelerator.

List of Figures

List of Tables

Introduction

Humans have, since ancient times, been intrigued by the sky and objects populating it. The perpetual quest to find a satisfying explanation regarding their nature, movement, and the way they came to existence led to the emergence of many scientific research fields of which nuclear astrophysics is a natural outcome. We may attribute its kick-starting to the year 1938 when Bethe and Critchfield [1] demonstrated that the hydrogen fusion mechanism, earlier proposed by Eddington, is compatible with the energy generation in the sun. Since many other reactions have been investigated as possible stellar energy sources leading to the discovery of the CNO cycle (1938/39), triple-αcapture (1952) alongside many other nucleosynthesis mechanisms occurring in different types of stars. It has then been proven that the majority of elements present in our universe are formed in stars, either during their lifetime or at the end of it. Nevertheless, explaining the disparities in their observed abundances in our solar system, thoroughly described in [2] and[3], highlights the influence of the neutron number present in the nuclei, improving the nuclear shell model[4] and the discovery of the neutron capture processes known as s and r processes.

To compare the results of the theoretical nucleosynthesis models with metallicity/isotopic observations done on actual stars, the production rates of each reaction should be known with as much precision as possible. The most straightforward way to obtain those values is through the direct reproduction and measurement of the nuclear reaction in a controlled laboratory environment. The usually lighter "projectile" particles like protons, neutrons, or α-particles are brought to the necessary energies using particle accelerators, then directed towards the "target" particle. That said, the extremely low probability of such capture reactions occurring in the astrophysical relevant low energy window makes such measurements very challenging from a technical point of view. Considerable means are necessary to build an adequate detection setup with sufficient sensitivity. In most cases, the background signals are indistinguishable from the actual reaction products requiring increasingly ingenious shielding and suppression techniques. This work focuses on the particularly important ^{22}Ne$(\alpha,$n$)^{25}$Mg stellar nuclear reaction measurement through the accomplishment of a full characterization of EJ-309 organic liquid scintillators[1]. A key component of SHADES[2] experimental setup[5] set to measure this reaction using the LUNA-MV accelerator facility[6] in the deep-underground facility of the Laboratori Nazionali Del Gran Sasso (LNGS), Italy. It covers the gain matching of the whole array, the identification and quantification of both internal and background activity as well as a full study of the detectors' response to γ, α, and neutrons providing an adequate light to energy calibration for each. The first chapter is an overview of stellar evolution and the way it is approached by modern science. A particular focus

---

[1]Scionix 127A127/5M-EJ309-E1-X2-NEG, 127 Œ 127 mm2 with 10 stage ETL9390 photomultiplier

[2]Scintillator-^{3}He Array for Deep-underground Experiments on the S-process, ERC-StG 2019 #852016

is then put on the ^{22}Ne(α,n)^{25}Mg reaction followed by a discussion on the limitations challenging its experimental reproduction in the lab and the current state of the art of its measurement. The second chapter is dedicated to neutron detection, detailing the functioning of EJ-309 scintillators and ^{3}He proportional counters used in the SHADES detection array. The internal background of the scintillators and the environmental background of the facility are investigated in chapter 4 relating the different means and techniques used to achieve it. An important measurement for the neutron response study of the array was performed at the Goethe University of Frankfurt - Germany. Chapter 5 summarizes the experimental measurement proceeding and the methodology used to analyze the collected data. The last part of the chapter is a full investigation of the scintillators-^{3}He counters time coincidence analysis and its use as an active shielding. The main findings of this work are then summarised in the last chapter dedicated to the results and their direct and indirect impacts on the SHADES final measurement.

Chapter 1

Overview on stellar evolution

Throughout their existence, stars undergo many phases in which different physical phenomena take place. They first start forming when gravitational contraction condenses an unstable original cloud of gas and dust. Pressure and temperature increase within this latter until the *Jean instability criterion* is met, i.e. when the gravitational energy surpasses the thermal energy of its composing molecules as follows :

$$G \cdot \frac{M^2}{R} \geq \frac{3}{2} \cdot kT \cdot \frac{M}{m} \tag{1.0.1}$$

where G is the gravitational constant, M is the total mass of the cloud, R is the radius, T is the temperature, and m is the mean molecular weight. The initial cloud, now a protostar, shrinks increasing its density and opacity, while the generated excess heat is radiated away from the external surface. This energy loss dictates the rate at which the contraction occurs until an equilibrium is reached (i.e. the released energy is equal to the stored internal one) following the *Virial theorem*. During this stage, the evolution is characterized by an increase in the temperature of the star without a significant variation in its luminosity (see Figure 1.1). It is soon followed by the so-called Hayashi contraction phase where the star approaches the main sequence following a path determined by its mass [7, 8, 9, 10, 11]. When the core temperature reaches around 1 to 2×10^7 K, thermonuclear reactions ignite between the cloud's main -and the lightest- components (i.e. hydrogen) producing the next heaviest element (i.e. helium). This releases large amounts of energy thus sustaining the star, preventing it from collapsing on itself because of gravitation forces. This phase, called "hydrogen burning", is where stars usually spend the majority of their lifetime. In the H-R diagram (Figure 1.1), it is represented by the long diagonal region called "Main sequence", where the majority of currently observed stars belong. Depending on the initial conditions leading to their formation, stars from the main sequence may have different masses and produce different luminosities (light and heat emission rates). The non-equally proportional relation between the two quantities ($\frac{L}{L_\odot} \simeq 10^4$ when $\frac{M}{M_\odot} = 10$) implies that heavier stars burn their hydrogen much faster, thus having shorter lifespans. At the end of the central hydrogen burning, temperatures sufficient to continue combustion in other areas of the star can be reached. Due to these active shells, the star is clearly divided in two: the central part (core) begins to contract to reach combustion temperatures of helium and the external part (envelope) expands beyond the shell. The effect of these two events provokes the expansion of the stellar radius causing an increase in brightness, and a decrease in effective temperature. Its luminosity heavily increases, moving it to the up-right
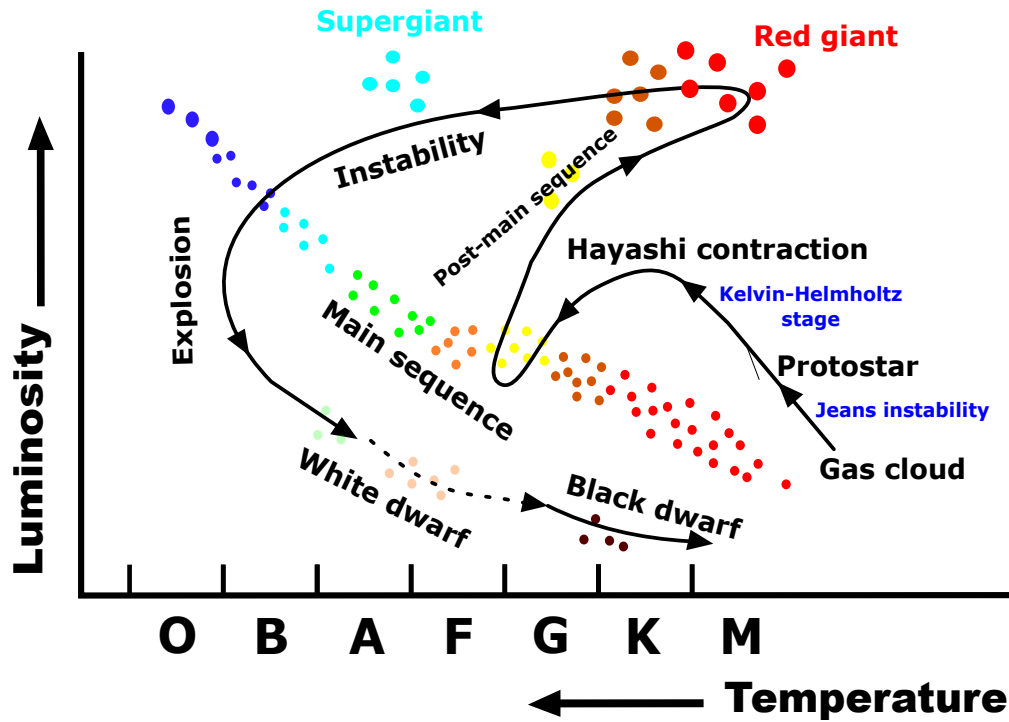
Figure 1.1: Hertzsprung - Russell diagram for a 1 $M_\odot$ star life cycle.

region of the H-R diagram, and becoming what is called a red giant (see Figure 1.1). If the star's mass is comprised between 0.5 and 2.4 $M_\odot$, the conditions for helium burning cannot be met in a non-degenerate environment. The central temperature keeps therefore increasing until the helium burning is ignited explosively because of the material degeneracy in what is called a *helium-flash.* helium-burning cycles occur several times before the star runs out of fuel. This kind of star eventually becomes a white dwarf that is mainly composed of helium. On another hand, if its mass is in the 2.3 to 8 $M_\odot$ range, both hydrogen and helium combustions are ignited without causing an electron degeneracy. A carbon and oxygen (C-O) core therefore forms with a mass that is sufficient to sustain carbon-burning (see Figure 1.2). If this C-O core is partially degenerate, the combustion is ignited outside the center in an explosive manner in what is called a *carbon-flash.* The star is then destined to become a carbon white dwarf. Stars with a very high mass M $\geq$10 $M_\odot$, all chemical elements below iron are burnt. Electronic captures and γ decays occurring in the Fe core lead to type II supernova explosion [12]. The remaining part of the structure does either form a black hole or a neutron star.

1.1 Main sequence stars

Even though our understanding of stellar nucleosynthesis -the process of elements' production by stars- started taking shape many decades ago, it still requires a clarification of certain grey areas essential for the construction of complete astrophysical models. The theory behind stellar nucleosynthesis is based on the consideration of different quantum interactions atomic nuclei are subject to in the stellar environment. It has so far been particularly accurate in describing stellar evolution and predicting a certain number of phenomena associated with it. The nucleosynthesis of elements lighter than iron is achieved in stars following different phases. The first
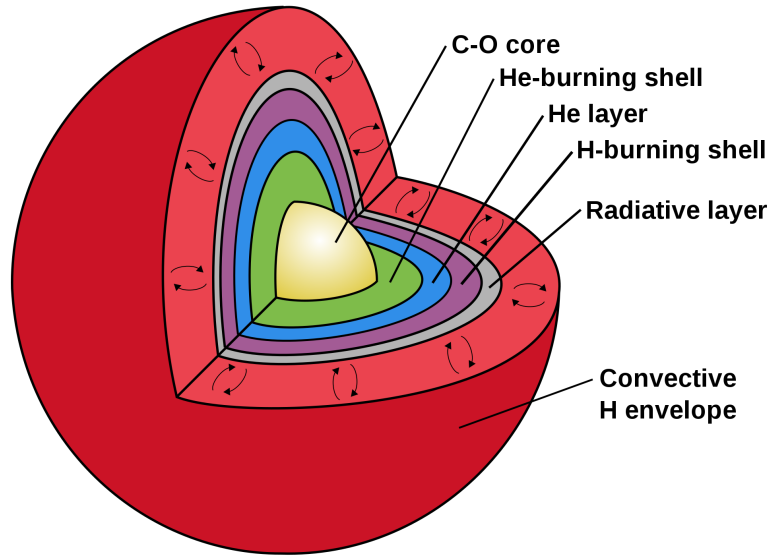
Figure 1.2: Cross-section view of a massive red giant star showing its different chemical layers. The black arrows represent the convection movements occurring in the outer shell.
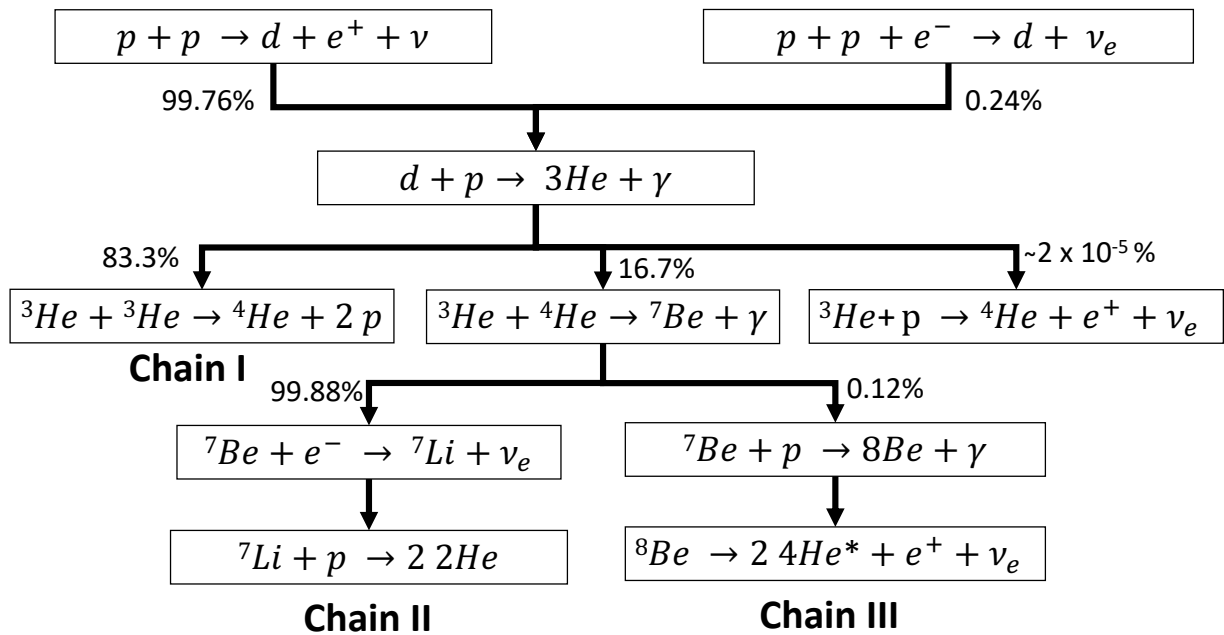
Figure 1.3: proton-proton fusion chains
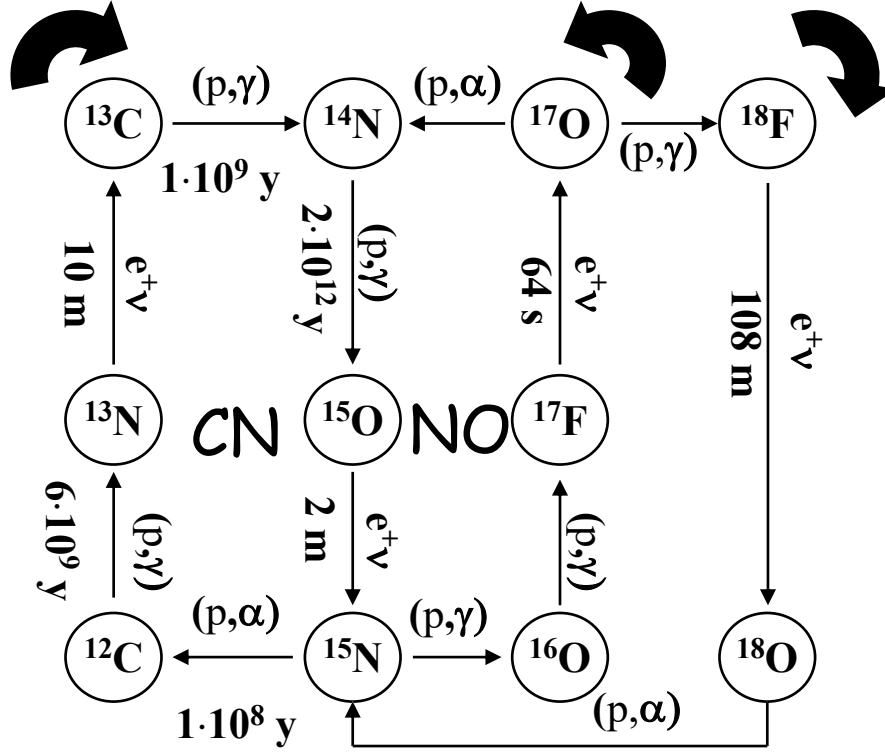
Figure 1.4: Nuclear reactions involved in the CNO cycle. $Q_{eff}^{CN} = 26.02$ MeV and $Q_{eff}^{NO} = 25.73$ MeV.

one, referred to as hydrogen burning, is the formation of helium starting from the very abundant proton interstellar molecular clouds through p-p (for proton-proton) nuclear fusion. This latter occurs following 1 of 3 possible paths -called p-p chains- as shown in Figure 1.3. ^{4}He having a lower mass than 4 protons, the full sequence of reactions is exothermic, releasing around $\sim$19 to $\sim$26 MeV of energy depending on the following chain of reactions. The $\sim$7 MeV energy difference between both processes is due to neutrino production in the cycle (see Figure 1.4).

The majority of stars in the observable universe are second or third-generation stars. This means that the original gas cloud leading to their formation contains elements synthesized in older, now deceased, stars. Three of them, namely carbon, nitrogen, and oxygen can catalyze the hydrogen burning when the total mass is $>$ 1.5 $M_\odot$. This process referred to as the CNO cycle, occurs through different groups of reactions involving the aforementioned species (see Figure 1.4). Its net result is, similarly to the p-p chain, a ^{4}He nucleus formation starting from 4 protons. Its cyclic nature implies that the abundances of different catalysts stay constant throughout the process and can not exceed the number of ^{12}C nuclei originally present in the cloud. Depending on the star's temperature, either the p-p chain or the CNO cycle may dominate the energy production rate as can be seen in Figure 1.5. In both cases, the outcoming energy is sufficient to keep the star in a hydrostatic equilibrium during its settlement on the main sequence phase.

1.2 Later stages and end-of-life

Stars remain in the main sequence until the hydrogen contained in the core is almost exhausted, and therefore become mainly composed of helium-4. The radiative
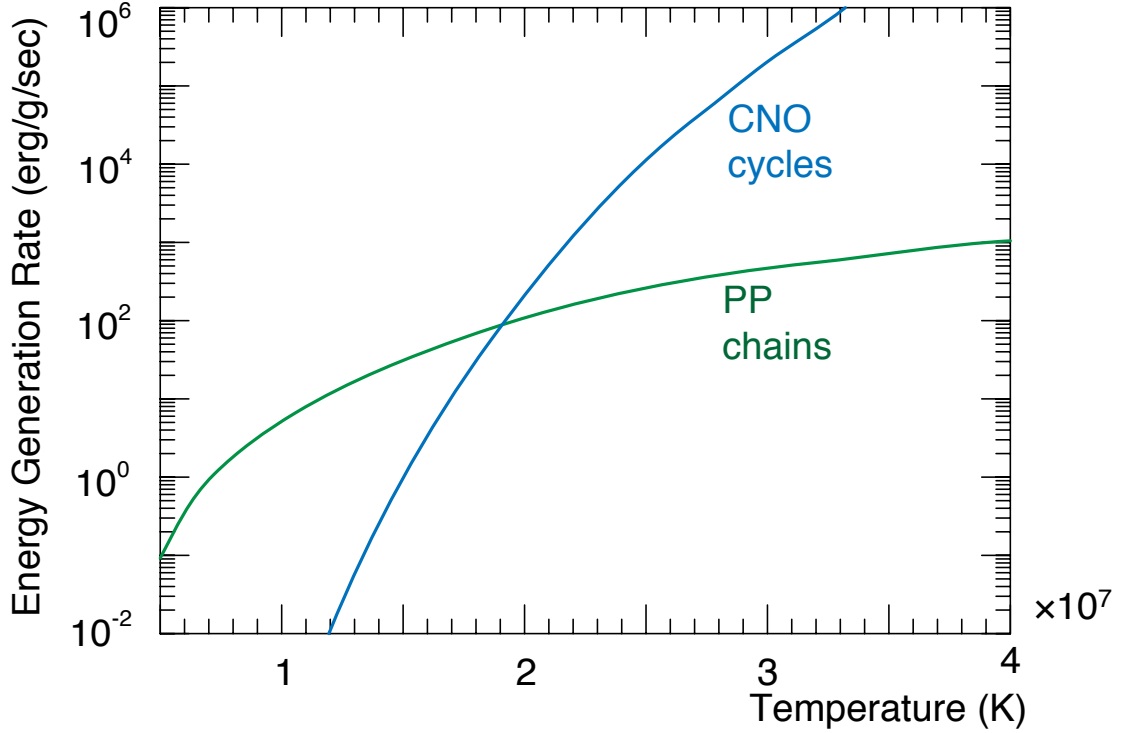
Figure 1.5: Temperature dependence of energy generation rates for p-p chain and CNO cycle in massive stars, adapted from [13].

pressure towards the exterior diminishes, and the star begins contracting once again igniting the hydrogen still present in the surrounding shell. The energy produced by this new ignition cannot all be radiated at the surface, provoking the expansion of the external envelope. The surface temperature drops and the radiated energy wavelength extends and shifts towards red, asserting its red supergiant designation [15, 16, 10]. As mentioned in the preamble of Chapter 1, stars with a mass $M \geq 0.5$ $M_\odot$ shift up-right on the H-R diagram after the core hydrogen burning phase. Their evolution follows the so-called red giant branch (or RGB) where they remain for a relatively short time ($\approx 10\%$ of the H-burning phase duration). For example, when the core temperature of 1 $M_\odot$ star reaches $\sim 10^8$K, its size is multiplied by factor 30 and its luminosity by factor 100. After consuming half of the inner hydrogen mass, the temperature becomes sufficient to ignite the core helium in the degenerate interior [17] following a two-step burning of ^{4}He called triple α-process (Equations 1.2.1 and 1.2.2).

$$^4\text{He} + {}^4\text{He} \leftrightarrows {}^8\text{Be} + \gamma \ (\sim 92 \text{ keV}) \ [t_{\frac{1}{2}} = 3 \times 10^{-16} \text{ s}] \tag{1.2.1}$$

$$^8\text{Be} + {}^4\text{He} \rightarrow {}^{12}\text{C} + \gamma \ (\sim 7.7 \text{ MeV}) \tag{1.2.2}$$

$$^{12}\text{C} + {}^4\text{He} \rightarrow {}^{16}\text{O} + \gamma \ (\sim 6.9 \text{ or } 7.1 \text{ MeV}) \tag{1.2.3}$$

$$^{16}\text{O} + {}^4\text{He} \rightarrow {}^{20}\text{Ne} + \gamma \ (\sim 5.6 \text{ MeV}) \tag{1.2.4}$$
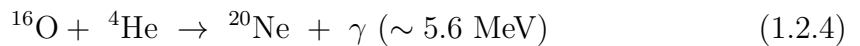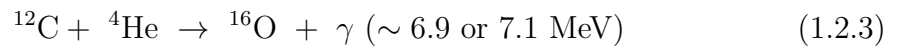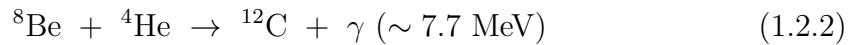
A decoupling of density and temperature occurs at this stage, in the sense that a slight temperature rise provokes a very high energy production rate increase without
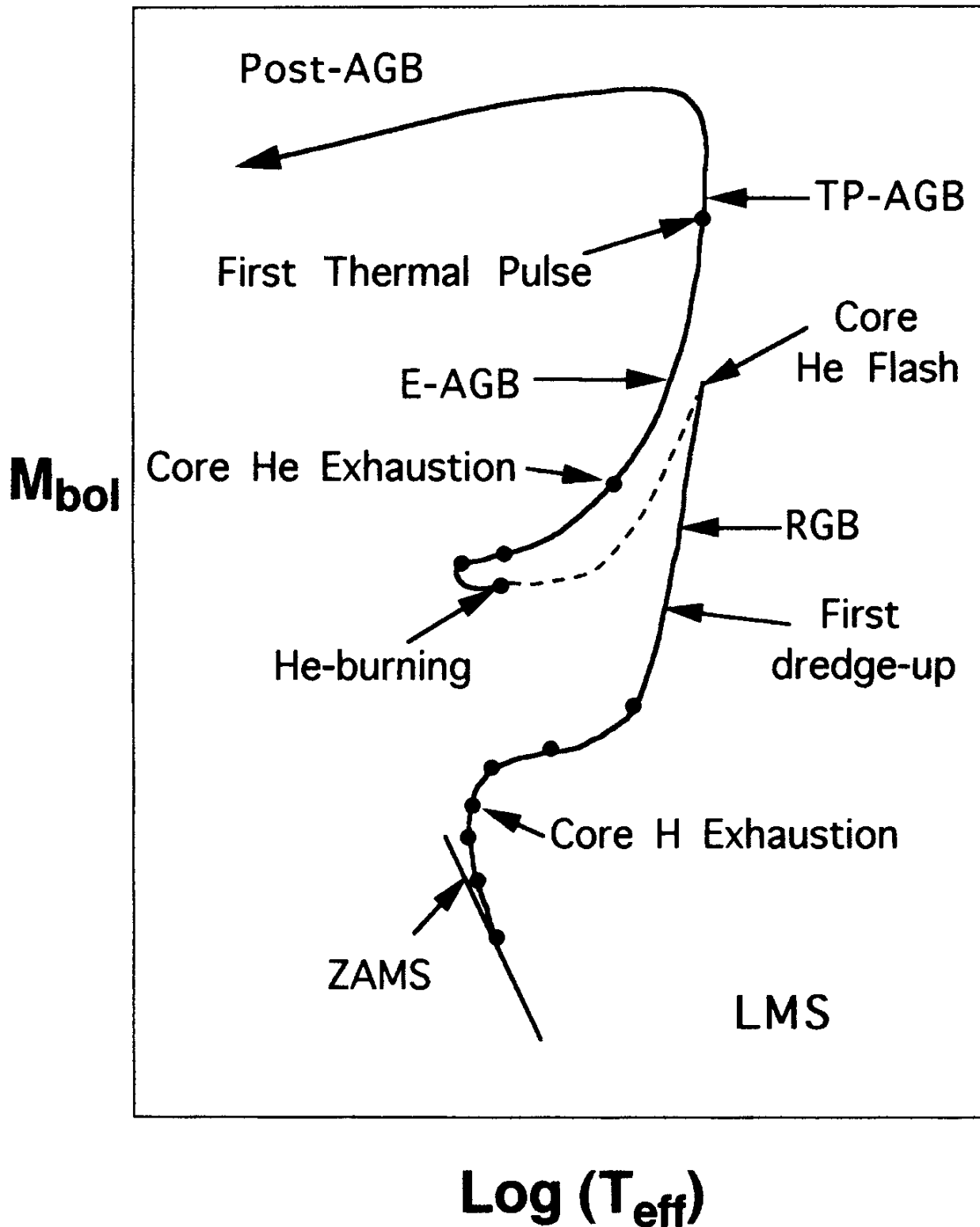
Figure 1.6: 1 M$_\odot$ star evolution from Zero Age Asymptotic Main Sequence (ZAMS) to post-AGB. Reprinted from [14].

affecting the density/pressure. This inevitably leads to detonations of the helium shell -known as *"helium flashes"*- because of the cooling process inefficiency between the helium shell and the external envelope. The expansion and contraction enter then into equilibrium, and the RGB star shifts down-left the H-R diagram in what is called the horizontal branch (see dashed line in Figure 1.6). In this phase, stars show a pulsing behavior reflecting a periodic luminosity variation. This is attributed to the partial ionization of hydrogen and helium in the near-surface region of the star. The increase in ionization decreases the amount of energy reaching the external envelope, leading to a decrease in the luminosity while raising the ions' density which provokes the expansion of the shell. This expansion decreases temperature, which allows ions to recombine with electrons, producing energy and increasing the luminosity again. Until an equilibrium is reached, the star keeps pulsating due to the periodic succession of these two episodes. The later evolution of a star passing the RGB stage almost exclusively depends on its mass. Those with a 0.1 M$_\odot$ $\leq$ M $\leq$ 1.4 M$_\odot$ such as the sun may eject their external envelope forming a planetary nebula while dying by becoming a white dwarf that slowly cools into a black dwarf in around half a billion years. On another hand, stars with a mass M $\geq$ 1.4 M$_\odot$ (Chandrasekar limit) do not have the same fate. Their degeneracy cannot handle the mass collapse and cases can here be distinguished :

- **1.4 M$_\odot$ $\leq$ M $\leq$ 8 M$_\odot$**: a somehow gentle adjustment is operated by expelling the excess mass into the interstellar medium as a planetary nebula. The goal of the process is to reach the 1.4 M$_\odot$ and therefore stability. The star then becomes a helium white dwarf if M $\leq$ 2.4 M$_\odot$ or that of carbon if M $\geq$ 2.4 M$_\odot$.

- **M $\geq$ 8 M$_\odot$**: the star has a much shorter remaining lifespan [3] and a series of shrinkages and pauses take place in its interior, each time provoking the ignition of newer (and heavier) chemical elements. The products of the previous fusion from the previous shrinking process become the fuel of the following one. Helium from the hydrogen burning fuses into carbon and oxygen when high temperature and pressure conditions are met.

The shrinkage-pause cycles in heavy-mass (M $\geq$ 8 M$_\odot$) stars continue while thermonuclear energy is available. At each new burning stage, the produced energy decreases due to the increase in the average binding energy per nucleon needed to produce the next heavier element, combined with the energy loss due to the formation of neutrinos. The final element reached through this process is iron (^{56}Fe) which accumulates in the core. The gravitational collapse then provokes a photo-disintegration of the iron in the core as well as electron capture that ionizes the surrounding gas. Energy keeps being lost to neutrinos accelerating the collapse of the core and leading to a huge explosion of the star known as a Type II supernova [18][19]. Under certain conditions, the highly dense core survives the explosion and becomes a neutron star or black hole.

Below-iron elements nucleosynthesis

To sum up, stars in the main sequence do mostly produce helium by burning hydrogen. When this latter is exhausted, the core contracts increasing temperature, expanding the external envelope of the star and igniting further elements burning. The helium burns producing carbon, oxygen, and some neon respectively as shown
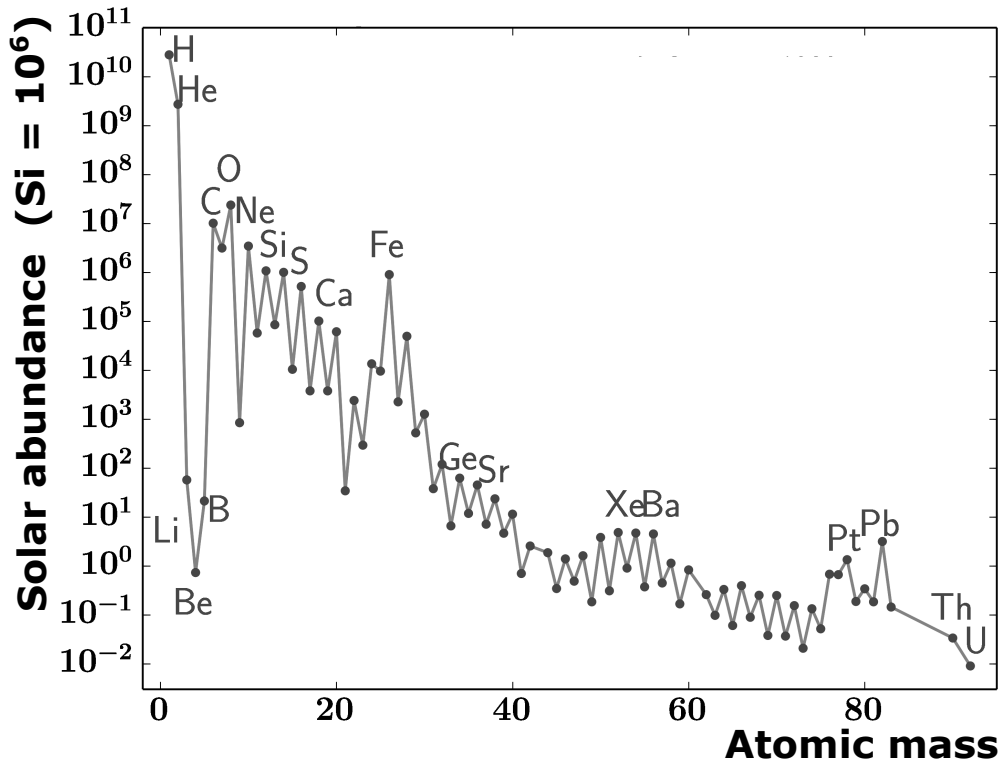
Figure 1.7: Chemical elements abundances in the solar system normalized to Silicon $= 10^6$. Data from [21].

in Equations 1.2.1 to 1.2.4. Carbon and oxygen themselves then burn producing Na, Mg, Al, Si, S, and Ca while at higher temperatures Neon burns producing Fe, Ni, Cr, Mn, and Co. The final abundances of these elements depend on the reactions' cross-sections and the ratio between those producing and those destroying each element. Most of the elements produced are collectively ejected into interstellar space in the form of immensely large clouds. Those latter then condense under the effect of gravitational attraction and then follow a different evolution path depending on the total accumulated mass. Some become later-generation stars containing traces of higher-mass elements which may catalyze new nuclear reactions [20].

1.3 Stellar nucleosynthesis of heavy elements

As stated above, carbon, nitrogen, and oxygen are formed in stars through the capture of charged particles, mainly protons and α-particles. This process continues until the formation of iron, the pivot element beyond which the nuclei' average binding energy per nucleon decreases, implying that more energy is needed to the reaction occur than that it releases. Nevertheless, the observed abundances of elements beyond the iron peak in the solar system (see Figure 1.7) don't quite correlate with this drop in transmissibility, thus indicating the existence of other nucleosynthesis mechanisms responsible for the formation of heavier elements. Neutrally charged particles are not subject to the Coulombian repulsion. The synthesis of heavier elements continues beyond the iron peak through a series of direct neutron captures followed by a β^- decay, consequently rising atomic number. When it occurs in
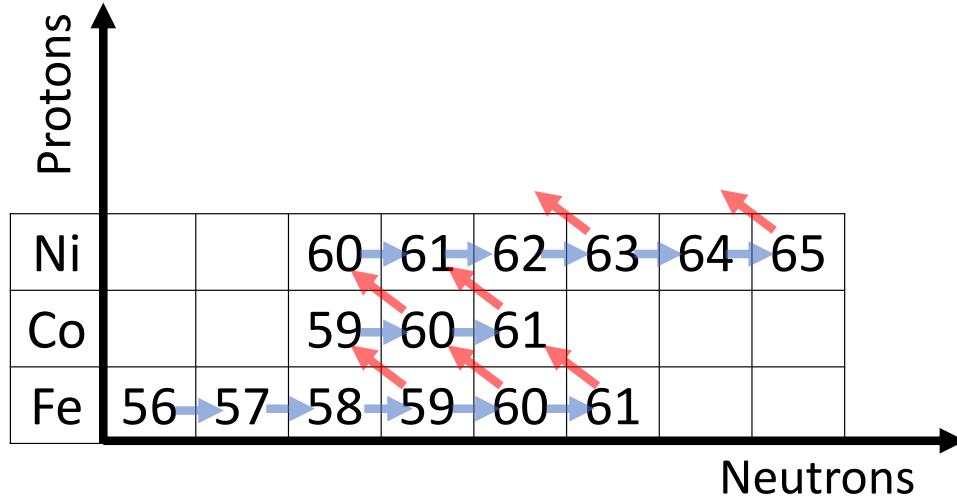
Figure 1.8: Nucleosynthesis of some beyond-iron elements through s process. The blue arrows represent slow neutron capture and the red arrows represent β^- decay responsible for the atomic number increase.

AGB stars where $^{13}C(\alpha,n)^{16}O$ and $^{22}Ne(\alpha,n)^{25}Mg$ are activated, generating a neutron density of about few 10^8 cm^{-3}, it is called the "s process" see Figure 1.8). On the contrary, the rapid neutron capture process or "r process" takes place when an abundant flux of neutrons ($\geq 10^{21}$ cm^{-3}) is available [22]. Multiple neutrons are captured quasi-simultaneously forming the furthest isotopes from the valley of stability. It is usually followed by one or more β^- decays bringing the elements to a more stable position with a higher atomic number Z. The explanation of the observed abundances of beyond-iron elements in our solar system through neutron capture reactions requires the study of both r and s processes. While the r process mostly contributes in the case of magical neutron numbers (N = 50, 82, and 126), the s process contribution can be found throughout most elements beyond iron. Nevertheless, its amount depends on two main elements: the cross-section of the neutron capture of the nucleosynthesis reaction, and the production rate of the source reaction feeding it with neutrons. The cross-section of neutron captures usually decreases with increasing neutron energy. In terms of stellar evolution, neutron capture reactions are not a source of any significant energy for stars.

S process components

As stated above, the s process is a succession of neutron capture reactions followed by beta decay (see Figure 1.8) that usually occurs at neutron densities $\leq 10^{11}$ cm^{-3}. It allows the stellar nucleosynthesis of heavy elements starting from the iron peak up to ^{209}Bi, the heaviest known stable isotope. Any neutron capture beyond this limit results in an α-decay decreasing the atomic number of the product nucleus. The s process has three different components, each dominating at different atomic mass ranges. The first one is called the "weak" s process. It mostly contributes to the formation of elements with an atomic mass 60 < A < 90. On another hand, the so-called "main" s process, contributes for the most part to the A = 90 to 205

region. The third component is named "strong" s process. Postulated in 1967 [23], it produces elements between ^{206}Pb and ^{209}Bi directly from the vastly available ^{56}Fe isotope. It is estimated that around half of the total production of these two isotopes is achieved through this third component. The principal neutron source reaction feeding the "main" and the "strong" s process is ^{13}C(α,n)^{16}O. It occurs during the AGB phase of low mass stars of M < 3 M$_\odot$ [14]. The "weak" s process, on the contrary, is the dominant component in massive stars with M > 13 M$_\odot$ during the core helium and shell carbon burning phases [24]. It is mainly fed by ^{22}Ne(α,n)^{25}Mg, relevant to this work. This latter reaction also contributes in medium mass stars of 4 M$_\odot$ < M < 8 M$_\odot$ for the production of stable magnesium isotopes with well-known measurable abundances[25].

The case of low-mass AGB stars

In low to intermediate-mass AGB stars, hydrogen and helium burning occurs in thin shells surrounding an electron-degenerate C-O core. It is during this phase that it contributes the most to the enrichment of the interstellar medium through a combination of convective movement between the core and outer shells, then the stellar winds that expel the newly formed nucleosynthesis products. In the early AGB phase, helium burning in the shell surrounding the compact C-O core is the main energy source for the star. When the shell's helium is exhausted and the star contracts again, the thermally pulsing AGB phase (TP-AGB) starts, and hydrogen fusion in the outer shell ignites and becomes the main energy source. The produced helium "sinks" to the thin ^{4}He shell and abruptly starts burning when conditions are met. This sudden explosive helium ignition due to the degenerate core is characterized by a short but high luminosity increase by a few thousand and is called a thermal pulse of helium flash. This provokes the expansion of the star which inevitably leads to its cooling, creating a convection movement between the hydrogen and the helium shells[26]. During the thermal pulse, energy production is mainly due to triple-α capture reactions. The mixing zone between the shells, often referred to as *Pulse Driven Convective Zone* or PDCZ, the flash creates is responsible for the transformation of a fraction of the ^{14}Ne produced during the CNO cycle into ^{22}Ne isotope. This latter accumulates in the bottom of the PDCZ where high temperatures $\geq$ 0.25 GK allow the ignition of the ^{22}Ne(α,n)^{25}Mg key reaction (see Figure 1.9). A competition between this reaction and ^{22}Ne(α,γ)^{26}Mg that requires lower temperatures takes place over the available ^{22}Ne budget[27]. It is important to determine the ratio of their rates since this directly influences the amount low low-energy neutrons available for the nucleosynthesis of heavier elements through the s process (see Section 1.3). Nevertheless, it is the ^{13}C(α,n)^{16}O nuclear reaction that remains its major neutron provider in low-mass AGB stars. It mostly occurs in the ^{13}C pockets that form in the upper region of the helium shell between two thermal pulses produced through ^{12}C(p,γ)^{13}N(β^+ ν)^{13}C series of reactions[28]. The TP-AGB phase causes a mass loss for the star in the form of stellar winds, the majority of which occur during the thermal pulse. It is estimated that an AGB star may lose up to around 70% of its mass during this phase [29]. After the last thermal pulse occurs, the star moves to the left of the HR diagram entering the post-AGB (P-AGB) phase. The star's evolution becomes then uncertain even though stellar models show that those having 1 M$_\odot$ produce planetary nebulae[30].
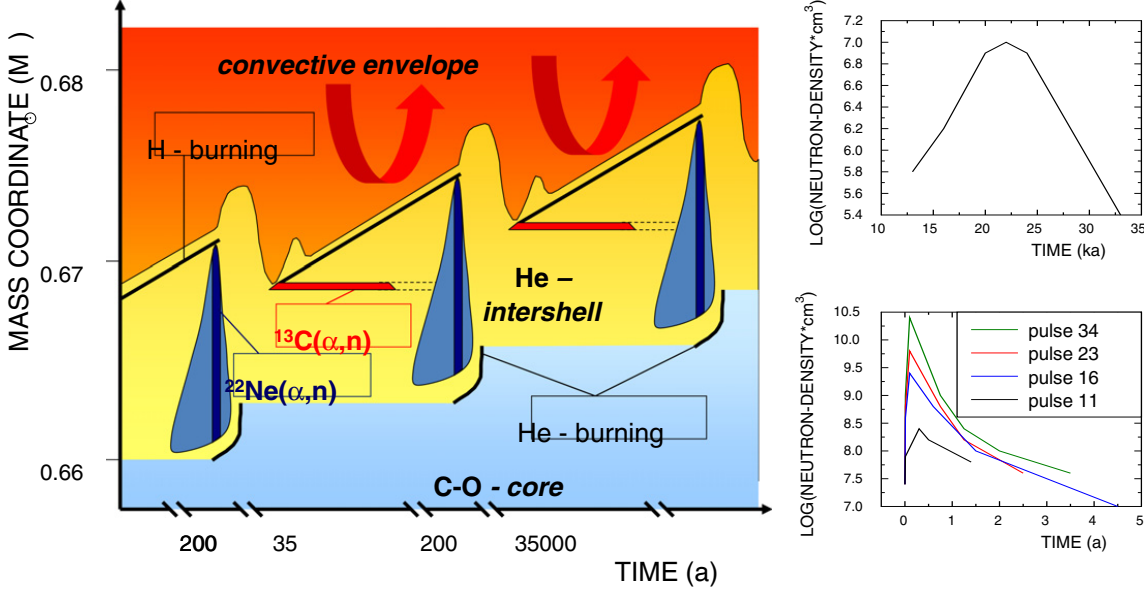
Figure 1.9: Convection mixing during the TP-AGB phase and ^{13}C pockets location (left). Neutron density production by (α,n) through time for ^{13}C (right-top) and ^{22}Ne (right-bottom). Reprinted from [31].

The case of massive stars

To explain beyond-iron peak abundances of isotopes having an atomic mass A<90, the contribution of the s process in massive stars $M_\odot > 8$ should also be considered alongside that of the low-mass AGB stars case. The main difference between the two is that it is ^{22}Ne(α,n)^{25}Mg that is the major neutron contributor to the s process. This occurs in both the convective He core burning (T $\sim 3 \cdot 10^8$ K) and the carbon burning (T $\sim 10^9$ K). ^{22}Ne is also produced during helium burning from the CNO ^{14}N ashes through ^{14}N(α,γ)^{18}F(β^+ ν)^{18}O(α,γ)^{22}Ne. Helium is here fully consumed before all ^{22}Ne nuclei react [22] implying that both ^{22}Ne(α,n)^{25}Mg and ^{22}Ne(α,γ)^{26}Mg resume during the C carbon burning phase using helium nuclei this latter produces through ^{12}C(^{12}C,α)^{20}Ne[32]. Previous works showed that the s process in high-mass stars during the convective carbon burning takes place at similar neutron flux exposure conditions than in the previous phase (i.e. Helium burning)[33]. As discussed in Section 1.2, the star may then explode producing a Type II supernova since it cannot initialize the burning of its iron core[31]. The explosion erases any s process fingerprint from the core up to a 3.5 M⊙ in the case of a 25 M⊙ star. Only around $\sim$ 2.5 M⊙ of the produced ejecta, originating from the hydrostatic nucleosynthesis phase, retains the original s process abundances. A large amount of the He interacts during the explosion with the unconsumed ^{22}Ne through ^{22}Ne(α,n)^{25}Mg increasing the neutron flow that leads to the further nucleosynthesis of further elements, thus changing the overall chemical composition in this region[34]. A precise knowledge of the ^{22}Ne(α,n)^{25}Mg cross-section is therefore key for the building of a reliable nucleosynthesis evolution model for massive stars.

1.4 Nucleosynthesis in intermediate-mass AGB stars

According to state-of-the-art stellar evolution models, the TP-AGB phase is heavily mass-dependent. This represents a major difference with the low-mass case leading to a non-identical evolutionary scheme. Instead of the s process, intermediate-mass AGB stars go through the hot bottom burning (HBB). A process in which the outer part of hydrogen-shell burning is part of the convection envelope[27]. This increases the availability of core content in the outer layer, increasing the star's luminosity which diverges from the low-mass case model calculations. The HBB contributes to stellar nucleosynthesis by sustaining proton-induced reactions such as the CNO cycle. The NeNa and MgAl cycles may also be activated if the temperature reaches values above 60 MK. Previous studies showed that it is also responsible for the production of ^{7}Li through the so-called Cameron-Fowler mechanism already taking place at temperatures between 30 and 40MK [35][36]. The MgAl cycle also consumes ^{24}Mg when temperatures surpass 90MK in intermediate-mass AGB stars, heavily impacting its abundance. The two other magnesium isotopes, namely ^{25}Mg and ^{26}Mg, are produced by respectively ^{22}Ne(α,n)^{25}Mg and ^{22}Ne(α,γ)^{26}Mg during the helium shell TP-AGB phase (see Section 1.3). Neutrons from ^{22}Ne(α,n)^{25}Mg also contribute to the final ^{25}Mg/^{26}Mg abundance ratio by inducing the ^{25}Mg(n,γ)^{26}Mg. The importance of magnesium isotopic distribution resides in our ability to measure its signature through stellar spectroscopy, providing a crucial tool for the chemical study of the stellar medium. The ratios of its three stable isotopes derived from the spectra of cool dwarfs located in the thin/thick disk of the galaxy [37] and that of giant stars in the (GC) NGC 6742 globular [38] cluster cannot be explained by the sole contribution of burning occurring in the carbon and neon shells in massive stars. The contribution of intermediate-mass AGB stars through the study of the aforementioned nuclear reactions can therefore be considered as additional major production sites thus improving the current Galactic Chemical Evolution models. It has also been shown that magnesium production intermediate-mass AGB stars is very sensitive to the reaction rate of ^{22}Ne(α,n)^{25}Mg and ^{22}Ne(α,γ)^{26}Mg[39] alongside the convection movements. As of now, both reactions' measured rate values come with very large uncertainties at stellar energies[40]. This directly results in non-negligible variation in predictions made over the final abundances of isotopes ranging from ^{25}Mg up to ^{31}P of respectively 1 order of magnitude for ^{22}Ne(α,n)^{25}Mg and 2 orders of magnitude for ^{22}Ne(α,γ)^{26}Mg at stellar temperatures below 300MK, a region largely dominated by this latter reaction. Works such as [39], attempted to recalculate the relative production of ^{25}Mg and ^{26}Mg in a 5 M$_\odot$ AGB star at different metallicity values. A reduction in the uncertainties of the two ^{22}Ne + α reaction rates led to a considerable lowering of the uncertainty over the productions of Mg → P isotopes to ∼30%, which is a remarkable improvement compared to those obtained using upper/lower limits from in the NACRE compilation[41]. The uncertainty over the production of P was also improved from around 400% to 35% (see Figure 1.10).
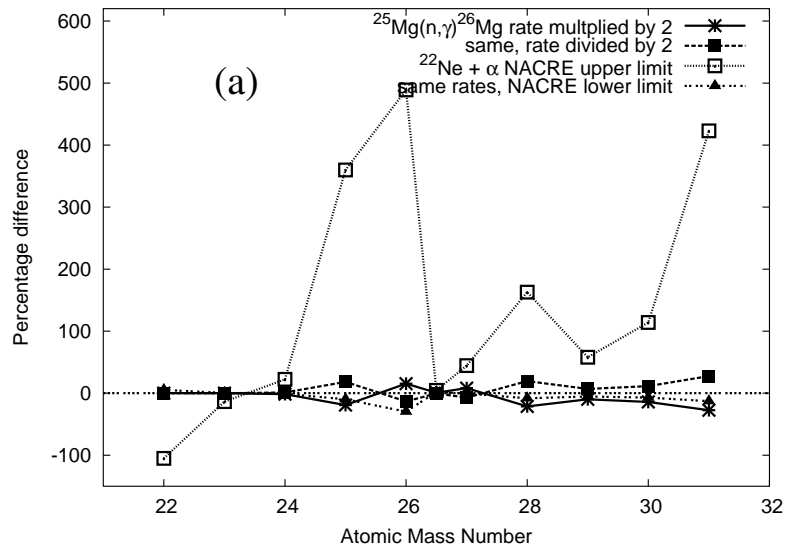
Figure 1.10: Difference between stellar yields calculated using ^{22}Ne + α reaction rates from as recommended in [39] and using the NACRE upper/lower limits [41] expressed in %. Model calculated for an AGB star mass and metallicity parameters of (5 M$_\odot$,Z = 0.02) and figure from [39].

Chapter 2

Experimental study of nuclear reactions

More than a century ago, research on the nature of atoms assessed their composition: a positively charged nucleus surrounded by electrons of negative charge. Later experiments showed that the nucleus is composed of several positively charged particles called protons and neurally charged particles called neutrons. The number of protons (Z) determines the chemical nature of the element while a variation in the number of neutrons (N) for the same Z creates more or less stable element isotopes. The total number of nucleons (i.e. protons and neutrons) is referred to as A, giving the following notation for an isotope belonging to a certain chemical element X:

$$^{A}_{Z}X_{N}$$

For easier readability, the Z and N are often omitted in this work since the element kind is already identifiable by its X nomenclature.

Nuclear reactions are the main energy source in stars. Lighter elements, starting from hydrogen, react through nuclear fusion to produce heavier elements until ^{56}Fe. Elements heavier than iron are produced by successive neutron capture reactions followed by β^{-} decays, named s and r processes depending on the available neutron density (see Section 1.3). All 3 nuclear reactions belong to the more general process called stellar nucleosynthesis. A nuclear reaction involving a projectile x and target nucleus A, producing y and B byproducts is noted A(x,y)B or :

$$A + x \rightarrow y + B$$
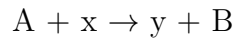
where A and x are called the reaction's entrance channel while y and B represent the exit channel. To describe the energy balance of a nuclear reaction, the concept of Q-value is introduced. It represents the amount of energy absorbed or released through the nuclear reaction. Following the energy conservation rule, the Q-value quantity is calculated as a mass excess as shown in Equation 2.0.1.

$$Q = (m_A + m_x - m_y - m_B) \cdot c^2 \tag{2.0.1}$$

The Q-value can be either positive or negative. In the first case, the reaction releases energy as is the case for hydrogen and helium fusions discussed in Sections 1.1 and 1.3. When the Q-value is negative, an energy superior to its absolute value should be provided to the system for the reaction to occur.

2.1 Nuclear reaction rate

An important quantity on which stellar evolution depends is the rate at which it occurs in the stellar medium. Often referred to as r, it is defined as the number of reactions happening per unit of volume per unit of time as described in the following equation from [17]:

$$ r = \frac{N_R}{V \cdot t} = n_1\ n_2\ \sigma(\nu)\ \nu\ = n_1\ n_2\ \langle \sigma\nu \rangle \tag{2.1.1} $$

where n_1 and n_2 represent the nuclear densities of the two interacting nuclei, ν their velocities, and $\sigma(\nu)$ the reaction cross section at the velocity ν. The product of the two latter quantities referred to as $\langle \sigma\nu \rangle$ represents the reaction rate per pair of particles. The energy of interacting nuclei in a non-degenerate plasma at thermodynamic equilibrium can be expressed as :

$$ P(E)\ dE = \frac{2}{\sqrt{\pi}} \cdot \frac{1}{(kT)^{\frac{3}{2}}} \cdot \sqrt{E} \cdot e^{-\frac{E}{kT}}\ dE \tag{2.1.2} $$

where the kinetic energy of the system $E = \frac{\mu\nu^2}{2}$ (with $\mu = \frac{M_1 M_2}{M_1 + M_2}$), T is the stellar gas temperature, and k is the Boltzmann constant. A broadening of the peak can be noticed when plotting P(E) -the Maxwell-Boltzmann distribution- at different kT values corresponding to different stellar scenarios (see Figure 2.1).

The reaction rate per pair of particles can therefore be expressed as :

$$ \langle \sigma\nu \rangle = \left(\frac{8}{\pi\mu}\right)^{\frac{1}{2}} \cdot (kT)^{-\frac{3}{2}} \cdot \int_0^{+\infty} E\ \sigma(E)\ e^{-\frac{E}{kT}}\ dE \tag{2.1.3} $$

Equation 2.1.3 is always true since the energy E is taken in the center-of-mass frame. The lower limit of the integration range is set to always be 0, the value of $\sigma(E)$ being anyways zero below the reaction's threshold energy. An analytical expression for the cross-section $\sigma(E)$ must be derived to estimate the total reaction rate. In the case of charged-particle capture that leads to the nucleosynthesis of elements before the iron peak, the reaction proceeds through resonant and non-resonant modes. Depending on their width, resonances may be considered either narrow or broad [20]. For this work, only non-resonant and narrow resonances are of interest and therefore will be discussed.

2.2 Nuclear reaction cross-section

The collision between particles allows the investigation of the nuclear properties of the particles/ions/isotopes involved in the reactions. This is often done in fixed target experiments at the lab by sending a beam of particles (usually of a lower mass), into a target containing the other reaction partner. The out-coming products are registered using a detection system strategically placed in the vicinity of the reaction center (see Figure 2.2). When this process doesn't alter the nature of the target nor that of the projectile, it is called elastic scattering. In this case, only energy and momentum are transferred between projectile and target. On the contrary, when an excitation of the energy levels of the target occurs or when it is transformed into another chemical element, the reaction is called "inelastic reaction". Beyond their energies and scattering angle, an important piece of information to extract from each reaction from the point of view of nuclear physics is its cross
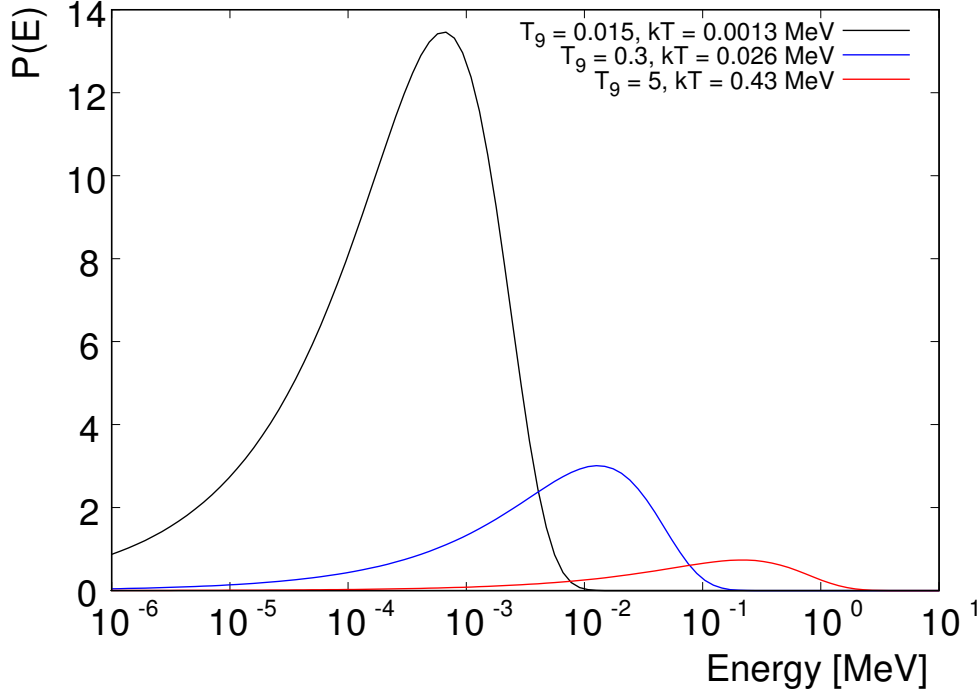
Figure 2.1: The Maxwell-Boltzmann distribution at different stellar stages having different temperatures. In black is when it is in the main sequence, in blue is the case of a classical nova [42] and in red is during a Type II supernova.

section. It is defined as the probability of having the projectile particle interact with the target:

$$\sigma \equiv \frac{\frac{N_R}{t}}{\left(\frac{N_b}{t \cdot A}\right) \cdot N_t} \tag{2.2.1}$$

where σ represents the reaction cross-section, $\left(\frac{N_R}{t}\right)$ is the number of interactions per unit of time t. $\left(\frac{N_b}{t \cdot A}\right)$ is the number of incident particles per unit of time t and area A. N_t is the number of particles within the beam. It is experimentally better suited to rewrite $\left(\frac{N_R}{t}\right)$ using the often well-known incident particles flux which is proportional to the accelerator beam current, as follows:

- **Beam area A > target area A_t:** $\frac{N_R}{t} = \left(\frac{N_b}{t \cdot A}\right) \cdot N_t \cdot \sigma$

- **Beam area A < target area A_t:** $\frac{N_R}{t} = \left(\frac{N_b}{t}\right) \cdot \left(\frac{N_t}{A}\right) \cdot \sigma$

where in the first case, $\left(\frac{N_b}{tA}\right)$ represents the number of incident particles flux and N_t the number of target nuclei and σ is the reaction cross-section. In the second case, it is more practical to consider $\left(\frac{N_b}{t}\right)$, the current of incident particles. In a homogeneous target, the ratio $\left(\frac{N_t}{A}\right)$ is equal to the total number of the nuclei in the target divided by its total area A_t, a value that is easier to estimate experimentally. A schematic drawing of the different variables discussed above is shown in Figure 2.2. The cross-section has a dimension of a surface, however, since its usual values are very low, it is more practical to use the barn (b) defined as $1 \text{ b} = 10^{-28} \text{ m}^2$
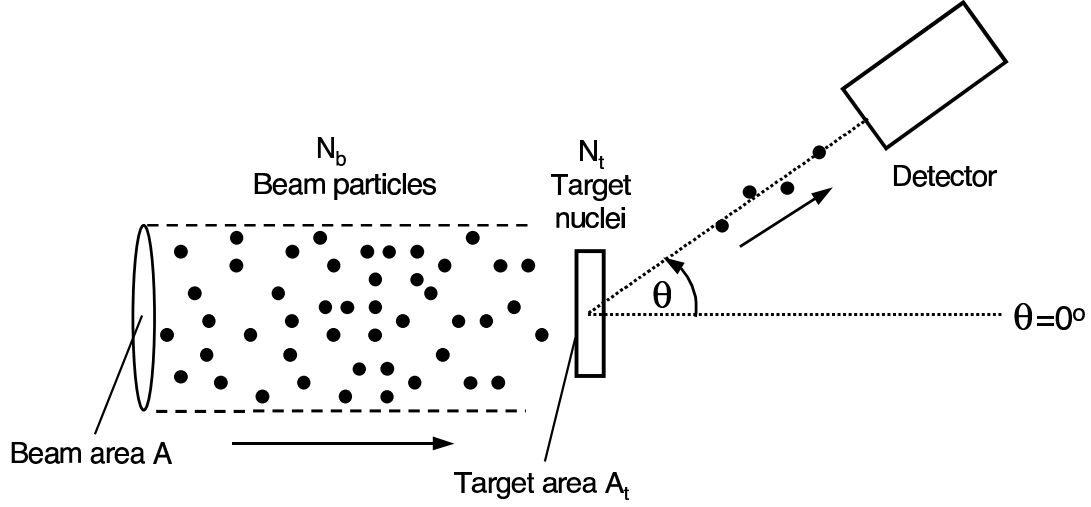
Figure 2.2: Schematic representation of a standard beam into target nuclear reaction experiment. Adapted from [20].

Non-resonant mode

It is important to consider the Coulombian repulsion between charged particles to express the cross-section in terms of the stellar environment energy. This quantity is often expressed as a potential written as :

$$V_C(r) = \frac{Z_1 Z_2 e^2}{r} \tag{2.2.2}$$

where Z_1 and Z_2 represent the number of positive charges in the nuclei, r is the distance between the two, and e is the elementary charge. Equation 2.2.2 implies that the Coulombian repulsion increases when the distance decreases. The energy should therefore be higher than the Coulombian barrier so the nuclear reaction can occur in a classical mode. This is very often not the case at stellar energies where the reaction only takes place because of the quantum tunnel effect described by quantum mechanics. The cross-section can be expressed using the Schrödinger equation solution for the s-wave approximation case as:

$$\sigma(E) = E^{-1} \cdot e^{(-\frac{2\pi}{\hbar}\sqrt{\frac{\mu}{2E}}Z_1 Z_2 e^2)} \equiv E^{-1} \cdot e^{-2\pi\eta} \cdot S(E) \tag{2.2.3}$$

The cross-section E^{-1} energy dependency is removed as well as that of the probability of the s-wave transmission through the tunnel effect below the Coulomb barrier height, represented by the $e^{-2\pi\eta}$ term and referred to as the Gamow factor. The tunnel effect is the dominant effect at stellar (low) energies allowing the reaction to take place. The nuclear effects of the reaction are gathered in the S(E) term - called S-factor or astrophysical factor- and show less variation than the exponentially behaving cross-section. Combining Equations 2.1.3 and 2.2.3, the reaction rate per pair becomes:

$$\langle \sigma\nu \rangle = (\frac{8}{\pi\mu})^{\frac{1}{2}} \cdot (kT)^{-\frac{3}{2}} \cdot \int_0^\infty S(E)\, e^{-2\pi\eta}\, e^{-\frac{E}{kT}}\, dE \tag{2.2.4}$$
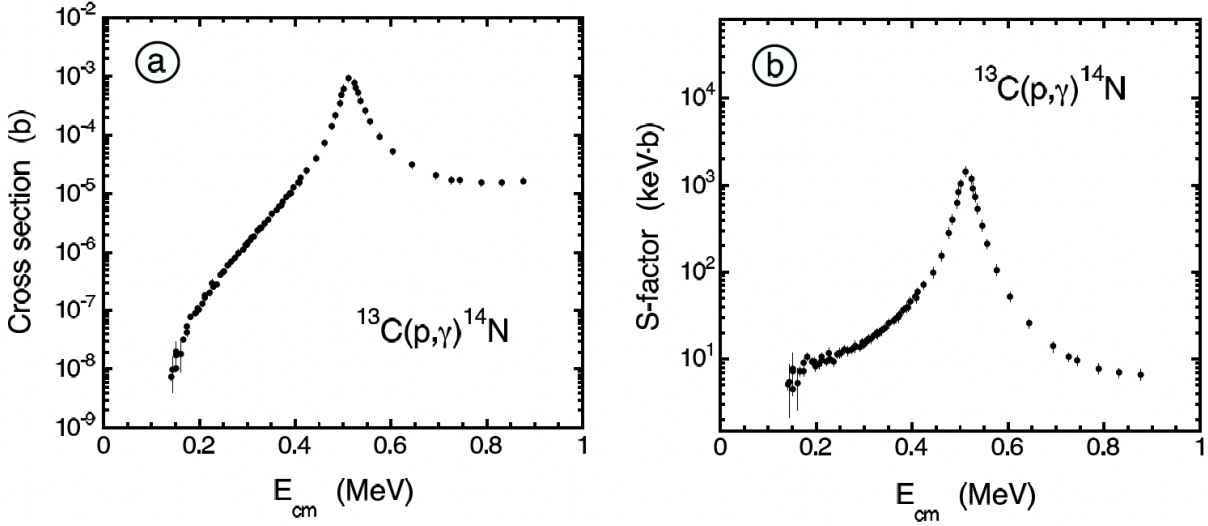
Figure 2.3: ⓐ experimental cross-section and ⓑ S-factor values of the ^{13}C(p,γ)^{14}N reaction around $E_{cm} \approx 0.5$ MeV. Reprinted from [20].

It integrates the convolution of the Maxwell-Boltzmann energy distribution and the penetrability factor of the Coulomb barrier. When plotted, it results in what is called the Gamow Peak, representing the most probable energy window for the reaction to take place (see Figure 2.4).

Narrow resonance mode

A nuclear reaction is achieved through a resonance mode when the sum of the Q-value of a nuclear reaction and the projectile's energy in the center-of-mass system matches the energy of an excited level of the obtained compound nucleus. This latter then decays into lower energy states making this nuclear reaction a two-step process. The probability of each step to happen is usually referred to as a partial width Γ_i, while the product of the two is set to be proportional to the cross-section as follows :

$$\sigma \propto \Gamma_a \cdot \Gamma_b \qquad (2.2.5)$$

where Γ_a and Γ_b are respectively the partial widths of the compound nucleus production and decay. It is important to note that the deexcitation may occur following different transition channels. A resonance width Γ is here defined as the sum of all possible decay channels. A resonance is considered narrow in the case of $\Gamma \ll E_r$. It is also called isolated if the resonances positions separation is much larger than their width Γ. In this case of both conditions being met, the cross-section can be expressed using the Breit-Wigner formula, as follows :

$$\sigma_{BW}(E) = \pi \left(\frac{\lambda}{2\pi} \right)^2 \cdot \frac{2J+1}{(2J_1+1)(2J_2+1)} \cdot (1+\delta_{12}) \cdot \frac{\Gamma_a \Gamma_b}{(E-E_r)^2 + (\frac{\Gamma}{2})^2} \qquad (2.2.6)$$

where $\pi \left(\frac{\lambda}{2\pi} \right)^2$ is the geometrical cross-section, $\frac{2J+1}{(2J_1+1)(2J_2+1)}$ is a statistical factor considering the spin-orbit distribution of the nuclei, J_1 and J_2 being the angular
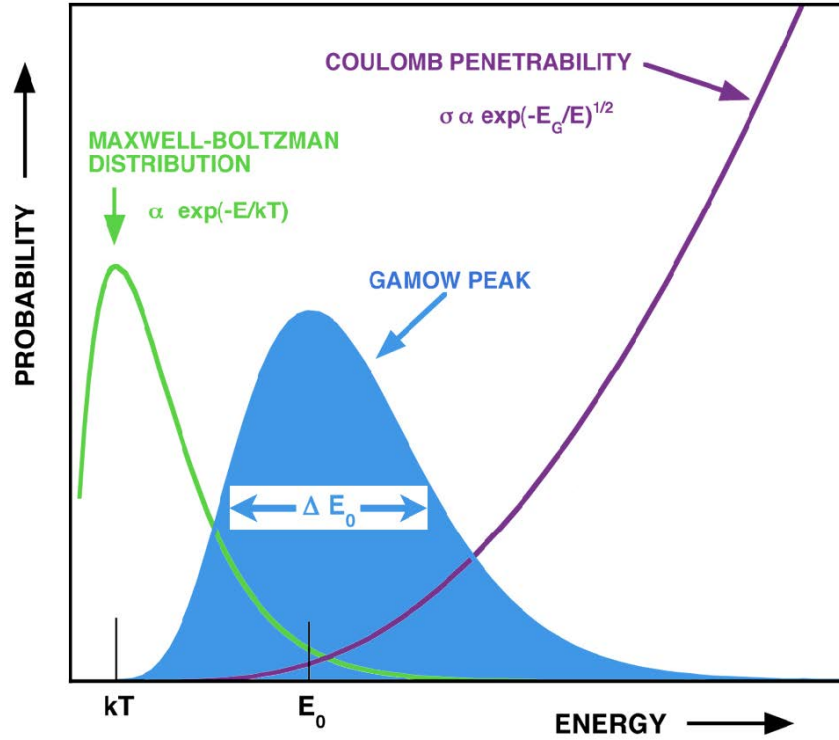
Figure 2.4: Schematic representation of the Gamow window. E_0 is the energy at which the reaction rate is maximized for a temperature T.

momenta of respectively the target and projectile nucleus, and J the angular momentum of the compound nucleus excited state. The $(1 + \delta_{12})$ term is introduced to take into consideration the case where the entrance and exit channels are identical, thus multiplying the cross section by 2. The $\frac{\Gamma_a \Gamma_b}{(E - E_r)^2 + (\frac{\Gamma}{2})^2}$ term describes the resonant damped oscillator response. Once again, it is possible to express the reaction rate per pair considering a resonant contribution using the Breit-Wigner formula as follows :

$$\langle \sigma \nu \rangle = \left(\frac{8}{\pi \mu} \right)^{\frac{1}{2}} \cdot (\mathrm{kT})^{-\frac{3}{2}} \cdot \mathrm{E_r} \cdot e^{-\frac{\mathrm{E_r}}{\mathrm{kT}}} \int_0^{+\infty} \sigma_{BW}(E) \; \mathrm{dE} \tag{2.2.7}$$

The term $\mathrm{E} \cdot \mathrm{e}^{-\frac{\mathrm{E}}{\mathrm{kT}}}$ shows a very limited variation around the resonance energy thus justifying its extraction from the integrand. The remaining integral represents the resonance strength $\omega \gamma$ and can directly be calculated as follows :

$$\omega \gamma = \frac{2J + 1}{(2J_1 + 1)(2J_2 + 1)} \cdot (1 + \delta_{12}) \cdot \left(\frac{\Gamma_a \Gamma_b}{\Gamma} \right) \tag{2.2.8}$$

In the same way, Equation 2.2.7, the reaction rate per pair of particles can be rewritten in terms of resonance strength, thus giving :

$$\langle \sigma \nu \rangle = \left(\frac{2\pi}{\mu \mathrm{kT}} \right)^{\frac{3}{2}} \cdot \hbar^2 \cdot (\omega \gamma)_\mathrm{r} \cdot e^{-\frac{\mathrm{E_r}}{\mathrm{kT}}} \tag{2.2.9}$$
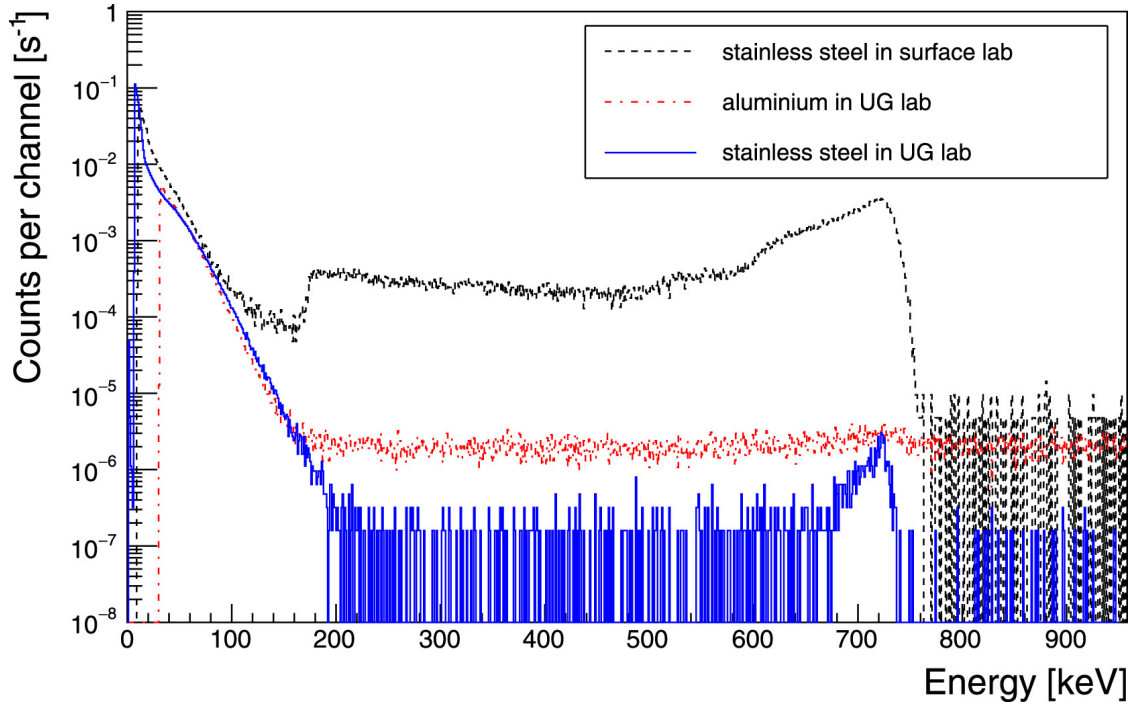
Figure 2.5: Comparison of neutron background spectra of unshielded ^{3}He proportional counters measured on a surface laboratory (in black) versus LNGS using 1 counter having aluminum housing (in red) and stainless steel (in blue). Figure from [45].

The contributions of multiple resonances can be summed to obtain the reaction rate. This latter is often dominated by resonances located in the aforementioned Gamow energy window, notably for E_r values close to kT. The total reaction rate of a single reaction, on the other hand, must also include the contribution of broad resonances as well as other minor contributions (non-resonant processes, sub-threshold resonances, amplitudes interference...).

A compilation of experimental reaction rate estimations has historically been produced and compiled by Willy Fowler and collaborators up to 1988. Although the originally reported values are still a reference, the European NACRE collaboration[41] proposed new values in an eponym compilation 10 years later. The first tabulated compilation of the recommended experimental reaction rate values for A=20 to 40 nuclei was proposed in 2001[43]. Around 2010, reaction rates estimated using Monte-Carlo techniques were produced and compiled by Iliadis and collaborators[44].

2.3 The background(s) challenge

The main limiting factor hindering the measurement of low-yield astrophysically relevant nuclear reactions is the very low signal-to-background ratio. In general, γ and neutron background activity are from different sources such as cosmic rays, long-lived activity of unstable isotopes in the surroundings of the measurement site, or even induced by the accelerator beam. The neutron background is the main concern for ^{22}Ne(α,n)^{25}Mg cross section measurements. For this specific case, the main background source is induced by (α,n) reactions from unstable heavy nuclear,

as a result of uranium and thorium decay chains or obtained as a product of cosmic rays interaction with air molecules[46]. These neutrons are often not distinguishable from those from the neutron signals coming out from the nuclear reactions in the experiment when both cover the same energy ranges unless some further filtering analysis methodology is used (coincidence analysis, ToF..). The most straightforward method to suppress environmental neutrons before they hit the detector is by thermalization followed by absorption in a medium called a moderator. This latter must be composed of low-mass elements (preferably hydrogen) that kinematically maximize the energy transfer at each scatter, thus requiring a lower distance to bring the neutron into the thermal energy of 0.025 eV. The moderating medium is often doped with chemical elements that are efficient at absorbing thermal neutrons such as boron-10. The shielding thickness must be adapted to the environmental conditions related to neutron production and energy: for example, neutrons with an energy of 1 to 3 MeV have a mean free path of a few cm in water [47]. It is also possible to decrease the neutron background by performing the experiment in deep-underground environments (decommissioned mines, tunnels under mountains...) which are naturally shielded from cosmic rays and their neutron-producing cascades. Only spontaneous fission of ^{238}U found in the surrounding rocks and (α,n) reactions may therefore contribute to the total background rate [48][49].

The deep-underground LNGS facility where the study of the SHADES detectors' intrinsic activity is discussed in Section 4.1. In this environment, the intrinsic radioactive activity of the materials composing the detectors becomes distinguishable (see Figure 2.5). This is why the housing material must be carefully chosen during the proof of concept phase of the experiment. Often, natural decay families such as those of ^{238}U and ^{232}Th found in aluminum or iron emit α-particles contribute to the neutron count rate in ^{3}He base proportional counters. The same phenomenon is observed in liquid scintillators where α-activity shows the same signature as neutrons (see Section 4.3). The other source of unwanted background occurring during nuclear reaction experiments is the ones produced induced by the interaction of beam particles with different materials along the accelerator beamline. Additionally, contamination of undesirable chemical elements that are not relevant to the conducted nuclear reaction experiment is present in the target under study. These "impurities" provoke the activation of reaction channels producing byproducts that may mimic the signal from the reaction under study. In the case of astrophysically relevant (p,γ) nuclear reactions, it is often ^{19}F contamination that causes the most damage to the experimental spectra by producing very high cross-section resonances at 224 and 340 keV. The ^{22}Ne(α,n)^{25}Mg relevant for this work is more concerned by (α,n) induced reactions. It is often hindered by carbon and oxygen isotopes found in the beamline which are probably remnants of previous experiments that used enriched gas targets. A list of most occurring (α,n) induced nuclear reactions in experimental setups is presented in Table 2.1.

2.4   Experimental study of ^{22}Ne(α,n)^{25}Mg

All the C and O available at the beginning of H burning are transformed into N since ^{14}N(p,γ)^{15}O is the bottleneck of the CNO cycle. While ^{12}C and ^{16}O productions are due to helium burning, their abundances are heavily dependent on the reaction conditions like pressure and temperature and thus the mass of the star. Indeed, the ^{12}C/^{16}O ratio is < 1 for massive stars, following the increased production rate of

Table 2.1: Usual α-beam induced nuclear reactions in particle accelerators [50]. The main contribution originates from reactions involving boron, carbon, and oxygen as target nuclei because of Coulombian repulsion increasing strength at higher Z-values.

α-induced reactions	Q-value (MeV)
$^{10}\text{B}(\alpha,\text{n})^{13}\text{N}$	1.06
$^{11}\text{B}(\alpha,\text{n})^{14}\text{N}$	0.16
$^{13}\text{C}(\alpha,\text{n})^{16}\text{O}$	2.2
$^{17}\text{O}(\alpha,\text{n})^{20}\text{Ne}$	0.59
$^{18}\text{O}(\alpha,\text{n})^{21}\text{Ne}$	-0.7
$^{47}\text{Ti}(\alpha,\text{n})^{50}\text{Cr}$	-0.32
$^{49}\text{Ti}(\alpha,\text{n})^{52}\text{Cr}$	1.21
$^{57}\text{Fe}(\alpha,\text{n})^{60}\text{Ni}$	1.35
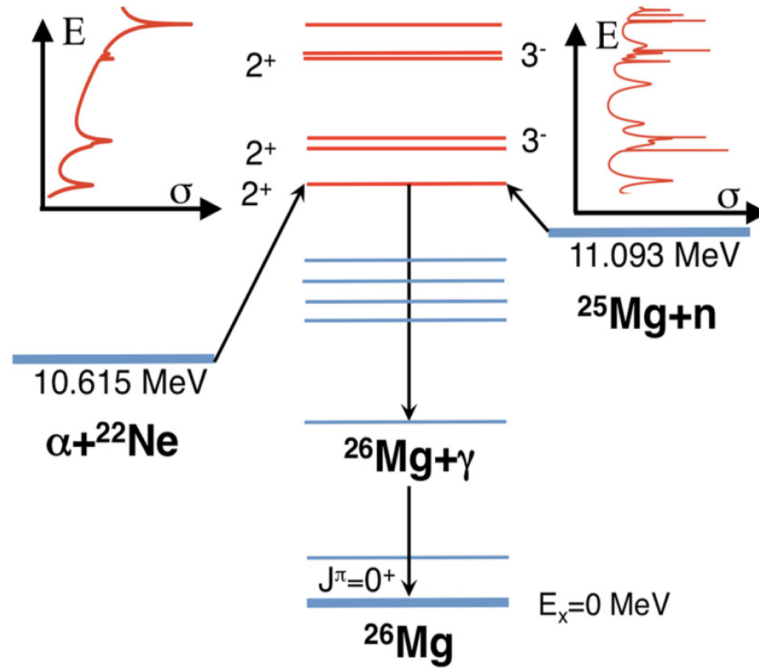
Figure 2.6: $^{22}\text{Ne}+\alpha$, ^{26}Mg and $^{25}\text{Mg} + \text{n}$ energy levels scheme. Reprinted from [51].

the $^{12}\text{C}(\alpha,\gamma)^{16}\text{O}$ nuclear reaction. All the remaining ^{14}N can form heavier elements through $^{14}\text{N}(\alpha,\gamma)^{18}\text{F}(\beta^+ \ \nu)^{18}\text{O}(\alpha,\gamma)^{22}\text{Ne}$ by α-particles capture during the helium burning phase as suggested by [3]. Two reactions enter then in competition for the conversion of ^{22}Ne : $^{22}\text{Ne}(\alpha,\gamma)^{26}\text{Mg}$ and $^{22}\text{Ne}(\alpha,\text{n})^{25}\text{Mg}$. This latter, which is the main focus of the SHADES experiment, has a negative Q-value of -0.48 MeV with an effective α-energy threshold of 565 keV. It is very active at the end of helium burning when T > 0.25 GK. It is a crucial source of neutrons feeding the nucleosynthesis of heavier elements of A ranging from 60 to 90 by other reactions that require rather low-energy neutrons.^{22}Ne found in the universe therefore mainly comes from AGB and massive stars and is responsible for the creation of two magnesium isotopes, namely ^{25}Mg and ^{26}Mg.

Since the $^{22}\text{Ne}(\alpha,\text{n})^{25}\text{Mg}$ nuclear reaction is an important neutron source feeding the "weak" s process, the determination of its cross-section at low energies is crucial
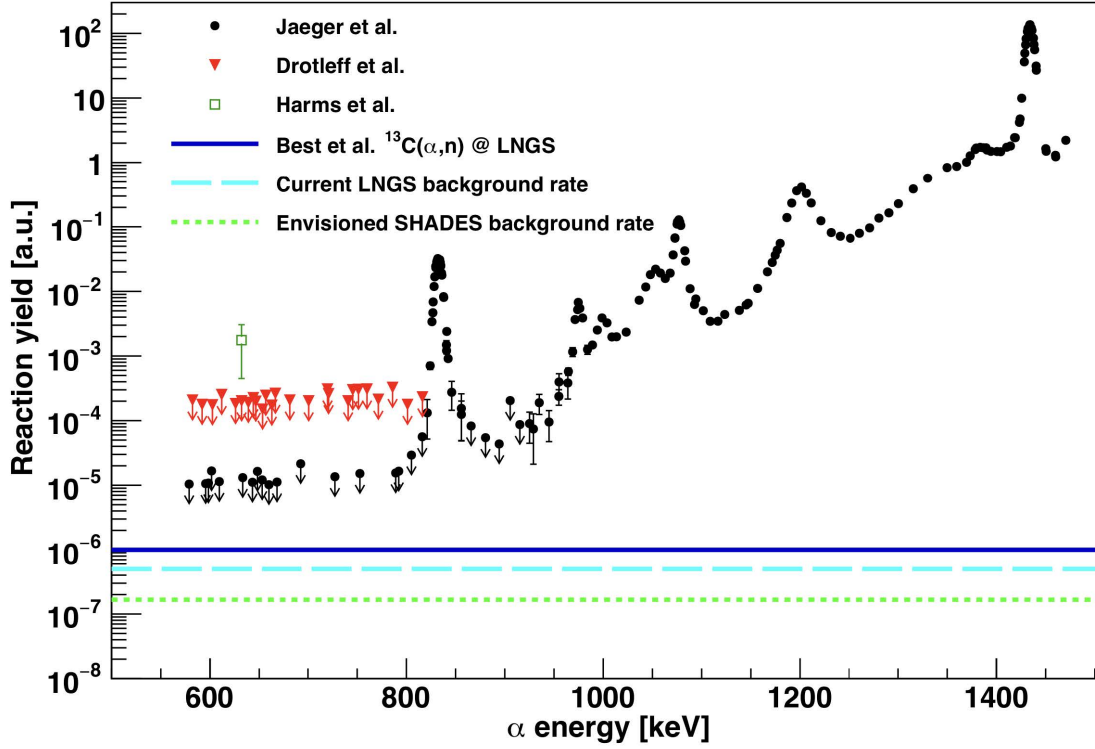
Figure 2.7: ^{22}Ne$(\alpha,$n$)^{25}$Mg experimental yield measurement literature results [54][53][52]. The 3 colored horizontal lines represent different background rates in the deep-underground facility of LNGS [55]. Originally from [56].

for the building of a general astrophysical model that describes the nucleosynthesis of heavy elements in stars. There have been many attempts to perform this measurement in the past through both direct and indirect nuclear reactions. The majority of the direct cross-section measurements at low energy were achieved in the labs of the University of Stuttgart [52][53][54]. These measurements were conducted using gas targets surrounded by ^{3}He proportional counters and advanced shielding to help reduce the environmental neutron background. Despite the increasing detection efficiency of the setup at each new measurement reaching $\approx 40\%$, only upper limits of a few 10^{-11} barns were able to be measured since the achieved 72 h^{-1} rate is mostly all natural background activity. In the case of the ^{22}Ne$(\alpha,$n$)^{25}$Mg reaction, both projectile and target have a J^{π} spin-parity of 0^{+}. Therefore, only natural parity states ($J^{\pi} = 0^{+}$,1^{-},2^{+}...) are contributors among which some are those located below 832 keV that are yet to be studied. Energy-wise, the "weak" s process takes place in two major stellar environments :

- **Helium burning phase** : at T = 250-400 MK $\Rightarrow$ resonances below 800 keV.

- **Carbon burning phase** : at T > 800 MK $\Rightarrow$ resonances above 800 keV.

In the second case, the contribution of still-unknown energy states -located below 800 keV- may also strongly contribute to the rate. Measuring resonances below 800 keV is very challenging because of the expected very low neutron production rate at the same order of magnitude as the environmental background.

As of now, there is no evidence of resonance energies of the compound nucleus ^{26}Mg below 832 keV. However, 5 natural parity states may populate the α-channel

[51]. This region is of particularly great importance from an astrophysical point of view since it corresponds to the 420 - 660 keV energy window of the stellar temperature at 300 MK. It is known that there are at least 2 unknown parity states thanks to results from indirect measurements through ^{25}Mg(n,γ)^{26}Mg reactions [51][57]. Nevertheless, the reaction rates and their associated Γ-widths were provided with relatively high uncertainties. The determination of low-energy spin-parity states is crucial since the reaction is only able to populate natural parity states, thus the importance of performing indirect measurements. The 5 parity states < 832 keV found by [51] taking place at relevant stellar energies which may produce resonances are reported in Table 2.2. It has also been shown by [58] that the current uncertainties over the experimental reaction rate values of ^{22}Ne(α,n)^{25}Mg lead to s process yield variation of up to 1 order of magnitude which requires further investigation even for already measured resonances. The neutron natural background is primarily due to cosmic rays interacting with elements found in Earth's atmosphere provoking a cascade of secondary radiation among which are neutrons. It (i.e. the n-background) represents a major source of uncertainty for the reaction rates but that can be suppressed by shielding the detection setup and/or by performing the measurement in a deep-underground environment where the neutron flux is very low. For this reason, the SHADES experiment is taking place at the underground laboratories of Gran Sasso (see Chapter 4). Aside from passive borated-polyethylene shielding, active shielding by anti-coincidence vetoing of events based on the work discussed in Section 5.6 will be applied during the post-process data analysis phase. It is visible from Table 2.2 that measurements [51] and [54] do not agree on the exact energy of lowest energy measured resonance: 832 vs 843 keV. This $\sim$10 keV difference between the two heavily influences the reaction rate since the energy value is contained in the exponential term. Depending on if the two resonances around 830 are considered independent and narrow, or as being one broad resonance corresponding to the same ^{26}Mg energy level, a discrepancy of up to factor 5 is found in the ^{22}Ne(α,n)^{25}Mg reaction rate at T $\approx$ 300 MK [59]. This latter matter strongly pushes towards the investigation of energies around and higher than the 830 keV peak, which is already planned in the experiment following this work. Combining the different shielding techniques (i.e. passive/active) in the extremely deep-underground environment of LNGS is going to help further reduce the neutron background as shown in Figure 2.7. This opens the possibility to have, for the first time, direct access to low-energy states below 830 keV. To achieve the level of sensitivity needed for this experiment, the used apparatus -noticeably the detectors- must be fully characterized before the final measurement. Their internal activity becomes a major limiting factor since it may be of the same order of magnitude as the expected neutron production rate from the ^{22}Ne(α,n)^{25}Mg reaction. In the following chapters, the procedure followed to perform this task in the framework of the SHADES experiment is discussed, as well as the results obtained for particle-type discrimination and active shielding performances.

Table 2.2: ^{26}Mg states properties. Data from [51] except the last row that is from [54].

E_n[keV]	E_x[keV]	E_α[keV]	J^π	n width [eV]
20	11112	589	2+	2095
73	11163	649	2+	5310
79	11169	656	-3	1940
188	11274	779	2+	410
194	11280	786	-3	1810
244	11328	843	N/A	171
235	11319	832	2+	Total = 250 eV

Chapter 3

SHADES detectors

The neutron background activity is the main challenge hindering the direct measurement of ^{22}Ne(α,n)^{25}Mg reaction cross-section below 830 keV as discussed in Section 2.3. Many shielding techniques are used to overcome this challenge such as moving the setup into an underground facility, using borated-polyethylene around the detectors, or post-process discrimination of events based on coincidence/anti-coincidence information. Besides the use of all these techniques, the SHADES hybrid experimental setup uses EJ-309 organic liquid scintillators (see Section 3.3) as moderators thermalizing the reaction's neutrons thus increasing their detection probability by ^{3}He-filled proportional counters. The full detection array consists of 12 scintillators forming a ring in between an inner 12 units and an outer 6 units of 10 bars pressure 1" $\varnothing \times$ 25 cm cylindrical stainless steel housing ^{3}He-filled proportional counters rings (see Figure 3.1). A windowless, recirculating gas target in which the reaction takes place goes through the center of the array. The 10 cm thick borated-polyethylene structure acts as both holder of the detectors and shielding against the external neutron background. The novelty of the SHADES setup resides in its ability to quantify the energy of incident reaction neutrons before thermalization using the EJ-309 scintillator properties and time coincidence analysis. Since the setup can provide timestamp information (i.e. the time at which events are detected) allowing the establishment of correlation (or not) between events hitting the scintillators and those captured by the ^{3}He counters. This latter procedure helps in the discrimination process by applying a cutoff on high-energy neutrons, in particular, those from the following beam-induced reactions :

- ^{11}B(α,n)^{14}N (Q=158 keV)

- ^{10}B(α,n)^{13}N (Q=1059 keV)

- ^{13}C(α,n)^{16}O (Q=2216 keV)

Similarly, time coincidence filtering can also be used to discard events due to the detectors' internal activity investigated in Chapter 4 through ^{3}He-Scintillator time coincidence analysis as conceived and tuned in Chapter 5. Both the data acquisition system (DAQ) and the scintillators configuration used throughout the EJ-309 liquid scintillators characterization work did slightly vary between measurements. An overall description of the experimental setup is therefore reported in each case as can be seen in the following chapters. Also, data from a 13$^{\text{th}}$ scintillator put outside of the main array -backup unit- is also taken and analyzed throughout this work
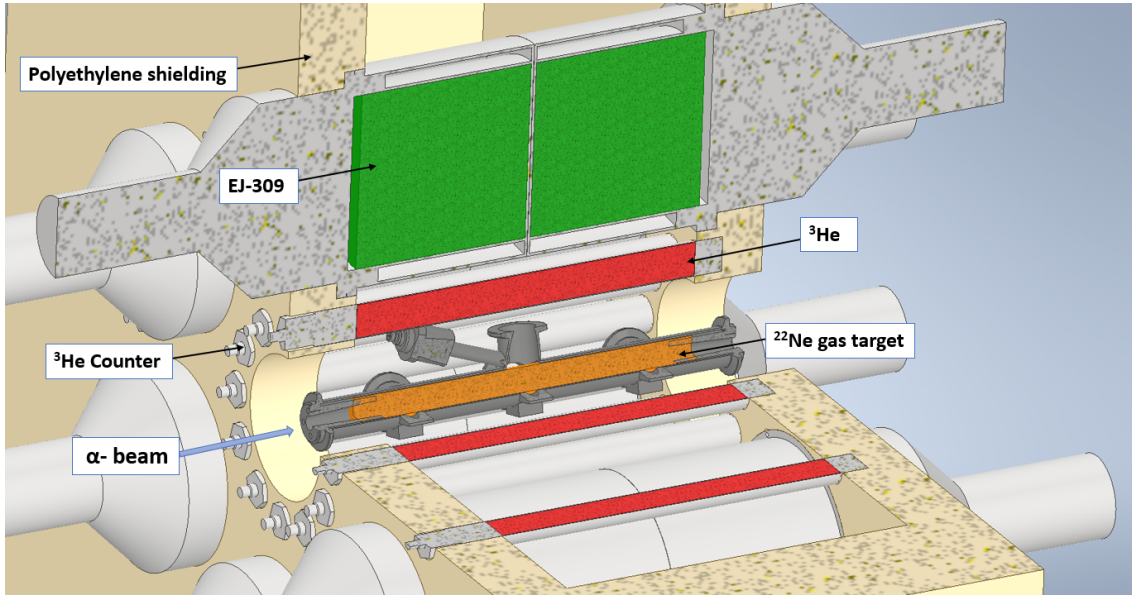
Figure 3.1: Lateral cut-view of the SHADES detection array. Reprinted from [60].

to assess the performance of the shielding. The full experimental detectors setup is therefore often referred to using the 12+1 units terminology.

3.1 Fundamentals of neutron detection

Depending on the type of detectors used, efficient neutron detection can be achieved by either elastic scattering or through direct nuclear reactions. In this latter case, the neutrons interact with a nucleus of the medium or with those present within as contamination or doping, producing energetically charged particles, mainly protons and α-particles. Having a charge facilitates the detection using typical radiation detectors based on charge or light collection and multiplication. The cross-section of neutron detection through nuclear reactions is heavily dependent on energy. For this reason, depending on the energy range, specific techniques are used to detect neutrons. Usually, very low energy neutrons show a higher cross-section (see Figure 3.3), hence the particular interest they are given during the development of the SHADES detection array. Radiative neutron capture X(n,γ)Y is often the outcome of neutron interaction in materials when thermalized. This process also allows the construction of neutron shielding or at least the attenuation of their initial energy. Nevertheless, it is more common to detect neutrons when the emitted secondary radiation is a charged particle: X(n,p)Y, X(n,α)Y, and X(n,Z)Y (fission). This is particularly the case of proportional ^{3}He counters discussed in Section 3.2. On another hand, fast neutron detection may go through direct nuclear recoil using, for example, a ^{4}He proportional counters which present higher efficiency between 1 and 3 MeV region [61], or, as in the case of the SHADES experiment, through thermalization (i.e. reducing their energy to < 0.5 eV) followed by capture in a ^{3}He counter. Even though neutrons from ^{22}Ne(α,n)^{25}Mg themselves have unbounded energies in this context, this high cross-section for low-energy neutron capture leads to the use of moderation material to lower their energy, increasing the setup global efficiency. Neutrons having energies under the cadmium cutoff of 0.5 eV are called "slow neutrons" [62]. The energy of secondary radiation resulting from slow neutron-induced reactions is often enough for direct detection. Since their energy is very low,

Figure 3.2: 1" inch $\varnothing$ × 25 cm length cylindrical 10 bars pressure ^{3}He-filled proportional counter with stainless steel housing. The same model and dimensions as those used for underground neutron background measurement, ^{13}C(α,n)^{16}O direct cross-section measurement [63], and in the SHADES project.

the Q-value has to be strictly positive to allow such reactions to occur.

As previously stated, the cross-section heavily decreases with increasing neutron energies. In some detector types, it is the recoil energy transferred to a charged particle that is detected. This is the case of EJ-309 organic liquid scintillators that use this elastic scattering-based technique to reconstruct the initial neutron energy (see Section 3.3). Kinematics calculations dictate that hydrogen is the most efficient moderator since neutrons may lose all their energy in one collision following an inelastic scattering interaction. In the same way, only a part of the energy is transferred by the neutron when interacting with heavier nuclei as shown in :

$$E_{R_{max}} = \frac{4A}{(1 + A)^2} \cdot E_n \tag{3.1.1}$$

where $E_{R_{max}}$ is the maximum target nuclei recoil energy, A its atomic mass, and E_n is the incoming neutron energy. The transferred energy is here maximized by considering a scattering angle $\vartheta = 0°$. In some cases, E_n is high enough that the inelastic scattering provokes an excitation of the target nuclei to a higher energy state $X(n, n)X^*$. this latter quickly decays to the more stable ground state emitting a γ-ray. This process generally does also make the neutron lose a large part of its energy allowing the establishment of high-energy neutron shielding and moderators for both safety or detection purposes.

3.2   Neutron detection with ^{3}He counters

The ^{3}He proportional counters are a type of gas-filled detector mainly used for neutron detection. They are often produced in the form of stainless steel or aluminum tubes (see Figure 3.2). Depending on the use case, one of the two housing materials may be preferred. Works such as [45] report that using iron units has, for example, heavily suppressed the internal activity of the detector. The internal background reduction is particularly crucial for low count rate measurements such as that of ^{22}Ne(α,n)^{25}Mg cross-section under the 830 keV resonance the SHADES experiment is focused on. ^{3}He itself is obtained through tritium decay. This latter being a rare by-product of ^{233}U, ^{235}U, and ^{239}Pu fission in nuclear reactors makes it expensive to produce hence also raising the cost of ^{3}He production. Its efficient neutron detection capabilities -under certain conditions- do however make it widely used in low cross-section neutron detection experiments. Neutron detection by ^{3}He-filled proportional

counters is based on their absorption by an isotope of helium following the nuclear reaction shown in Equation 3.2.1.

$$\ce{^{3}_{2}He} + \ce{^{1}_{0}n} \ \rightarrow \ \ce{^{3}_{1}H} + \ce{^{1}_{1}p} \ (\text{Q-value} = 764 \text{ keV}) \qquad (3.2.1)$$
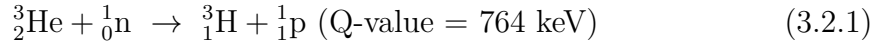
They are called proportional counters rather than detectors because of their limitation of only being able to provide the count number of the captured neutrons without the associate energy information. Using an adequate DAQ setup does however allow the extraction of further useful information such as individual events timestamps. The proportionality -mentioned in their name- refers to the proportional light yield production depending on the capture reaction products energy rather than that of the incoming neutron. When a slow neutron -for which ^{3}He counters have a high detection efficiency- enters the detector, the reaction products are emitted in opposite directions with an energy of always 573 keV for the proton and 191 keV for the triton (tritium nucleus). The cross-section of this reaction is $\sim$5.3$\times$10^3 barns for 1 eV neutrons, with a $1/v$ energy dependency (see Figure 3.3). When both reaction products lose the totality of their energy within the ^{3}He gas, a 764 keV signal -after calibration- is produced. There is however a non-negligible probability for one of the products to hit the metallic housing of the detector to which they transfer a fraction of their energy. This phenomenon -called the wall effect- shapes the eponym region located between $\sim$180 to $\sim$660 keV in the ^{3}He typical spectrum through a convolution of the proton and triton partial energy deposition contributions. The amplitude threshold highlighted in Figure 3.4 corresponds to the minimum possible detectable energy transfer that occurs due to thermal neutrons: the produced tritons depositing their full energy in the ^{3}He gas while the proton energy is almost fully lost within the housing material (i.e. Stainless steel or aluminum). Below around 180 keV γ-ray interaction with the gas and electronic noise signals dominate the spectrum. The clear separation between the two regions allows reliable particle-type discrimination as previously stated in the beginning of the section. It is however not uncommon to couple this property with signal rise time analysis to improve the dichotomy between the two particle types [64]. Also, even though this type of detector does not provide information on the incoming neutron energy, the ability to discard γ-rays as well as the availability of timestamp information allow the establishment of the anti-coincidence-based active shielding as discussed in Section 5.6.

3.3 EJ-309 organic liquid scintillators

The process of light emission by certain materials after being hit by ionizing radiation is called scintillation. Collection of this light through more or less complex experimental devices is a well-understood and reliable particle detection technique. The light is then converted to charge or voltage forming a signal that is then sent to and collected by the DAQ. However, not all DAQs can record the time characteristics of the signals produced by the detectors. When available, the signals (called waveforms) are recorded in shape using regular time intervals. They not only allow the counting of individual events but also provide information -based on their shape- about particle type and energy. The latter is made possible thanks to the fact that the amount of scintillation light produced/collected is often proportional to the particle's initial energy. It is also possible, as shown in Section 3.5, to further process the signals through Pulse Shape Discrimination (PSD) leading to the labeling of
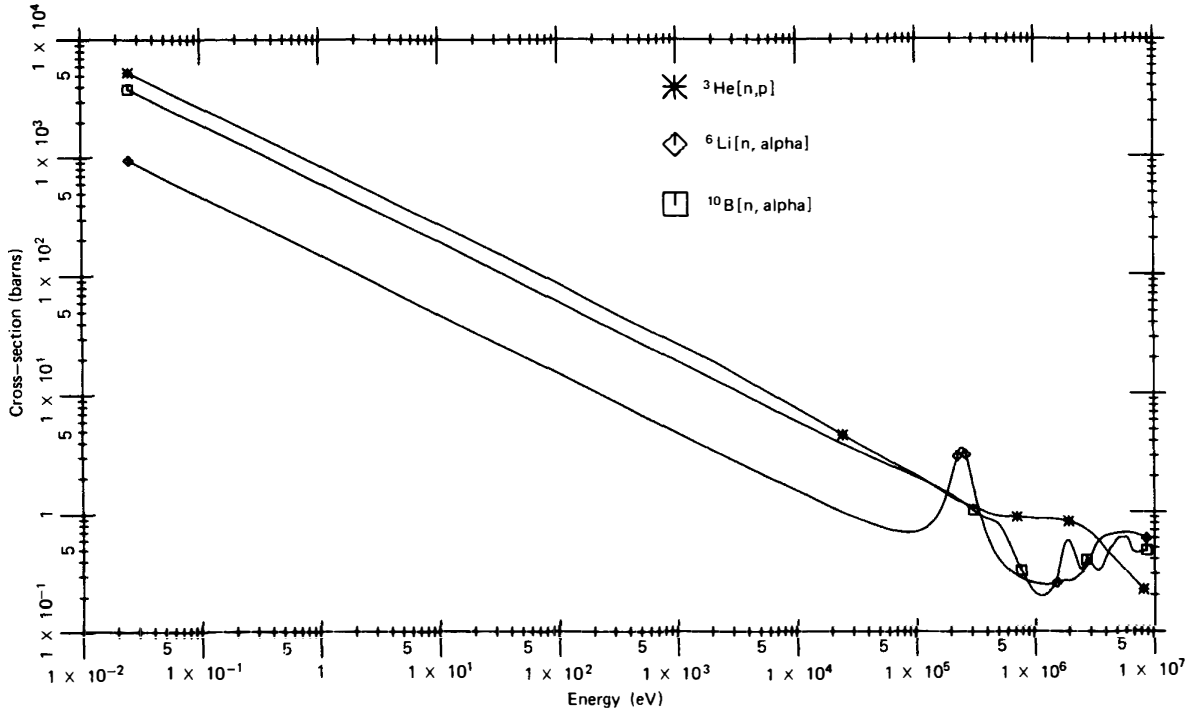
Figure 3.3: Neutron capture cross-section dependency on energy in different gas-filled proportional counters. Reprinted from [65].

individual events with their corresponding particle type. To suit detection by scintillation, the active material on which the detector is based must be able to convert into detectable light the kinetic energy of charged particles with maximum efficiency. This conversion process must also ideally preserve a certain proportionality between the amount of light collected and the charged particle's initial energy over a wide range of energies. The material has also to be transparent to the light wavelengths it emits following the scintillation process to ensure optimal light collection. The duration of luminescence produced in the material for each signal must be short enough to produce a unique fast pulse. Also, it (i.e. the material) must have a refraction index that is similar to glass ($\sim$1.5), this will ensure an optimal coupling of the scintillation emitted light to the photomultiplier tube or other amplification components. Inorganic materials such as alkali halide crystals show a better light output and linearity but their response time is in some way very slow, making them more often used for γ-ray spectroscopy thanks to the higher Z-value constituents. On another hand, organic scintillators, have a lower light yield but a faster pulse decay time. The fact that they contain hydrogen makes them an optimal choice for β and neutron spectroscopy (see Equation 3.1.1).

The scintillators in use for the SHADES experiment are based on an organic liquid scintillator commercially known as EJ-309. It is a mixture of 90.6% carbon and 9.4% hydrogen with a density of 0.959 g/cm^3. Its low toxicity and high flash point (i.e. ignition temperature) of $F_{EJ309} = 144$ °C make it an ideal alternative to the commonly used EJ-301 ($F_{EJ301} = 25$°C) for measurements in underground environments where safety guidelines are often more restrictive. Also, EJ-309 is known for having a relatively good light output of around 75% of that of anthracene (or 52% when doped with 5% natural boron). This translates to a scintillation efficiency of around 12.5×10^3 photons/1 MeV e$^-$ (according to the manufacturer).
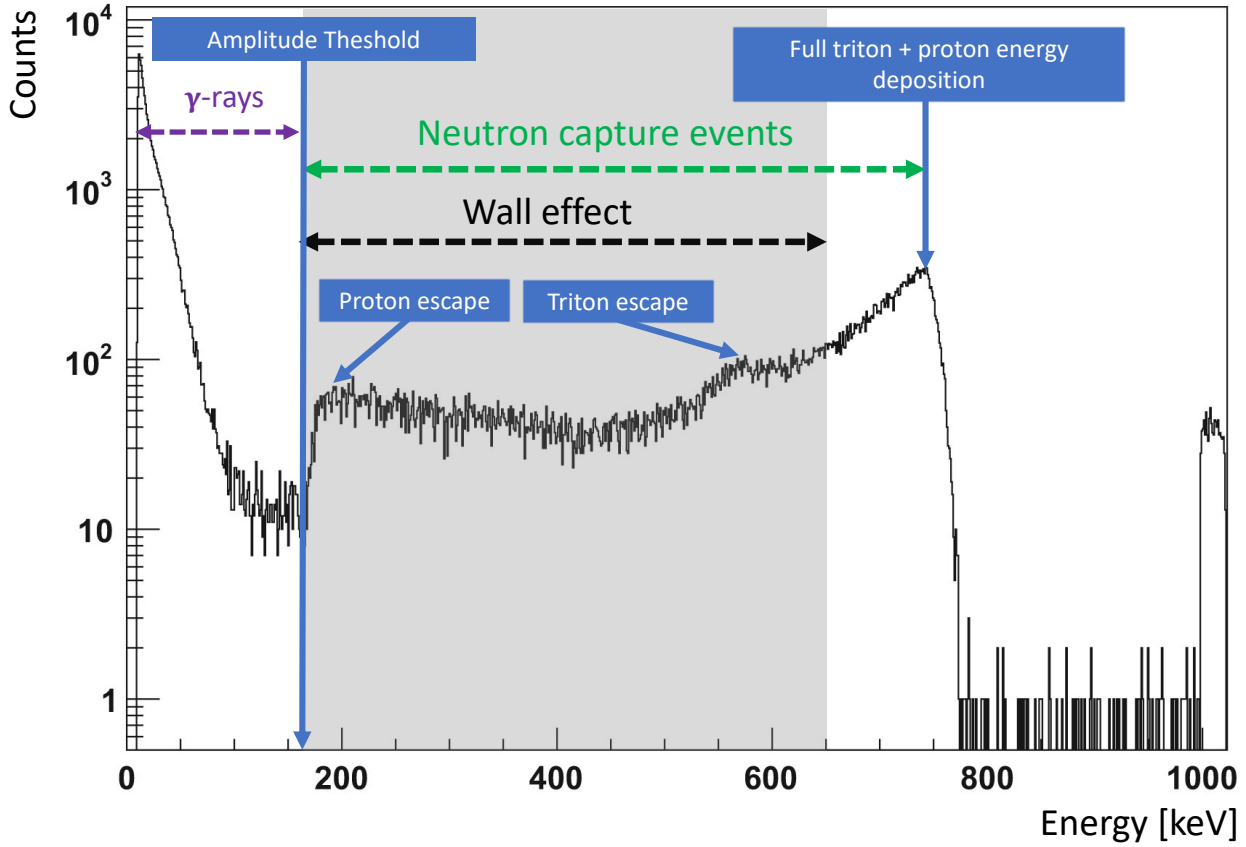
Figure 3.4: Characteristic ^{3}He counter spectrum showing the origin of different features. The dashed green double arrow is the energy range where the signal is due to the capture of 1 neutron. In the dashed black double arrow is the range of the signals that are due to the reaction products hitting the counter wall (see Equation 3.2.1). γ-rays and electronic noise produce events in the region shown with a dashed purple double arrow. Events above 800 keV are due to the pile-up of 2 signals or more. Spectrum adapted from [66].

It also has a good reflective index of 1.57 and the maximum wavelength of the emission spectrum at 424 nm. The units used for this work are delivered with a 10-stage ETL9390 photomultiplier (see Figure 3.5). EJ-309-based liquid scintillators do however not produce full energy peaks because of their composition of mainly low Z chemical elements (C and H) (see Figure 3.6). The incident γ-rays are often not able to fully deposit in their energy. This type of detector is known for achieving good neutron/γ-ray discrimination. In the SHADES setup, the scintillators are primarily meant to act as neutron moderators. For this reason, the non-doped EJ-309 model (i.e. without boron) is used, since neutrons are thermalized but not absorbed, allowing them to later be captured by the surrounding ^{3}He counters with a higher cross-section.

3.4 DAQ setup & gain match

The study of the SHADES setup response to γ-rays involves all 12+1 units of 5"×5" cylindrical EJ-309 scintillators (see Figure 3.5). A CAEN SY5527 power supply was used to simultaneously provide a negative voltage for each detector. It is remotely controlled by a dedicated software named *GECO*. The rest of the DAQ system is
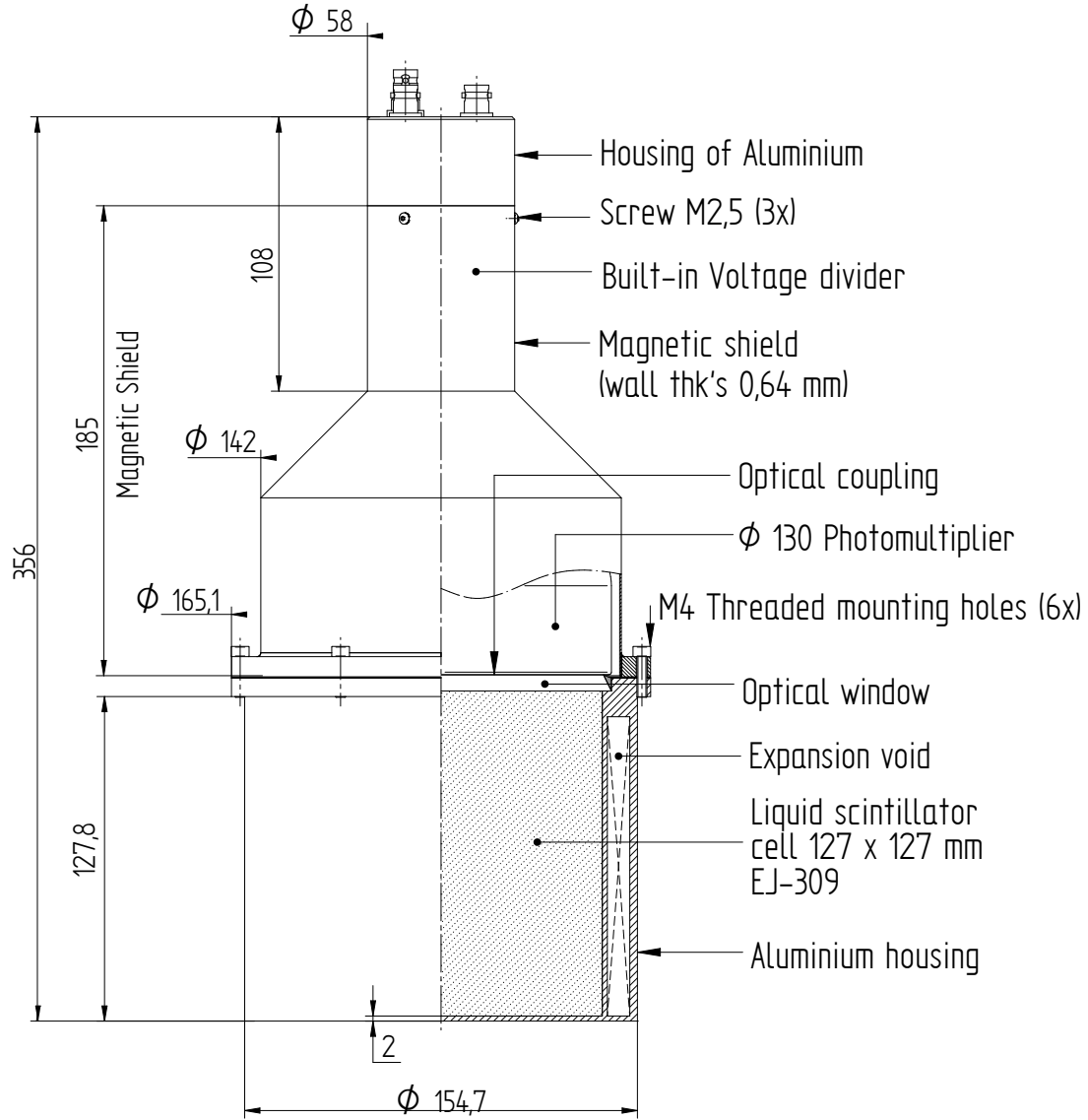
Figure 3.5: The technical drawing of an EJ-309 liquid scintillator unit used in this work. Courtesy of Scionix Holland B.V. ™.

composed of 3×CAEN 16 channel 14-bit 250 MS/s V1725SB digitizers running the DPP-PSD firmware. They are mounted on a dedicated VME crate connected to a computer through a USB 2.0 cable, and to the scintillators through 12+1 lemo cables. The signal acquisition and saving are achieved using the CoMPASS software [67] provided by the manufacturer. Alongside the visualization of individual signals, this latter also allows a direct fitting of the energy spectra, thus facilitating the gain match procedure. Different units of the same type of organic liquid scintillators may show a different response for same-energy γ-rays depending on many parameters such as the applied electrical voltage. This implies that in the case of the simultaneous use of multiple detector arrays as for SHADES, it is important to even this response for each unit to match the rest of the array in order to ease the calibration procedure. Indeed, this allows the establishment of a unique energy calibration applicable to all units. The procedure of tuning different same-type detectors to obtain the same light response for same-energy particles is called gain matching. It is achieved by varying the value of the voltage applied between its electrodes, hence changing the signal amplitude of the detected particles. This process results in an overall shift
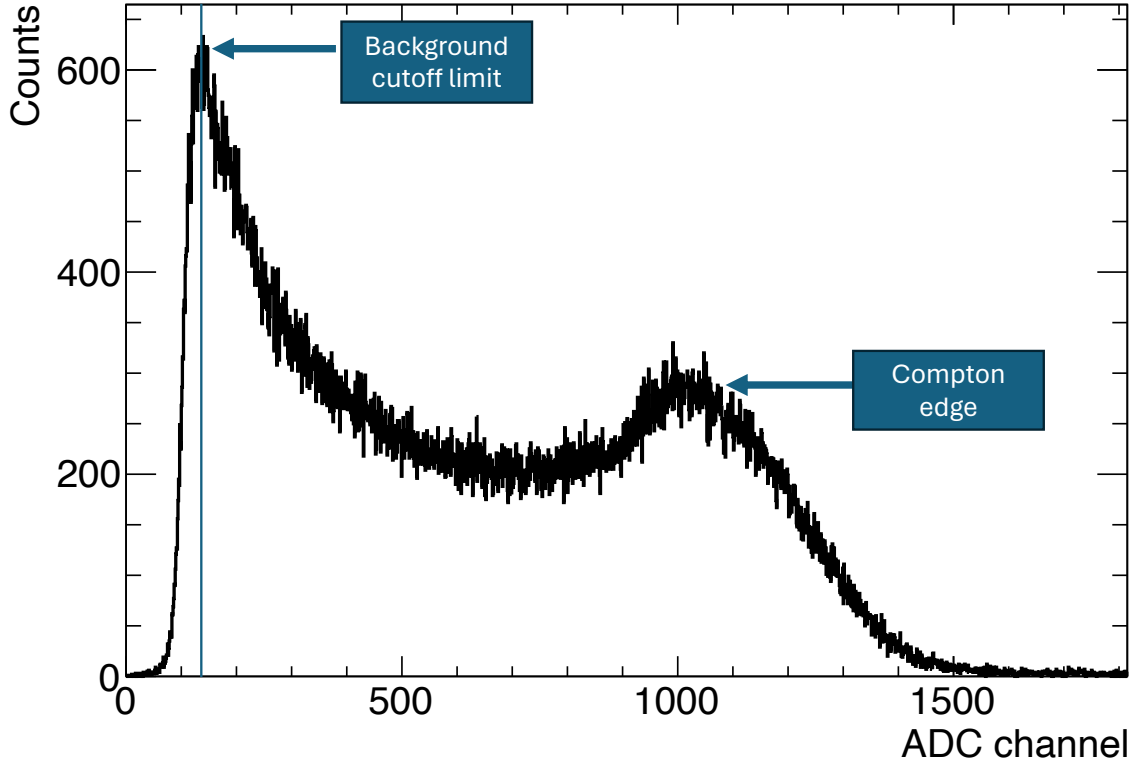
Figure 3.6: ^{60}Co spectrum obtained by 1 EJ-309 liquid scintillator using the gain match calibration parameters reported in Section 3.4. The energy of the signals is represented using the default ADC channel labeling of the pulse height.

and stretching of the energy spectrum (labeled in ADC channels). For this work, the spectrum of a 158 kBq ^{60}Co radioactive source is used as a reference. The measurement took place in the nuclear astrophysics laboratory of the Federico II University of Naples (surface) with the SHADES 13 EJ-309 liquid scintillators units using the following CoMPASS DAQ parameters (defined as in Figure 3.8) :

- Record length : 992 ns.
- Pre-trigger : 96 ns.
- Polarity : Negative.
- DC Offset : 5%.
- Energy Coarse Gain : 10 fC / (LSB × V$_{pp}$).
- Input Dynamic : 0.5 Vpp.
- Threshold : 300 lsb.
- Trigger holdoff : 1024 ns.

For this work, the gain matching of the detectors is performed in two steps. All detectors were first placed on the top of a wooden table in a circular arrangement around the ^{60}Co source and then connected to both the power supply and DAQ system. The voltages applied to each unit are manually tuned such as the spectrum's Compton edge is located at around ADC Channel 1000 (see Figure 3.6). The live spectrum visualization and fit available in CoMPASS allows the estimation of the exact Compton edge's bin value in the energy spectrum that corresponds to the applied voltage. The second phase of the gain match procedure consists of varying the voltage applied to each detector in a ±100 V range with a $\delta V = 10$ V steps and recording the change in the Compton edge position. The resulting points are fitted

with a quadratic function giving the exact voltage value at which the Compton edge is located at the targeted ADC channel of 1000 (see Figure 3.7). Some detectors stop responding below or after a certain voltage value, (e.g. +90V for unit n° 5), such points are not considered for the Compton edge fit procedure. The obtained optimized voltages for each unit are reported in Table 3.1. Those last voltage values are used throughout the rest of this work.
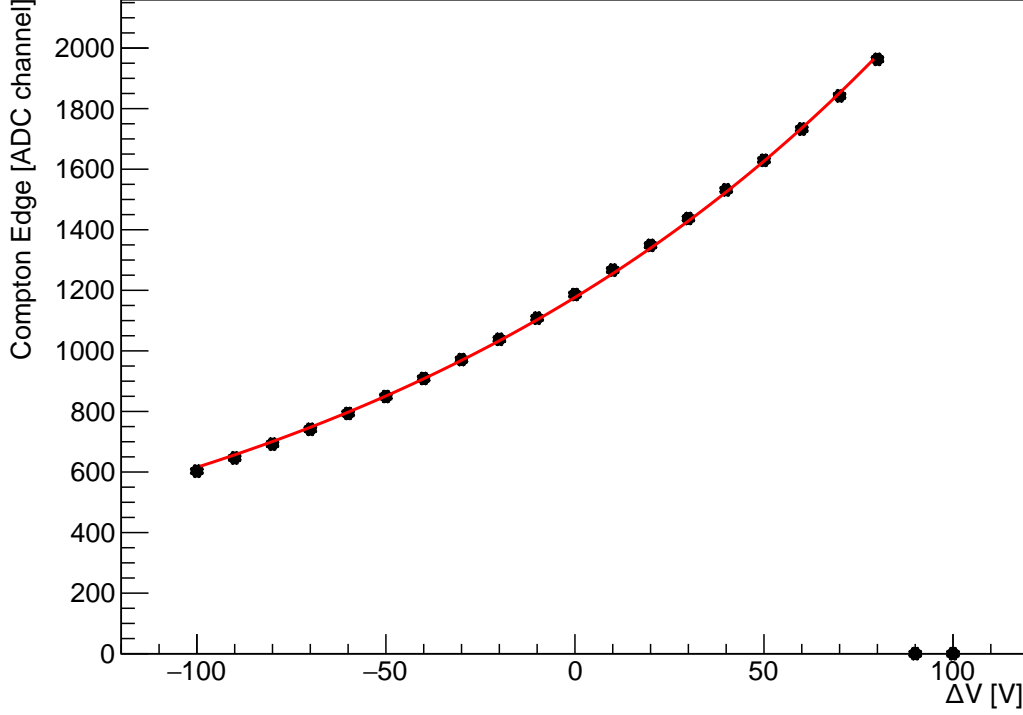
Figure 3.7: EJ-309 Detector (unit n° 5) response for voltage variation around the pre-gainmatch values. In red is the result of a fit performed on the points using a quadratic function.

3.5   Pulse Shape Discrimination analysis

The signal produced by the used DAQ setup is a sampling of the voltage each 4ns over a customizable duration labeled in the DAQ software as "Record length". When the voltage varies by a given percentage from a value calculated by averaging a few successive samples (called baseline), a signal recording is triggered. This saves the voltage values starting from a certain number of samples before the trigger, up to the total allowed wavelength duration. The signal shape is generally a peak with a long tail (see Figure 3.8). Its corresponding light yield variation in time can be represented as the sum of two decay components: a Fast (few ns) and slow (hundreds of ns) as follows :

$$f(t) = a_1 \cdot f_{fast}(t) + a_2 \cdot f_{slow}(t) \tag{3.5.1}$$

The first component is known to be due to the decay of singlet states in the material while the latter component -corresponding to slow decay- originates from the

Table 3.1: Optimal voltage values applied for each detector.

Detector n°	Optimal Voltage [V]
01	794
02	975
03	1108
04	1080
05	1025
06	859
07	829
08	1179
09	999
10	848
11	1049
12	1101
13	1111

decay of long-lived triplet excitation states [65]. Its contribution to the light output compared to that of the fast component (i.e. $\frac{a_2}{a_1}$) depends on the particle type. Even though the EJ-309 organic liquid scintillators of the SHADES array are primarily used as moderators, their γ-neutron separation properties can be exploited for further analysis and to boost the setup efficiency through active shielding (see Section 5.6). The PSD performance does however vary depending on the parameter choice and its optimization for each use case scenario (high γ-rays background, presence of neutrons or α-particles,... etc.). Since neutrons are the relevant particles in this experiment's framework, the PSD optimization targets the achievement of a maximum neutron/γ separation justifying the need for a strong neutron source. The activity of a 3.31 MBq AmBe ($\sim 2 \times 10^3$ neutrons/s) source is measured using one scintillator (unit n°5) placed inside a 10cm thick lead box in the surface lab to reduce the amount of environmental γ-rays hitting the detector. This measurement is performed using the CAEN V1725SD digitizer. This latter is connected to the DAQ computer using optical link cables. Also, some of the DAQ parameters are here changed from the values reported in Section 3.4 while also saving the individual waveforms information corresponding to each event. This should, in principle, not have any influence on the optimal voltages obtained from the gain match procedure. The modified CoMPASS DAQ parameters are :

- Energy Coarse Gain : **40 fC / (LSB × Vpp)** .
- Input Dynamic : **2.0 Vpp**.

Even though "classical" PSD algorithms take different approaches to discrimination between particle types based on the produced signal shape, the difference is mostly always found in the decay time (i.e. the pulse tail). In any used technique, the tail integral must consistently be normalized to the total pulse since it is also energy-dependent. The most common PSD technique used for this detector type is charge integration. It functioning and optimization for the used EJ-309-based detectors are discussed below. The use of alternative methods is also investigated in the last part of the section.
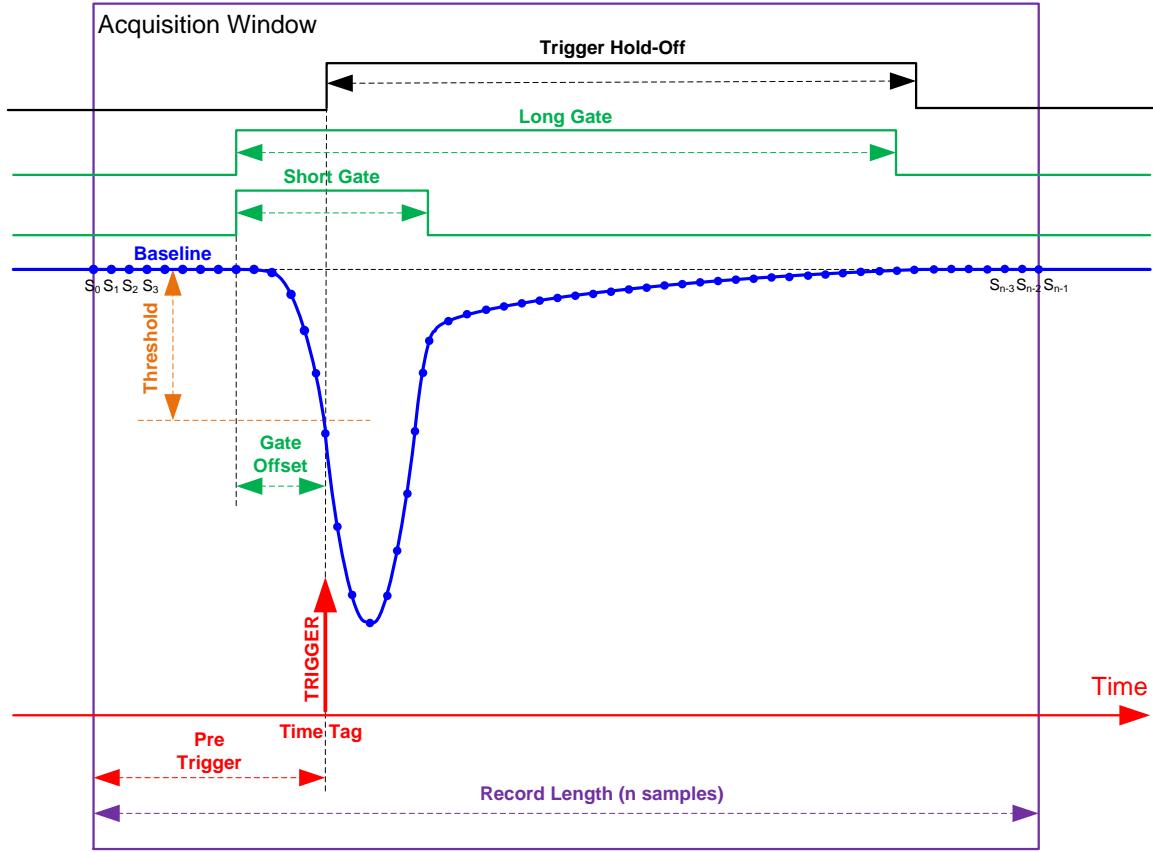
Figure 3.8: Representation of different PSD-DPP parameters in a theoretical signal waveform. Reprinted from [67].

DAQ Energy

To obtain a better resolution, the energy of each detected particle is taken as what is considered the total integral of the pulse (see long definition in Section 3.5) it produces instead of the maximum amplitude. The improvement in energy resolution doing so can clearly be noticed by comparing Figures 3.6 with Subfigure 3.13(a) which both are obtained from a ^{60}Co source. The energy axis has therefore a voltage per time dimension and is hereafter labeled "DAQ Energy", and not ADC Channels (i.e. the amplitude). On another hand, While the beginning of a pulse is easily identifiable using trigger information (leading edge method), the tail slowly decays in time windows that are energy-dependent. Since the energy of the incoming particle is defined as the integral over the long gate L in the PSD technique called double gate method [68] [69], the integration range is taken as L, the long gate value maximizing neutron/γ-rays separation (see figure 3.11). Also, the raw waveforms are here processed before the integration by subtracting the baseline. The value of this latter is taken as the average ADC value over the specific ranges in the flat part of the waveform preceding the trigger (see Figure 3.8) or towards the end of the record length where the tail flattens. To avoid negative energy values, the baseline is always estimated in 3 different regions : 0-36, 400-480, and 560-640 ns, then keeping the lowest value. The 0 ns mark is shifted by +96 ns to match the beginning of the gate offset for the upcoming analyses. Two different pulses with equal total integrals but from two different particle types are shown in Figure 3.9.
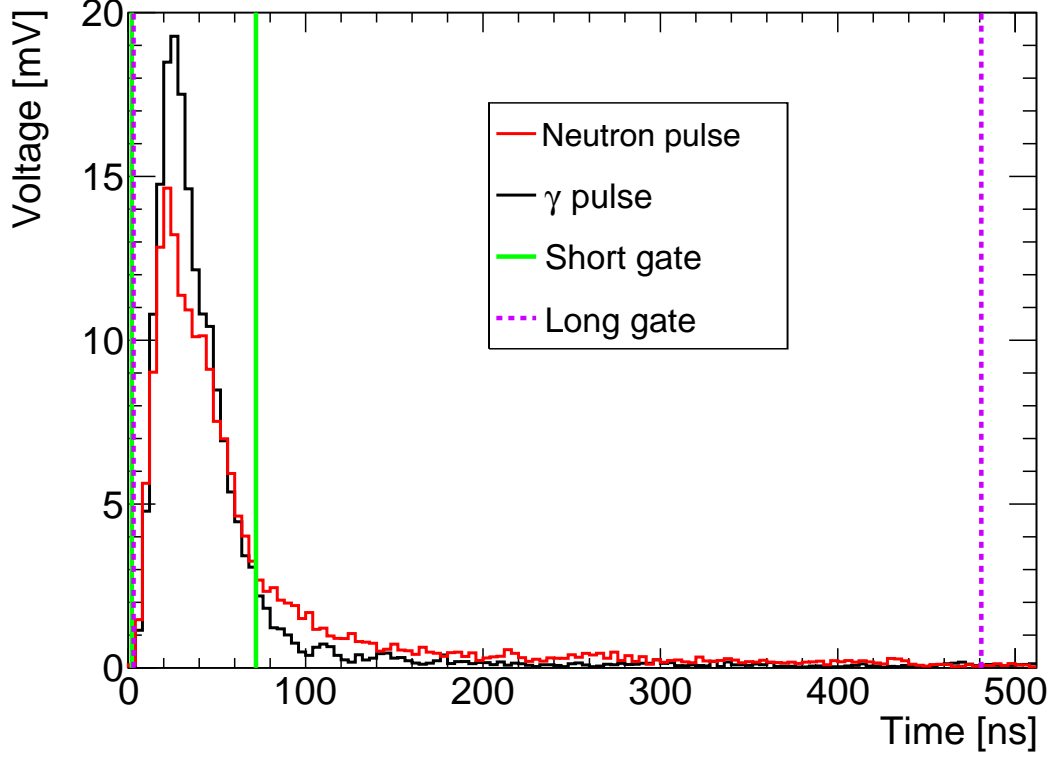
Figure 3.9: Typical neutron and γ same-integral signals produced by the DAQ. The baseline has been subtracted and the ADC channels converted to mV. Neutron signals often show longer decay times at similar energies.

The charge integration method

As a first approach, the acquired AmBe measurement data is analyzed using the charge integration method [70][71]. A technique based on assigning to each waveform a value that is defined as the ratio of two integrals: the total pulse (I_L) and that of a part of its tail ($I_L - I_S$). The integration time window of the first is the long gate L shown in Figure 3.9 while for the second it is the difference between the long and short gate integrals. The distribution of the obtained value -labeled PSD- gives information about the probability of each event belonging to a certain particle type. The PSD parameter is therefore calculated as follows for the charge integration method :

$$\text{PSD} = \frac{I_L - I_S}{I_L} = 1 - \frac{I_S}{I_L} \tag{3.5.2}$$

The PSD value is re-calculated multiple times for the whole data set changing the short and long gates widths. The best values are then chosen such as to maximize the separation between the neutron and the γ-rays peaks in the resulting PSD distribution. The separation is quantified using the Figure of Merit (FoM) value of the distribution [72]. It is calculated for each short/long combination as follows :

$$\text{FoM} = \frac{\mu_n - \mu_\gamma}{2.36 \cdot (\sigma_n + \sigma_\gamma)} \tag{3.5.3}$$

where μ_n and μ_γ are the mean values of the neutron and γ peaks while σ_n and σ_γ are their corresponding standard deviation values. Those values are estimated fitting

(a)

(b)
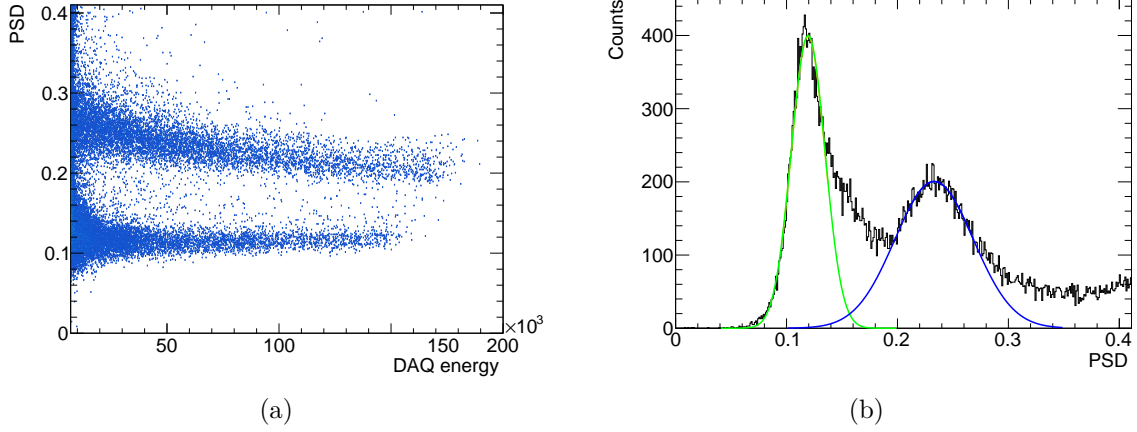
Figure 3.10: Americium-Berylium measurement PSD analysis results using surface-optimized PSD parameters of 68 ns for the short gate and 480 ns for the long gate. (a) shows a bi-dimensional distribution of both PSD and Energy while (b) is its projection on the PSD axis.

the distribution with two Gaussian functions as shown in Subfigure 3.10(b). The absolute figure of merit value depends on the chosen minimum detection energy threshold. The PSD distribution of higher energy events produces more separated peaks, increasing the FoM value while also lowering the difference between different short/long combinations. To avoid this latter issue only events with a DAQ Energy > 7000 (∼100 keVee) are considered. This threshold -calculated using the full pulse length- produces FoM values from around 0.7 to 1.2. Their distribution following a clear peak allows the determination of a maximum, thus the best value for L to consider. Long gate values above 320 ns produce similar FoM figures within a margin of uncertainty. For this work, the reference short/long combination is taken as 68 ns/480 ns implying that the DAQ energy of each event in arbitrary units is defined as the signal integral inside a long gate that is 480 ns wide as shown in Figure 3.9.

Alternative PSD techniques

Using the same experimental data set, other PSD techniques were investigated such as "curve-fitting" and "pattern recognition" methods. The first technique (i.e. curve-fitting) aims to distinguish particle types by fitting the decay part of the pulses where the difference in shape is enhanced [73][74]. The fit model used is often a decay exponential where the fit parameter is the slope, but other models were also tested in this work such as fitting the whole pulse with a Landau-like distribution :

$$L(x) = \frac{\xi_0}{\pi c} \int_0^{+\infty} e^{-t} \cdot \cos\left(\left(\frac{x-\mu}{c}\right) \cdot t + \log\left(\frac{t}{c}\right) \cdot \frac{2t}{c}\right) dt \qquad (3.5.4)$$

where L(x) is the fit function, ξ_0 is a factor proportional to energy, μ is the peak location in the waveform, and c is the scale parameter used as PSD value. The reliance of this technique on minimization algorithms resulted in a substantially higher processing time of around factor 10 compared to the charge integration method, as previously reported by [75]. The resulting PSD distribution didn't show an improved separation compared to the charge integration method (see Table 3.2). This is because the difference in the pulse shape between different particles is mainly
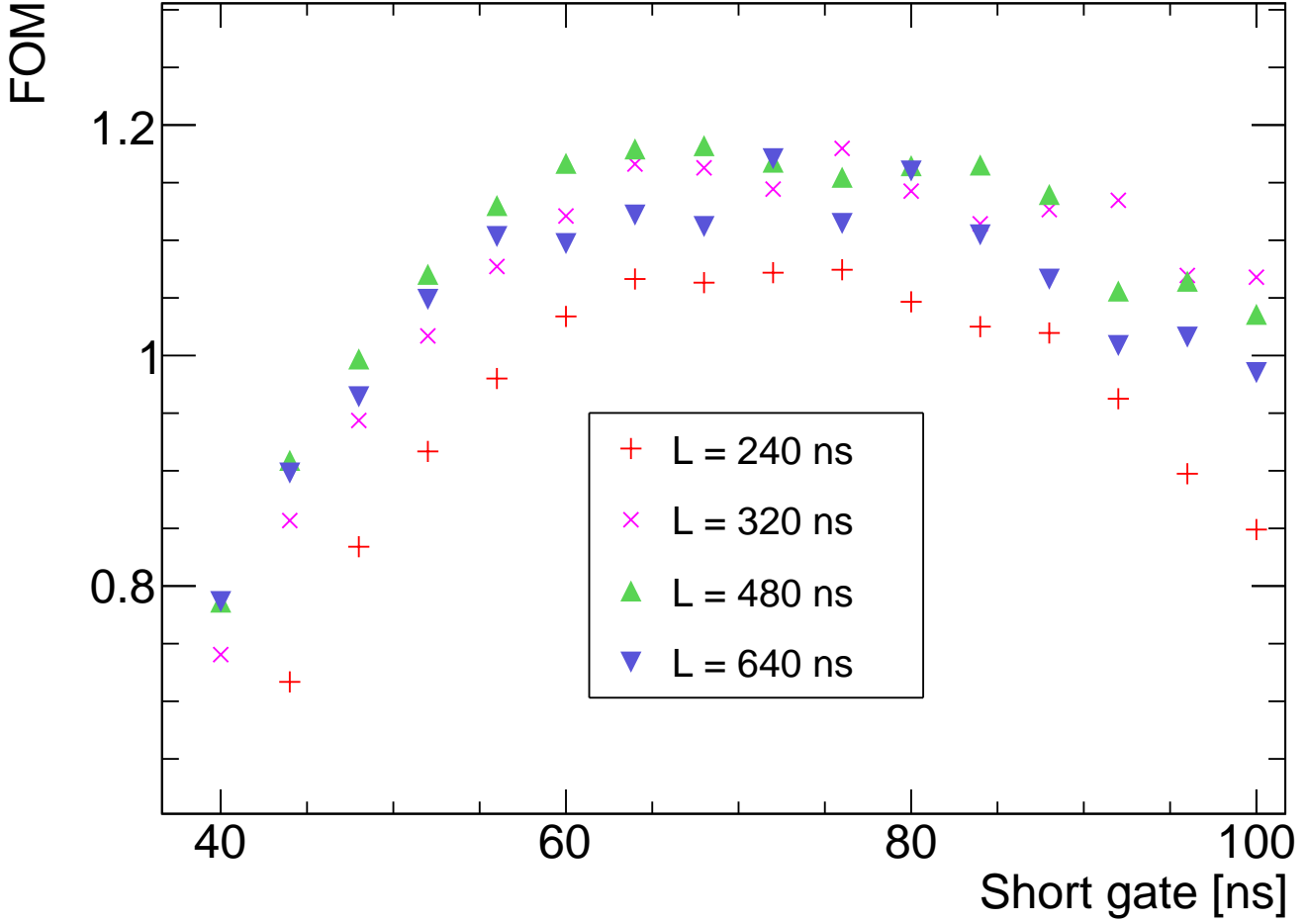
Figure 3.11: Figure of merit values estimated for different short/long gate values for AmBe source events above DAQ energy of 7000, corresponding to around 0.1 MeVee (see Section 3.6).

emphasized towards the end of the pulse (see Figure 3.8). This latter region of the signal is however not always well-fit by the algorithm because of several reasons such as its lower weight compared to the peak vicinity and also the overall non-strictly Landau-like shape of the pulse.

Another PSD technique investigated in this work is the pattern recognition method [76]. It considers the signal waveform as an n-dimensional vector with a coordinate value equal to the voltage value at each sample. The PSD parameter is here considered to be the angle formed by the vector V and a reference vector W from a typical γ/neutron pulse as follows :

$$\Theta = \arccos\left(\frac{V \cdot W}{|V| \ |W|}\right) \tag{3.5.5}$$

where $V \cdot W$ represents the scalar product of the waveform vector V and the reference vector W, while $|V|$ and $|W|$ are their respective norms and ϑ is the angle between the two, used as the discrimination parameter. It, therefore, decreases with the increasing similarity (particle type) between the V and W. Contrary to charge integration, curve-fitting, and pattern recognition methods do not require a polished

Table 3.2: Comparison between the performance of different PSD techniques using data from an AmBe source measurement. The first column represents the minimum energy considered for the PSD distribution. The electron-equivalent energy in the second column is calculated according to the calibration performed in Section 3.6

		FoM		
E_{DAQ} threshold	E_{ee} [keVee]	Double Gate	Pattern recognition	Curve-fitting
5000	70	0.87	N/A	N/A
7000	100	1.20	N/A	N/A
10000	137	1.31	0.81	1.11
20000	275	1.44	0.93	1.25

parameter optimization. It is enough to give a rough estimation of the slope value in the first one as a preliminary fit parameter while the pattern recognition does only require a smart choice of the reference vector. It is also noticed that the best separation results are obtained using the raw waveform sample values (i.e. without baseline deletion). A shape comparison between the results of these alternative methods and the reference one used in this work is shown in Figure 3.12 while the corresponding FoM values for different energy thresholds are reported in Table 3.2.

3.6 Energy calibration

The experimental data obtained measuring 158 kBq ^{60}Co and 22.5 kBq ^{137}Cs radioactive sources, is used to establish the EJ-309 liquid scintillators γ-energy calibration. Their typical γ-emissions at respectively 1.17, 1.33, and 0.66 MeV produce well-identifiable Compton peaks. The energy calibration is established by finding a linear correspondence between the location of the Compton edge in the spectrum and their actual electron equivalent energy. This latter quantity is calculated using the following formula :

$$E_{Compton} = E \cdot \left(1 - \frac{1}{1 + \frac{2E}{m_e c^2}} \right) \qquad (3.6.1)$$

where $E_{Compton}$ is the Compton edge position, E the γ-ray initial energy, m_e the electron mass, and c the speed of light. In the case of ^{60}Co, the Compton edges are located at respectively 0.94 and 1.06 MeV while that of ^{137}Cs is found at 0.47 MeV. Their positions in the uncalibrated spectra -labeled in DAQ energy- can be determined in different ways. In this work, instead of the standard method of fitting the region of interest (ROI) of the spectrum with 1 or 2 Gaussians for respectively ^{137}Cs or ^{60}Co, Monte-Carlo simulated spectra of the EJ-309 scintillators response to the sources activities is generated using the Geant4 C++ Toolkit v11.0 [77]. The used detector geometry and composition are thoroughly discussed in Section 4.5. The obtained spectra from the two simulations are fitted to the corresponding data using a linear relation. Since the simulation outputs a spectrum with an infinite resolution, the fit procedure also considers a Gaussian energy spread of the events with a standard deviation value that scales according to the square root of the energy rule as follows :

$$\sigma(E) = R \cdot \sigma_0 \cdot \sqrt{\frac{E}{E_0}} \qquad (3.6.2)$$
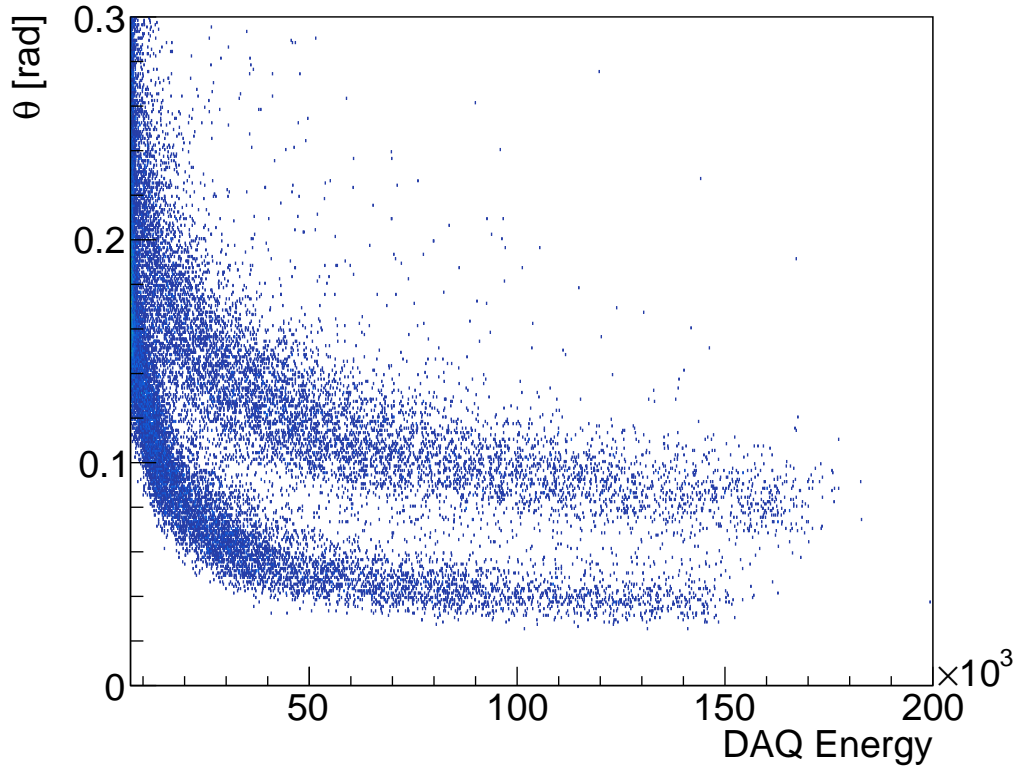
(a)
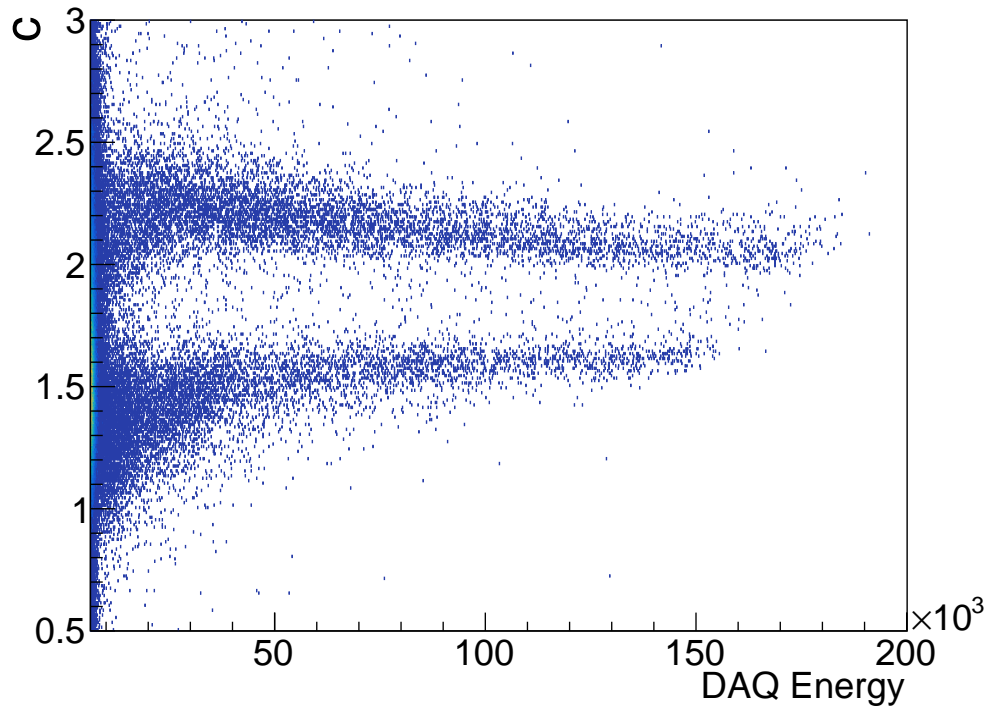
(b)

Figure 3.12: PSD performance using alternative PSD techniques.(a) is achieved using the pattern recognition technique focused on the t > 152 ns region of the waveform and using a high energy γ-signal vector as a reference (W).(b) is obtained using the curve-fitting method with the function from Equation 3.5.4. The border between γ and neutron events regions is located at around $\Theta = 0.05$ in (a) and at around c = 1.7 in (b), neutrons always being above and γ-rays below.

where $\sigma(E)$ is the energy resolution at energy E, R is the proportionality parameter, and σ_0 is the energy resolution at the reference energy E_0. The ratio is introduced to ensure that at $E = E_0$, $\sigma(E)$ is equal to σ_0. The value of this latter is deduced from the experimental spectrum and implemented in the numerical fit based on the minuit2 minimizer. Two different sets of calibration parameters are then obtained, each adapted for the ROI in the corresponding energy spectrum (i.e. ^{60}Co and ^{137}Cs) as shown in Figure 3.13. The values of this linear fit allow a more precise estimation of the Compton edge position in the uncalibrated spectra. Finally, a linear fit using the 3 obtained values is performed allowing the establishment of a calibration that is valid for a wider energy range (see Figure 3.14). For the rest of this work, this latter calibration is used as a reference for the establishment of energy in electron equivalent units except explicitly stated. This energy calibration applied to the Energy vs PSD bi-dimensional spectrum of the previously measured AmBe source is shown in Figure 3.15.
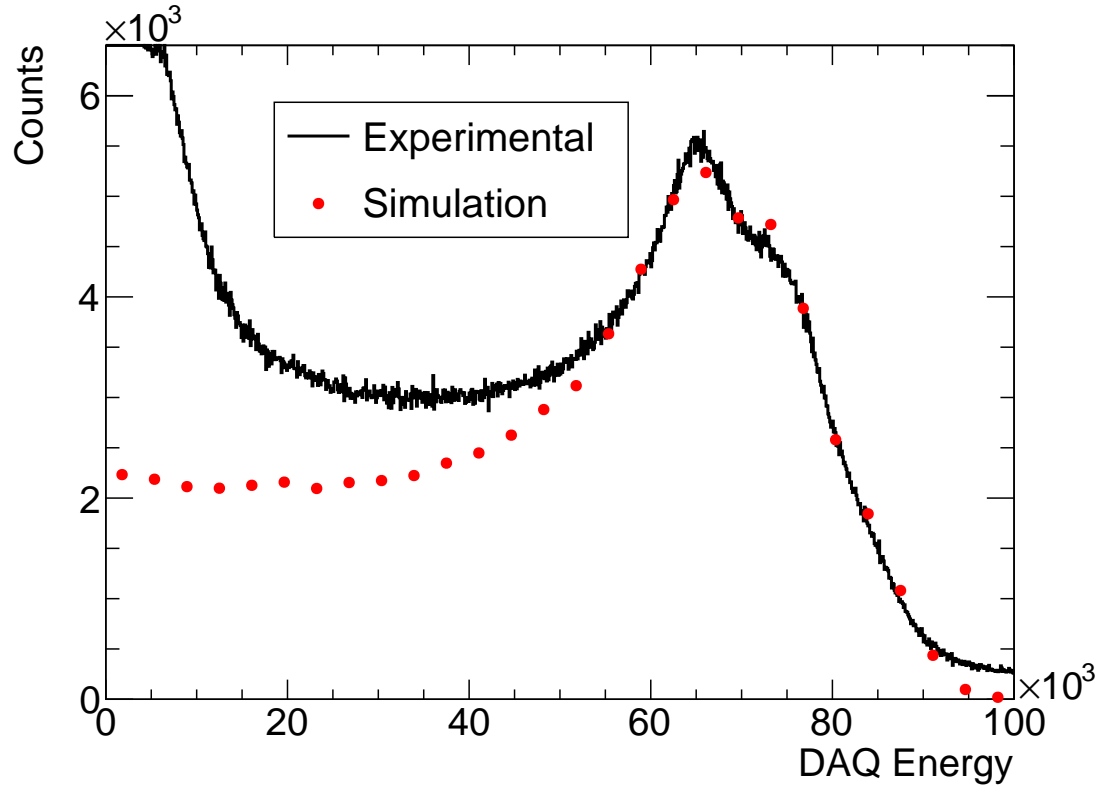
(a)
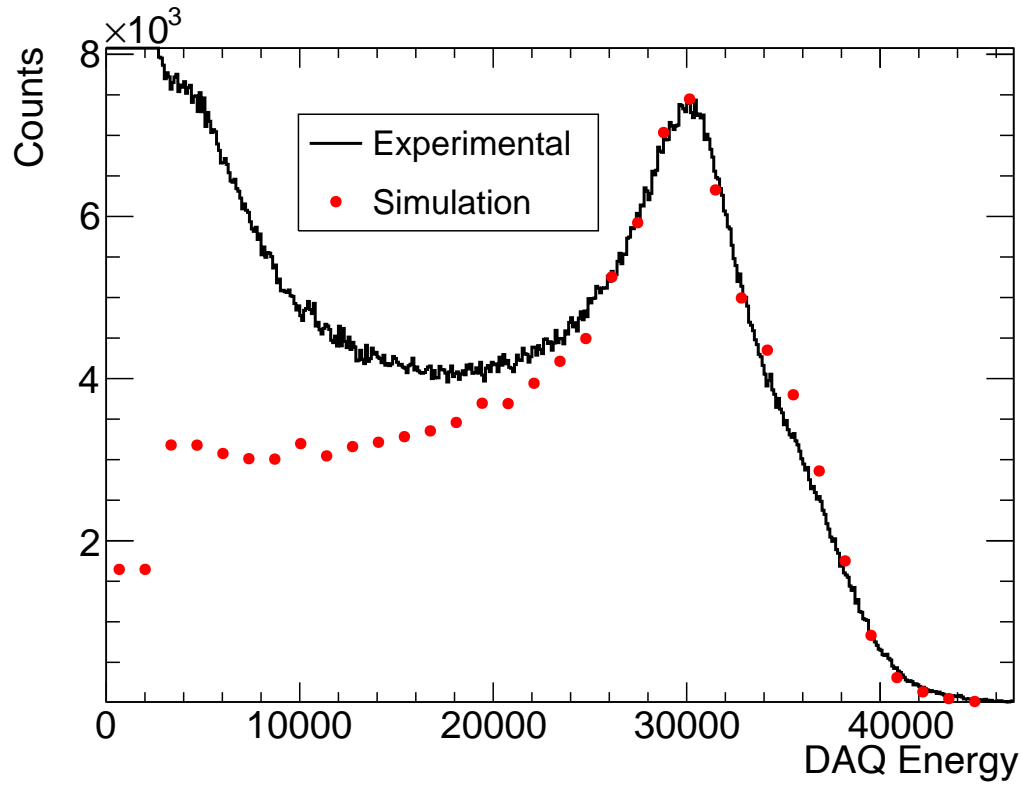
(b)

Figure 3.13: Fitted simulations of ^{60}Co in(a) and ^{137}Cs in (b) spectra to experimental data measured inside lead shielding in the surface lab.
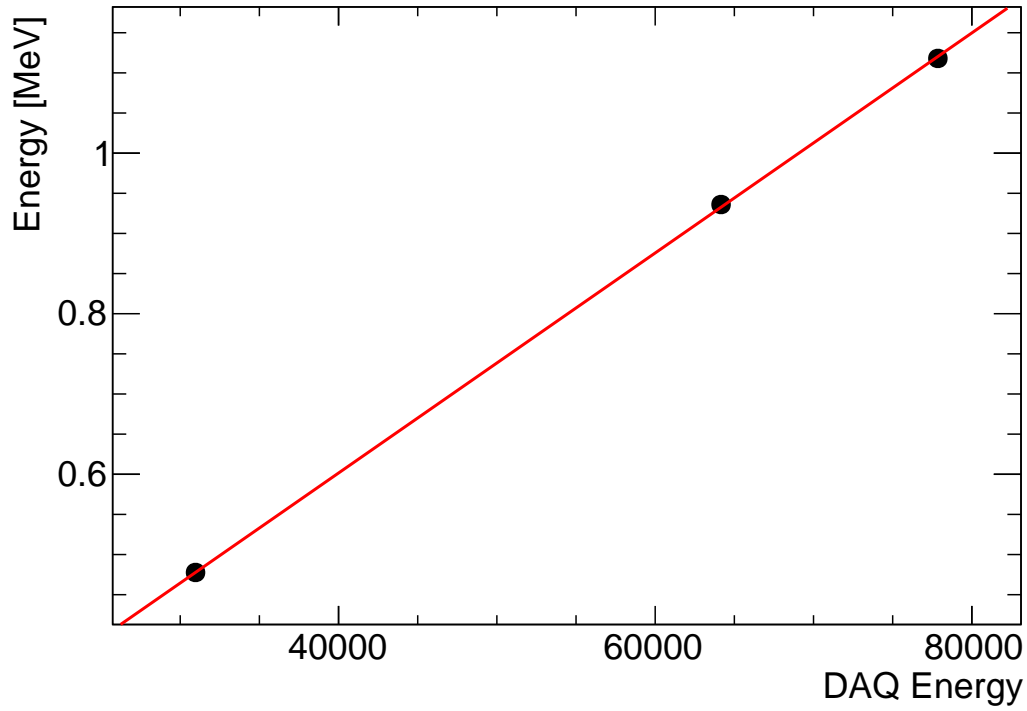
Figure 3.14: Energy correspondence between DAQ energy and the actual γ-energy. In red is a linear fit of the points with an output of $5.3{\times}10^{-2}$ for the constant and $1.37{\times}10^{-5}$ for the first order coefficient.
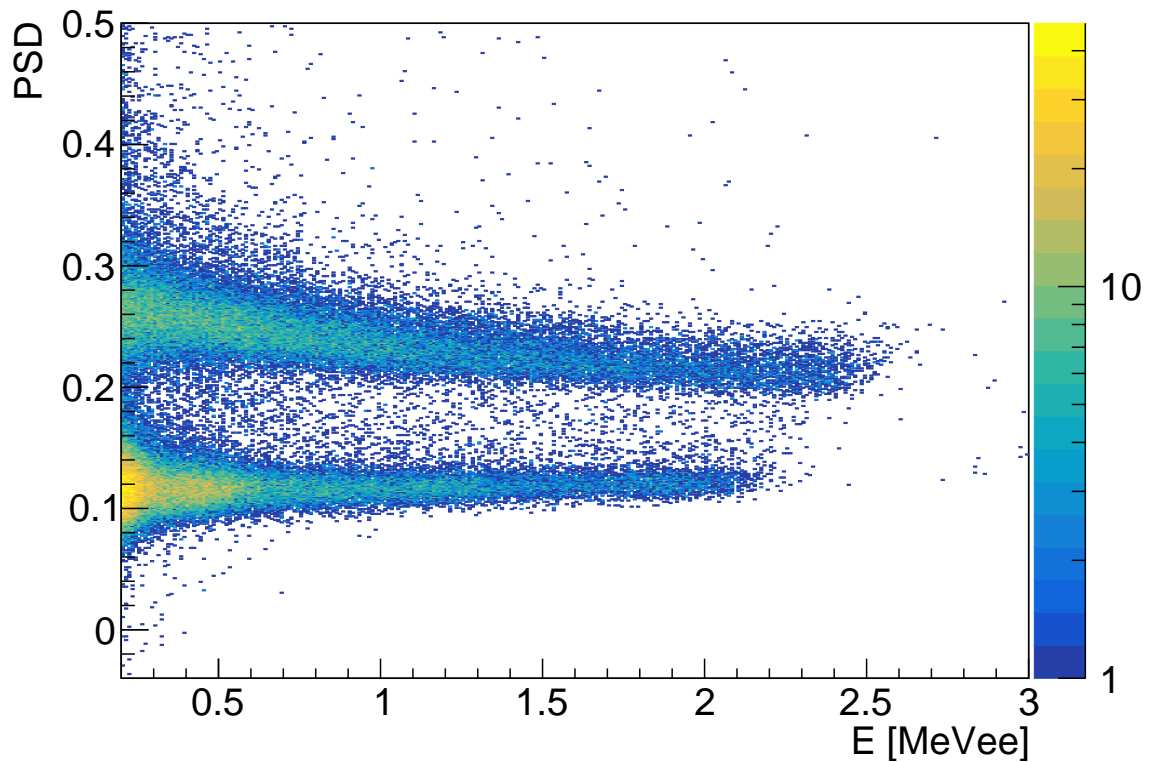
Figure 3.15: Calibrated PSD-energy spectrum of an AmBe source measured using an EJ-309 liquid scintillator placed inside lead shielding on a surface lab. The neutron activity region is located above PSD = 0.2 while the γ events region is below this limit.

Chapter 4

Intrinsic detector background

Deep-underground, neutron and γ environmental backgrounds are sufficiently low to increase the opportunities for improving the sensitivity for highly challenging nuclear cross section measurements. Under these conditions, the detector's own internal activity may become the new limiting factor thus the necessity to quantify it and possibly determine its origin and evolution over time. In this chapter, I describe the experimental setup and methodology I followed for the study of EJ-309 organic liquid scintillators' internal activity to be used in the measurement of the ^{22}Ne(α,n)^{25}Mg reaction, detailing the whole procedure from the establishment of proper γ and α energy calibrations to the identification of the radioactive contaminants present inside their structure. The data analysis tools and methods are also discussed at each corresponding step. Another PSD parameters optimization is also performed to optimize the particle-type separation for this new environment.

The required sensitivity for EJ-309 scintillator's intrinsic activity detection is reached by placing the set of 12 + 1 detectors in the LUNA-400 accelerator[79] room in the deep-underground facility of LNGS (see Figure 4.1). this latter is located 1.4 km under Mount Gran Sasso in the Italian Abruzzo region. Previous studies showed that neutron and cosmic ray fluxes measured inside this environment are respectively 3 and 6 orders of magnitude lower than on earth's surface [66][80]. The reduction of the neutron background (see Figure 2.5) is a considerable advantage that allows -as discussed in Section 4.3- a quantitative analysis of the internal activity leading to the determination of its origin. The same DAQ equipment described in Section 3.5 was transferred underground and used with the same acquisition parameters except for the record length that is reduced to 664 ns to save storage space. Detectors n° 1 to 12 were placed in a 4×3 rectangular arrangement inside a 5 cm thick lead castle covering all 6 sides (see Figure 4.2). This extra shielding helped to further suppress γ-rays and therefore reduce the events rate by up to 1 order of magnitude compared to the 13th detector placed nearby (outside of the lead castle) in a 5 cm thick borated-polyethylene shielding. The individual event rates are shown in Table 4.2. A different detection threshold is assigned to each detector leading to a background readout rate of around 200 kb/s. This allows the discarding of very weak signals that cannot be sorted by the PSD analysis, while also saving data storage space on the DAQ hard disk.
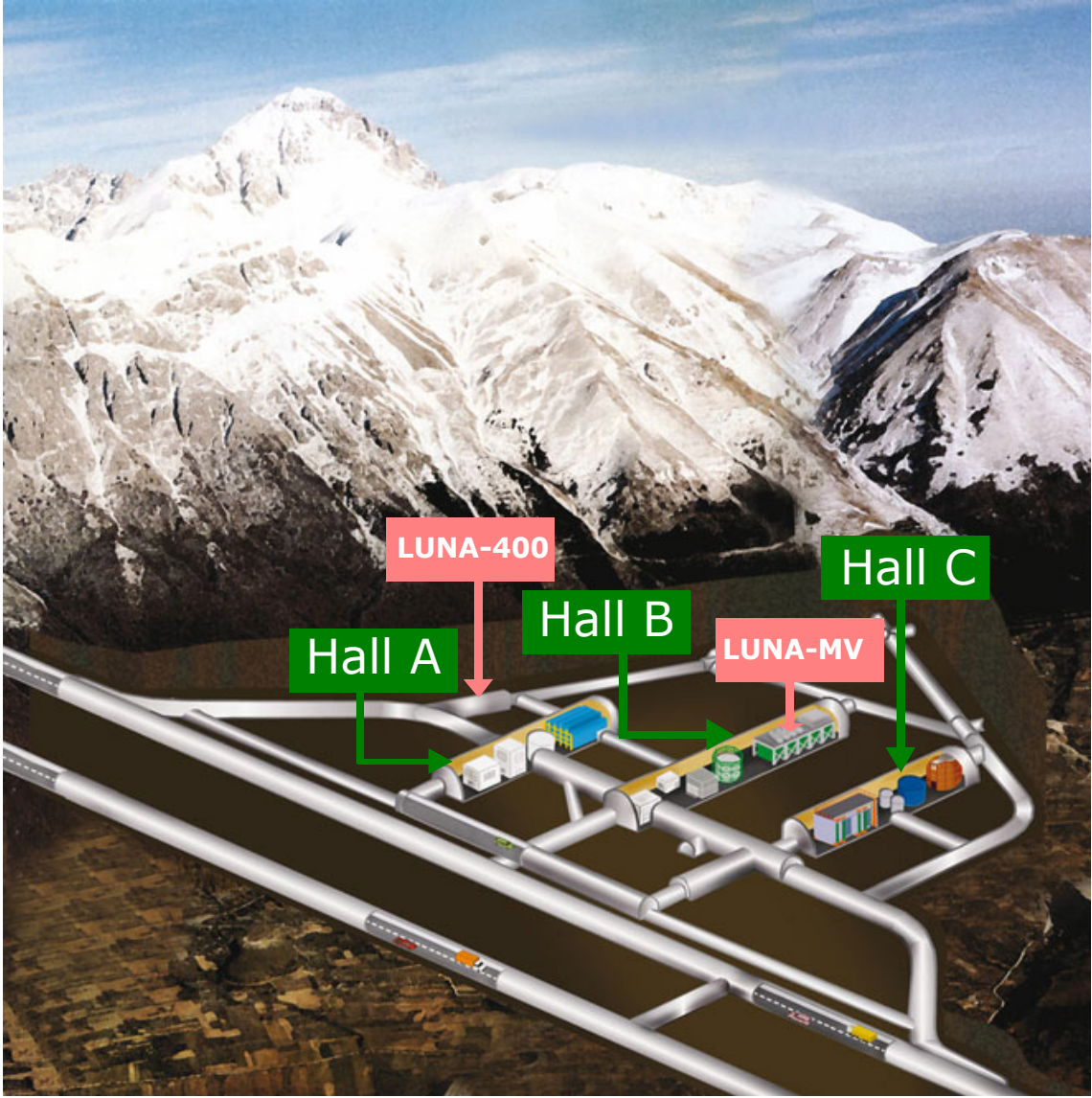
Figure 4.1: Plan view of the underground LNGS facility in Italy (AQ). Adapted from [78].

4.1 Underground measurements

γ-source measurement

A first short measurement is performed using a ^{60}Co source placed in between the already-shielded 12 detectors. The aim is to establish a new γ-energy calibration that is optimized for the new measurement conditions since environmental variables like temperature can influence the detector gain. The obtained energy spectra after the measurement are labeled in E_{DAQ} (channels). The conversion to γ (electron equivalent) energy is done through the Monte-Carlo simulation similar to the procedure previously discussed in Section 3.6. The Compton edge region located at around 850 to 1150 keV in the simulated spectrum is then fitted to the experimental spectrum assuming a linear relation. The fit result outputs two values: P_0 and P_1 which respectively are the y-intercept and the slope of equation 4.1.1.

$$E_{keVee} = P_0 + P_1 \times E_{DAQ}. \tag{4.1.1}$$

Despite the use of voltages from Table 3.1, the final experimental spectra of the

Figure 4.2: EJ-309 scintillators arrangement inside lead shielding in the LUNA-400 accelerator room at LNGS (Hall-A) during the internal background measurement.

two sources slightly differ from one detector to another. A Specific (P_0, P_1) pair of parameters, as reported in Table 4.1, is applied for the corresponding detector throughout the rest of this work.

Background measurement

To investigate the internal activity of the EJ-309 liquid scintillators, a long background run was performed between July 28th and September 1st, 2021 using All 12+1 detectors. The same DAQ settings as for the γ source measurement were used. Individual thresholds were readjusted to meet the targeted 200kb/s readout rate. The measurement lasted for around 839 hours. The raw number of events recorded by each detector -including the unshielded one- and the corresponding count rates are reported in Table 4.2. It is worth noting that low energy γ-events from the envi-
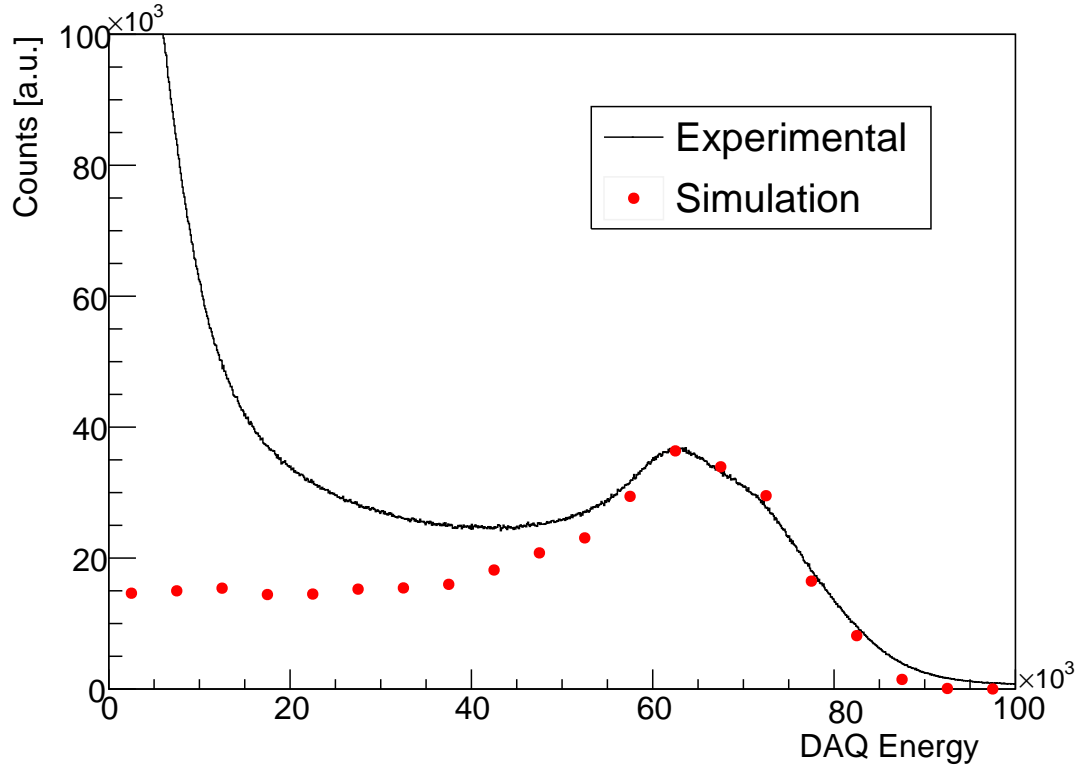
Figure 4.3: Simulated spectrum in the Compton edge region (in red) fitted to the Underground ^{60}Co experimental data (in black).

Table 4.1: Optimal E_{DAQ} to E_{keVee} calibration parameters for each detector

Detector	P_0	P_1
1	0.03	0.016
2	-0.01	0.015
3	-0.04	0.016
4	-0.07	0.015
5	-0.01	0.015
6	-0.07	0.015
7	0.03	0.015
8	-0.25	0.015
9	0.00	0.015
10	-55.00	0.014
11	0.08	0.016
12	-0.02	0.015

Table 4.2: Count rates of each SHADES liquid scintillator recorded underground. The total measurement time was 3,019,367 s ($\sim$1 month).

Detector n°	Total n°of events	Count rate [s^{-1}]
1	$8.06{\times}10^7$	$2.7{\times}10^1$
2	$6.36{\times}10^7$	$2.1{\times}10^1$
3	$1.01{\times}10^8$	$3.3{\times}10^1$
4	$9.72{\times}10^7$	$3.2{\times}10^1$
5	$1.08{\times}10^8$	$3.6{\times}10^1$
6	$8.90{\times}10^7$	$2.7{\times}10^1$
7	$8.86{\times}10^7$	$2.9{\times}10^1$
8	$7.53{\times}10^7$	$2.5{\times}10^1$
9	$1.06{\times}10^8$	$3.5{\times}10^1$
10	$1.35{\times}10^8$	$5.0{\times}10^1$
11	$9.26{\times}10^7$	$3.1{\times}10^1$
12	$1.21{\times}10^8$	$4.0{\times}10^1$
13 (Pol)	$6.97{\times}10^7$	$2.3{\times}10^2$

ronment constituted the main contributors to the total rates as can be seen in the background energy spectrum (Figure 4.4).

4.2 Underground data PSD analysis

Using charge integration short and long gates values optimized from the AmBe source lab characterization discussed in Section a bi-dimensional PSD-E diagram is created as shown in Subfigure 3.5). However, it is interesting to investigate whether it is possible to further improve the PSD peak separation at lower energies since the ^{22}Ne(α,n)^{25}Mg outputs very low-energy neutrons due to its negative Q-value. The figure of merit is therefore re-calculated for different short/long combinations, considering events with energy > 200 keVee. Below the latter deposited energy condition, particle type can not be described anymore by a Gaussian distribution, noticeably the γ-PSD peak. As a consequence, the numerical fit used to calculate the FoM value finds difficulties reproducing the peaks' shape, introducing inconsistencies in the results. Only data from 1 detector is here used to avoid worsening the peak resolution by summing data from different detectors with different calibration uncertainties. A further PSD analysis was performed investigating different short and long gate values of respectively 48 ns < S < 144 ns and 360 ns < L < 640 ns. The step is made finer around the FoM peak (see Figure 4.5). The results obtained performing this calculation are compiled in Figure 4.5. This analysis showed the best short/long combination to be (S = 80 ns, L = 480 ns). However all FoM values for a short gate 72 ns < S < 96 ns are within < 5% difference margin. The PSD performances obtained using two different sets of gate parameters: underground and AmBe source optimized, are compared in Figure 4.6.

The pulse shape discrimination analysis performed on the underground background measurement data revealed the existence of an activity peak at around 0.18 < PSD < 0.28, a region where usually neutron events are expected. It is expected from aforementioned ^{3}He counters measurements [48] [66]. The conclusion drawn at the time was that the neutron activity inside the LNGS underground facility is very low and therefore cannot quantitatively justify the number of observed
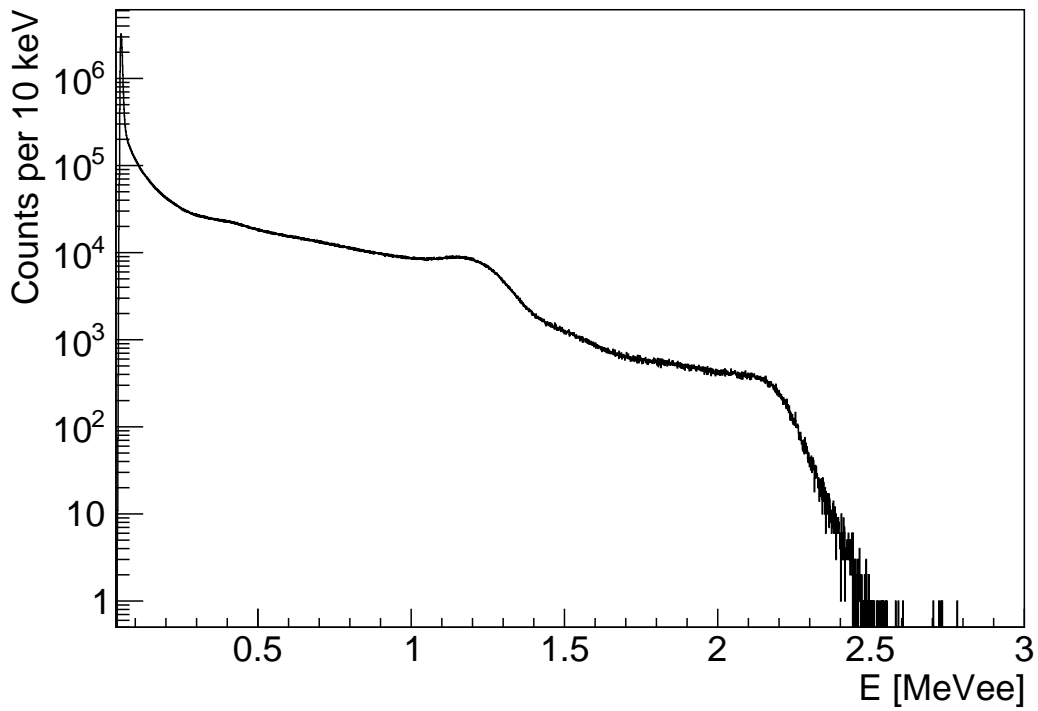
Figure 4.4: Underground background calibrated energy spectrum recorded by a single detector located inside the lead castle.
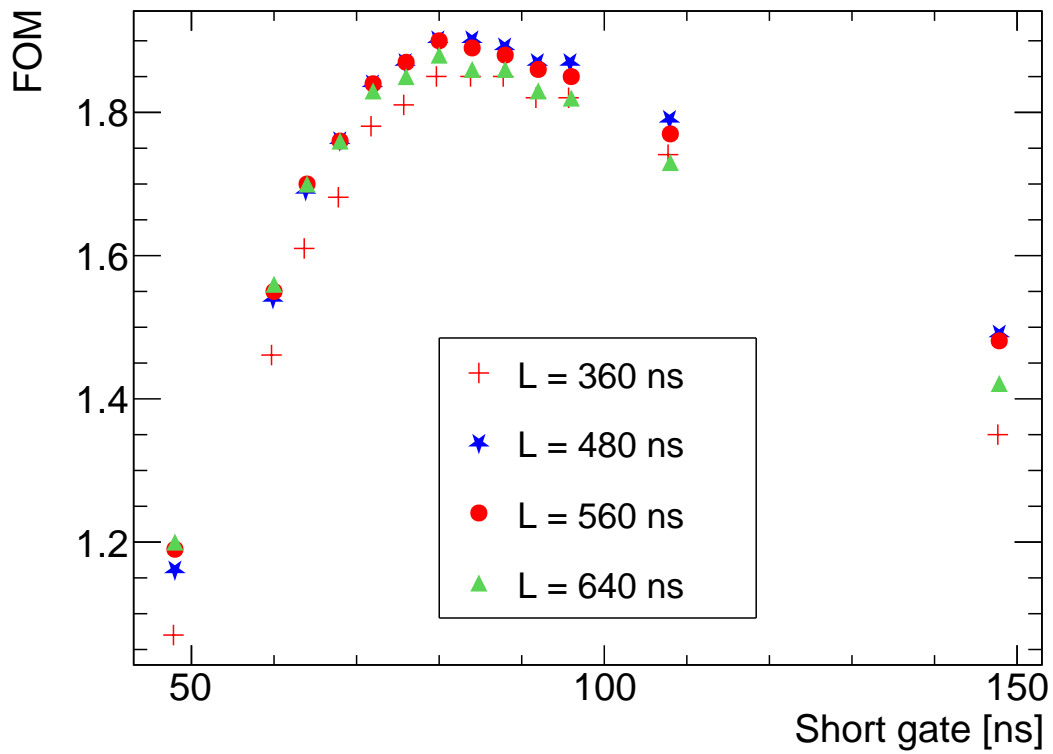
Figure 4.5: FoM dependency on short/long combinations for the charge integration PSD technique. Data from the LNGS deep-underground EJ-309 background measurement. Only events above 200 keVee are considered.
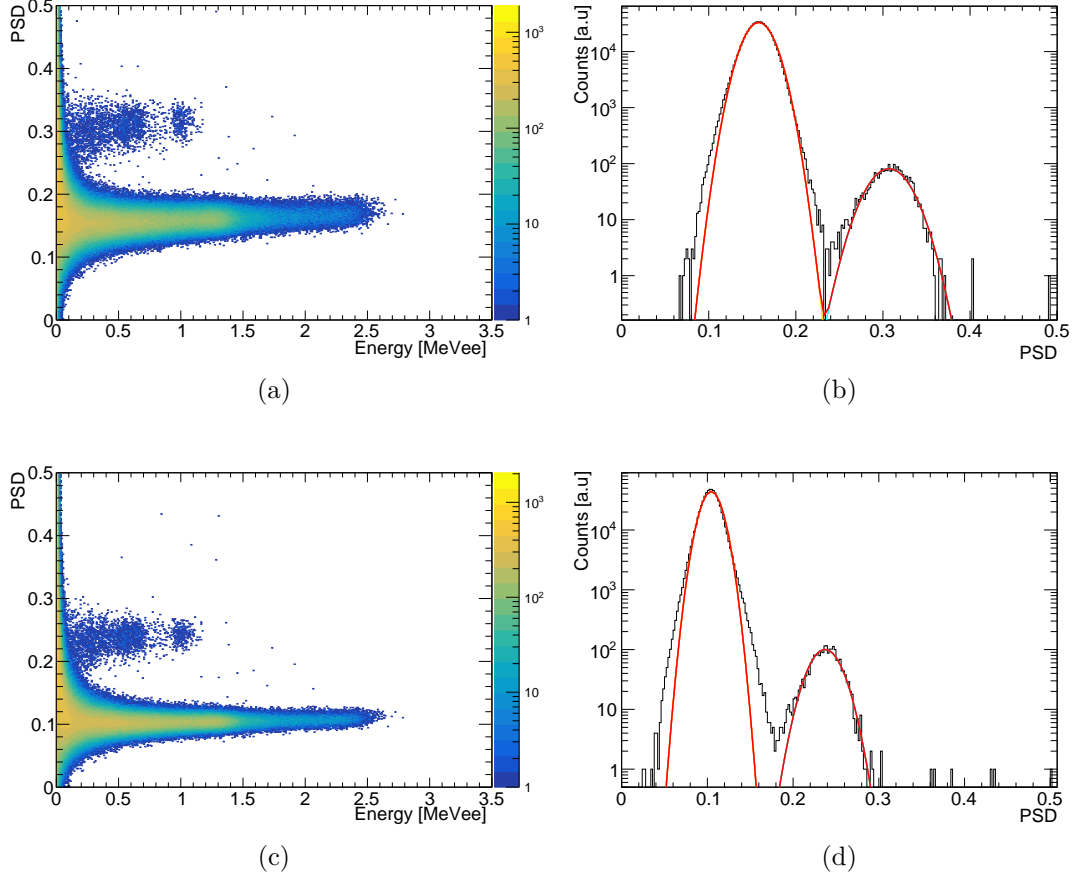
Figure 4.6: Underground measurement PSD analysis results comparison. (a) represents the PSD vs Energy distribution using the gates parameters optimized for a neutron source and (b) its projection on the PSD axis. (c) is the same bi-dimensional spectrum obtained for underground optimized gates and (d) is its PSD axis projection. The minimum energy threshold considered for the FoM building is 0.2 MeVee.

counts in this region, reported in Table 4.3. For comparison, N_n^{est}, the number of neutrons with an energy between 1 keV to 2.5 MeV (light output of 0.01 to 1.29 MeVee) that is expected to cross a scintillator (i.e. before taking into account a detection efficiency) for a $\sim 3 \times 10^6$ s measurement performed in the same facility [48] is only of :

$$
\begin{aligned}
N_n^{est} = \ & \Phi_n \times D_T \times S_{EJ309} \\
= \ & (\ (0.54 \pm 0.01) \times 10^{-6}\ )\ \text{cm}^{-2}\text{s}^{-1}\ \times\ 3,019,367\ \text{s}\ \times\ 760\ \text{cm}^2 \quad (4.2.1) \\
= \ & 1239 \pm 23\ \text{events.}
\end{aligned}
$$

where Φ_n is the measured neutron flux in the relevant energy range, D_T is the measurement duration and S_{EJ309} is the detector's external surface. It is, therefore, reasonable to attribute the observed high PSD peak activity to α-particles [81][49], most likely from within the detector itself (specifically its metallic part) due to their short average traveling range. α-particles are also known for having longer decaying signals in liquid scintillators compared to γ/β⁻ signals [82], thus increasing the PSD parameter value. The presence of isolated peaks in the projected energy spectrum of the corresponding PSD region (i.e 0.18 < PSD < 0.28) can be associated with activity originating from an α-emission chain having well-defined energies (see Subfigure

Table 4.3: Number of PSD-distinguishable α-events registered by each detector during the whole duration of the measurement (3,019,367 s).

Detector	α-counts	Error	α-activity (h^{-1})
1	$5.43{\times}10^4$	$2{\times}10^2$	64.7
2	$6.38{\times}10^4$	$3{\times}10^2$	76.1
3	$5.25{\times}10^4$	$2{\times}10^2$	62.6
4	$5.73{\times}10^4$	$2{\times}10^2$	68.4
5	$6.51{\times}10^4$	$3{\times}10^2$	77.7
6	$5.42{\times}10^4$	$2{\times}10^2$	64.7
7	$4.92{\times}10^4$	$2{\times}10^2$	58.7
8	$5.06{\times}10^4$	$2{\times}10^2$	60.3
9	$4.92{\times}10^4$	$2{\times}10^2$	58.6
10	$5.13{\times}10^4$	$2{\times}10^2$	61.1
11	$5.13{\times}10^4$	$2{\times}10^2$	61.1
12	$6.05{\times}10^4$	$2{\times}10^2$	72.1
13 (Pol)	$5.43{\times}10^4$	$2{\times}10^2$	64.7

4.7(b)). From there, it is possible to quantify the α-activity within each detector. This information is particularly important to consider since neutron events -relevant for the SHADES experiment- may be misidentified as that of α-particles because of their similar PSD signature (Figure 3.15). Nevertheless, since the separation becomes harder to achieve under 200 keVees (see Subfigure 4.6(a)), the first estimation of the observed α-counts number is obtained using a graphical cut manually defining the "distinguishable" α-particles border (see Figure 4.8). The results of this procedure repeated for all detectors are reported in Table 4.3. While saturated waveform events are here nonexistent, pile-up events inside the α-peak represent less than 1% of the total count of the α-peak, allowing to pass over any dead time contribution in the rest of underground data analysis.

4.3   Internal α-activity

The EJ309 scintillating liquid of the detectors is contained inside an aluminum housing with an intrinsic α-activity due to ^{238}U and ^{232}Th presence in the original ore [83]. The quantification of this contamination is of particular importance for deep underground experiments [49]. Due to the strong neutron suppression underground, this intrinsic background dominates the observed corresponding PSD region spectrum (see Subfigure 4.7(b)). When emitted inside the aluminum housing α-particles gradually lose their energy along the wall thickness before reaching the active detector volume. They are therefore expected to produce a continuous α-energy spectrum down to zero energy. However, the aforementioned spectrum shows 3 distinct peaks, which indicate the presence of αemitters inside the liquid itself, where the total energy of the particle is deposited. ^{222}Rn from ^{238}U and ^{220}Rn from ^{232}Th are the first gaseous elements to be produced in their respective chains (see Table 4.4). Assuming that they can diffuse through the detector walls before decaying inside the liquid ($t_{1/2}^{^{222}\mathrm{Rn}}$ = 3.8 days and $t_{1/2}^{^{220}\mathrm{Rn}}$ = 55 seconds), one expects to observe 4 α-particles from each chain, which for the used scintillators resolution (0.53 MeV at 7.69 MeV) would result in six peaks in the energy spectrum. The two lower energy α-emission peaks after radon creation in both decay chains are too close to be resolved. Sub-

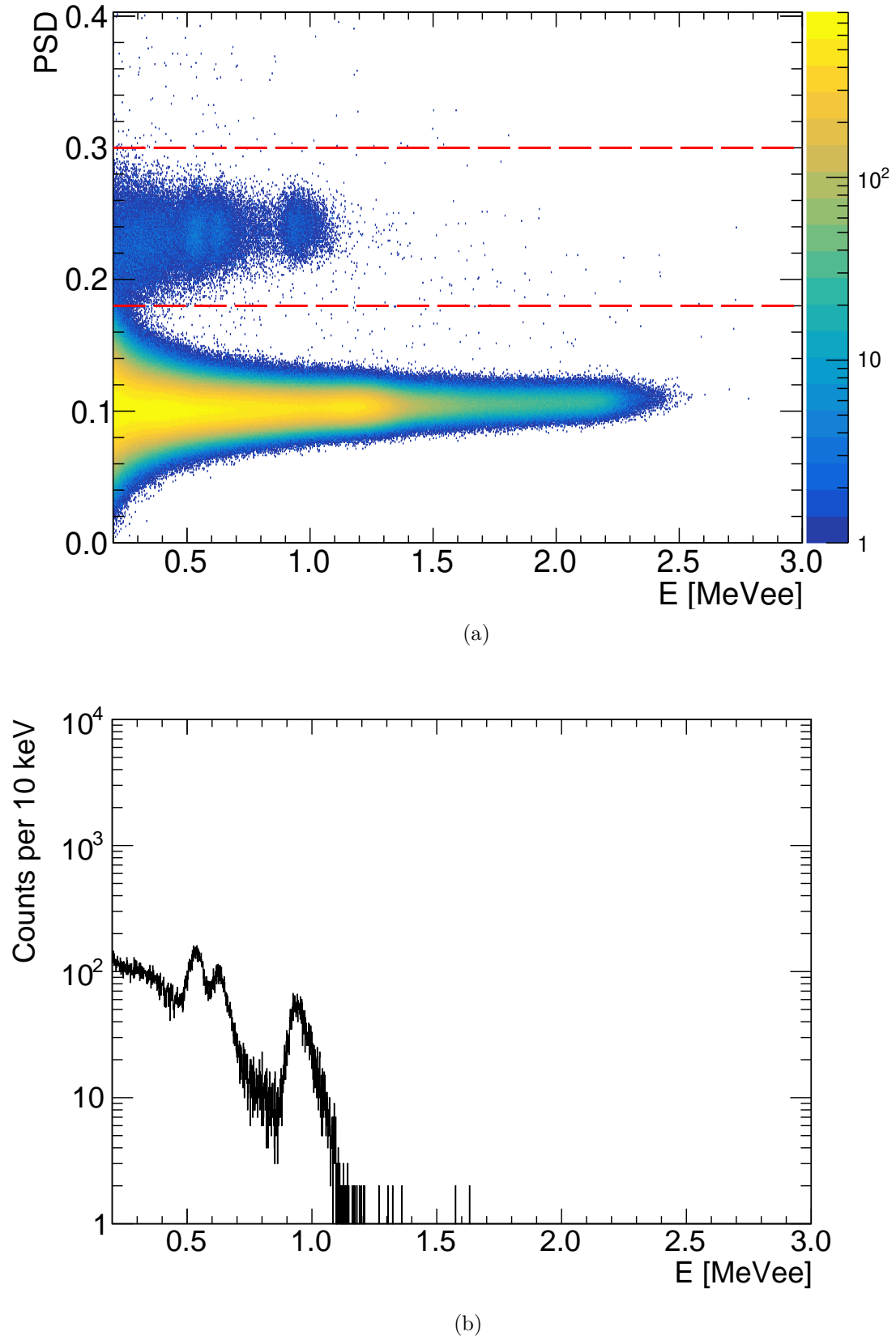(a)

(b)

Figure 4.7: The results of the underground measurement analysis is shown. (a) is the signature of different peaks in the $0.39 > \mathrm{PSD} > 0.24$ region is highlighted and (b) is the energy spectrum of this latter PSD region.
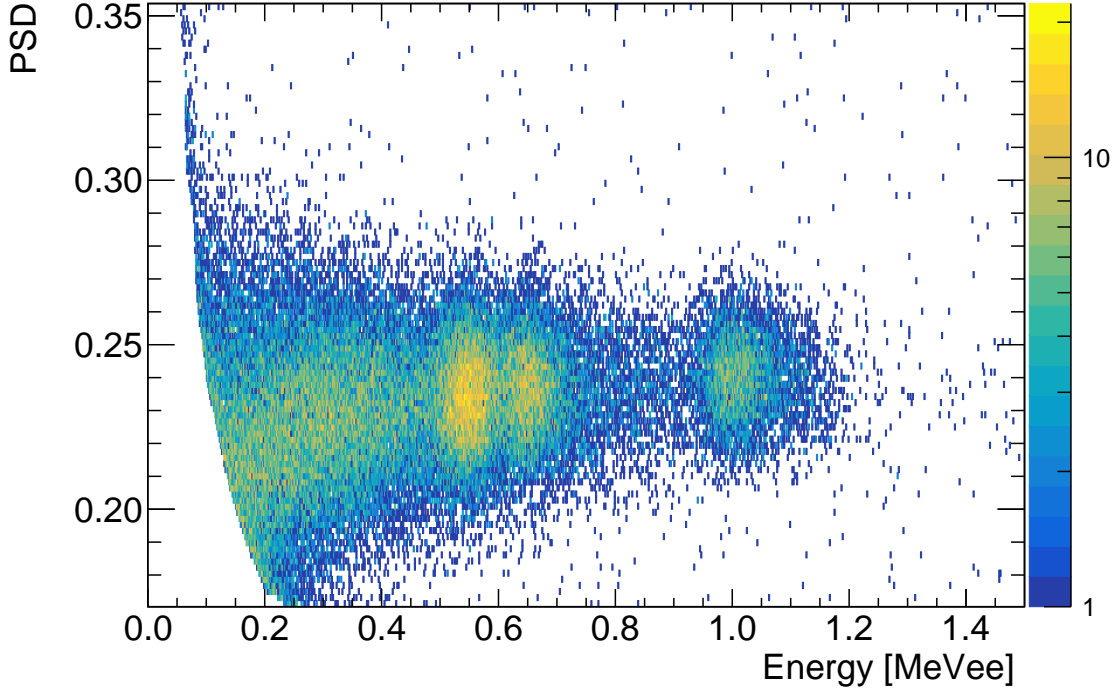
Figure 4.8: Isolated α-activity PSD peak of detector n°4 from Subfigure 4.7(a).

figure 4.7(b) clearly shows that only three peaks are observed. The activity of only one of the two radon isotopes is therefore detected.

The energy shown in Subfigure 4.7(b) is labeled in MeVee. It represents the light output of the detected α-events rather than their actual energy. It is therefore not possible to determine which of the two decay chains is responsible for the observed liquid activity peaks exclusively using this energy information, especially since both produce radon decay spectra of similar relative intensities. It is however possible to determine the responsible parent radon isotope by performing time coincidence analysis. The half-life of the isotope producing the highest α-energy peak is either 0.299 or 163 µs depending if it is ^{212}Po from ^{232}Th or ^{214}Po from ^{238}U, with respectively the following its decay schemes :

$$^{214}\text{Bi} \rightarrow e^- + {}^{214}\text{Po} \rightarrow {}^{210}\text{Pb} + \alpha \ (7.67\text{MeV})$$

$$^{212}\text{Bi} \rightarrow e^- + {}^{212}\text{Po} \rightarrow {}^{208}\text{Pb} + \alpha \ (8.78\text{MeV})$$
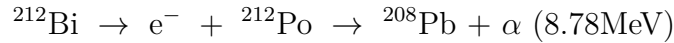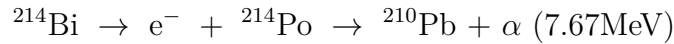
In both cases, the polonium isotope is produced at the same time as a β^- particle and soon decays producing an α-particle. The time delay values between the two emissions (i.e. β^- and α) are therefore similarly distributed to the isotope of interest half-life decay spectrum. The time coincidence analysis is performed by first selecting events within $\pm 2\sigma$ from the fitted center of the highest energy peak (see Subfigure 4.7(b)). The time delay Δt with the directly preceding β^- event is then calculated using the timestamp information provided by the DAQ. β^- events are selected from the γ region since both particles produce similarly shaped signals because of the scintillator detector functioning principle [65]. Also, only events with energy > 0.3 MeVee are kept to reduce the number of random coincidences[49]. The

Table 4.4: ^{238}U and ^{232}Th natural decay families. Columns reporting in order: the parent isotope, its half-live, branching ratio, and the corresponding α-emission energy.

Uranium family				Thorium Family			
Parent	**half-life**	**B$^{\mathbf{R}}$**	**α-energy [keV]**	**Parent**	**half-life**	**B$^{\mathbf{R}}$**	**α-energy [keV]**
^{238}U	4.468×10^9 y	79%	4198	^{232}Th	14.0×10^9 y	78.20%	4012
^{238}U	4.468×10^9 y	21%	4151	^{232}Th	14.0×10^9 y	21.70%	3947
^{234}U	2.455×10^5 y	71.38%	4774	^{228}Th	1.9125 y	73.40%	5423
^{234}U	2.455×10^5 y	28.42%	4722	^{228}Th	1.9125 y	26.00%	5340
^{230}Th	7.538×10^4 y	76.30%	4687	^{224}Ra	3.66 d	94.92%	5685
^{230}Th	7.538×10^4 y	23.40%	4620	^{224}Ra	3.66 d	5.06%	5448
^{226}Ra	1600 y	93.84%	4784	^{220}Rn	55.6 s	99.88%	6288
^{222}Rn	3.8222 d	99.92%	5489	^{216}Po	144.0 ms	99.99%	6778
^{218}Po	3.097 m	99.97%	6003	^{212}Bi	25.0 m	25.13%	6050
^{214}Po	163.6 μs	99.98%	7686	^{212}Bi	25.0 m	9.75%	6089
^{210}Po	138.376 d	100%	5304	^{212}Po	0.299 μs	64.06%	8784

resulting values distribution is plotted in a 1 μs bin width histogram and fitted using the exponential decay formula from Equation 4.3.1 :

$$\mathrm{P}(\Delta t) = e^{-\lambda\cdot\Delta t} \tag{4.3.1}$$

where P(Δt) represents the probability for the polonium nuclide to survive after a time interval Δt, and λ is the decay constant. This latter quantity allows the estimation of its half-life t$_{\frac{1}{2}}$ using Equation 4.3.2, as follows :

$$t_{\frac{1}{2}} = \frac{\ln(2)}{\lambda}. \tag{4.3.2}$$

The fit is here constrained to the region between 1 and 1000 μs. The used DAQ setting implies a 992 ns time resolution between two events from the same detector. No difference in the distribution of events below 1μs can therefore be measured. For this reason, the fit lower edge value is set at 1μs. The upper edge of the fit range extends to around 6 half-lives, which is sufficient to assess the distribution slope. The obtained half-life values for each scintillator are reported in Table 4.5. Calculating the weighted average of the t$_{\frac{1}{2}}$ values for the shielded detectors (n° 1 to 12) leads to a half-life value of 163.7±1.1 μs which is that of ^{214}Po. A result that is equal to that obtained performing the fit on a unique delay time spectrum constructed summing delay time data from all shielded detectors as shown in Figure 4.9. This result for ^{214}Po half-life is in agreement with previous experiments dedicated to measuring the isotope's decay time confirming the ^{238}U origin of the observed α-activity in SHADES EJ-309 liquid scintillators (see Table 4.6).
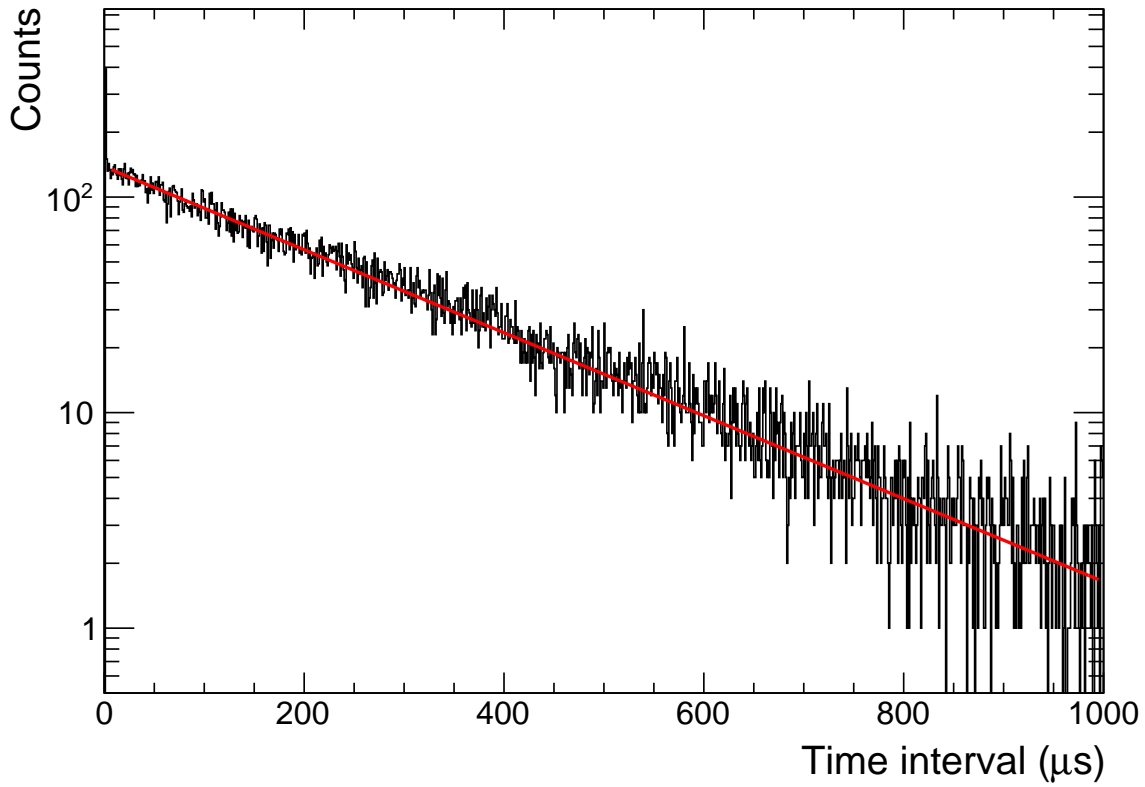
Figure 4.9: Spectrum representing β-α delay time distribution. Values taken from all lead shielded scintillators (i.e. units 1 to 12). The red line is the fit performed using Equation 4.3.1.

Table 4.5: ^{214}Po half-life estimation using each detector and its corresponding statistical uncertainty.

Detector	$t_{\frac{1}{2}}$ [µs]	Error [µs]
1	163.1	3.2
2	163.3	3.8
3	162.7	3.5
4	160.6	3.0
5	166.4	3.6
6	164.9	3.4
7	162.2	5.5
8	159.5	3.5
9	170.1	4.7
10	166.3	4.6
11	168.3	3.6
12	161.3	3.6
13 (Pol)	161.4	6.0

Table 4.6: ^{214}Po half-life values from literature and present work.

Ref.	$t_{1/2}$ [μs]
Von Dardel (1950) [84]	163.7 ± 0.2
Ballini (1953) [85]	158.0 ± 2.0
Ogilvie (1960) [86]	159.5 ± 3.0
Dobrowolski and Young (1961) [87]	164.3 ± 1.8
Erlik et al. (1971) [88]	165.5 ± 3.0
Zhou et al. (1993) [89]	160 ± 12
Wu (2009) [90]	164.3 ± 2.0
Suliman et al. (2012) [91]	164.2 ± 0.6
Miramonti et al. (2014) [92]	163.6 ± 0.3
This work [93]	**163.7 ± 1.1**

Table 4.7: Linear and quadratic α-energy calibration parameters. The light-output energy is taken in keVee and α-energy in MeV.

	p_0	p_1	p_2
Fit1	$-4.75(6) \times 10^2$	$1.85(1) \times 10^{-1}$	/
Fit2	0 (fixed)	$4.39(3) \times 10^{-2}$	$1.03(1) \times 10^{-5}$

4.4   α-energy calibration

Identifying the isotope responsible for the highest energy α-emission peak (i.e. ^{238}U) reveals the actual energy of each observed peak (see Subfigure 4.7(b)). This allows to establishment of an α-energy calibration, thus assessing the α-energy quenching behavior of the detectors (i.e. the non-linearity dependence of the light output production depending on the energy). A function built summing 4 Gaussian distributions + 1 decay exponential is used to fit the α-peaks in the region from 0.5 up to 1.1 MeVee. Each component respectively represents the α-activity contributions of ^{210}Po, ^{222}Rn, ^{218}Po, and ^{214}Po present in the liquid and that of α-particles emitted from the aluminum housing. The peak positions in the light output spectrum (see Subfigure 4.7(b)) are then extracted from the fit results as the corresponding Gaussian mean. This method allows the individual estimation of the ^{210}Po, ^{222}Rn α-emission peaks positions that are not resolved by the detector. A fit on the resulting 4 data points is then performed using both a linear and quadratic relation (see Figure 4.10). The obtained values of the parameters of both fits are reported in Table 4.7. At high α-energies the quenching behavior appears to become quasi-linear similar to previous observations done on similar types of organic liquid scintillators [94]. Besides ^{238}U, ^{232}Th is also usually found in commercially available aluminum [83]. It is worth noting that the PSD and time coincidence analyses discussed above do not fully allow the quantification of the contaminant amount that is contained in the aluminum housing. This is because α-peaks are only visible at higher energies. At lower energy values, a continuum dominates the α-spectrum requiring further analysis techniques to disentangle the contribution of different compartments. In the following section, this is achieved by fitting Monte-Carlo simulations of the different emitting chains (components) to the α-spectrum following a pre-defined radon diffusion scenario (see Section 4.5).
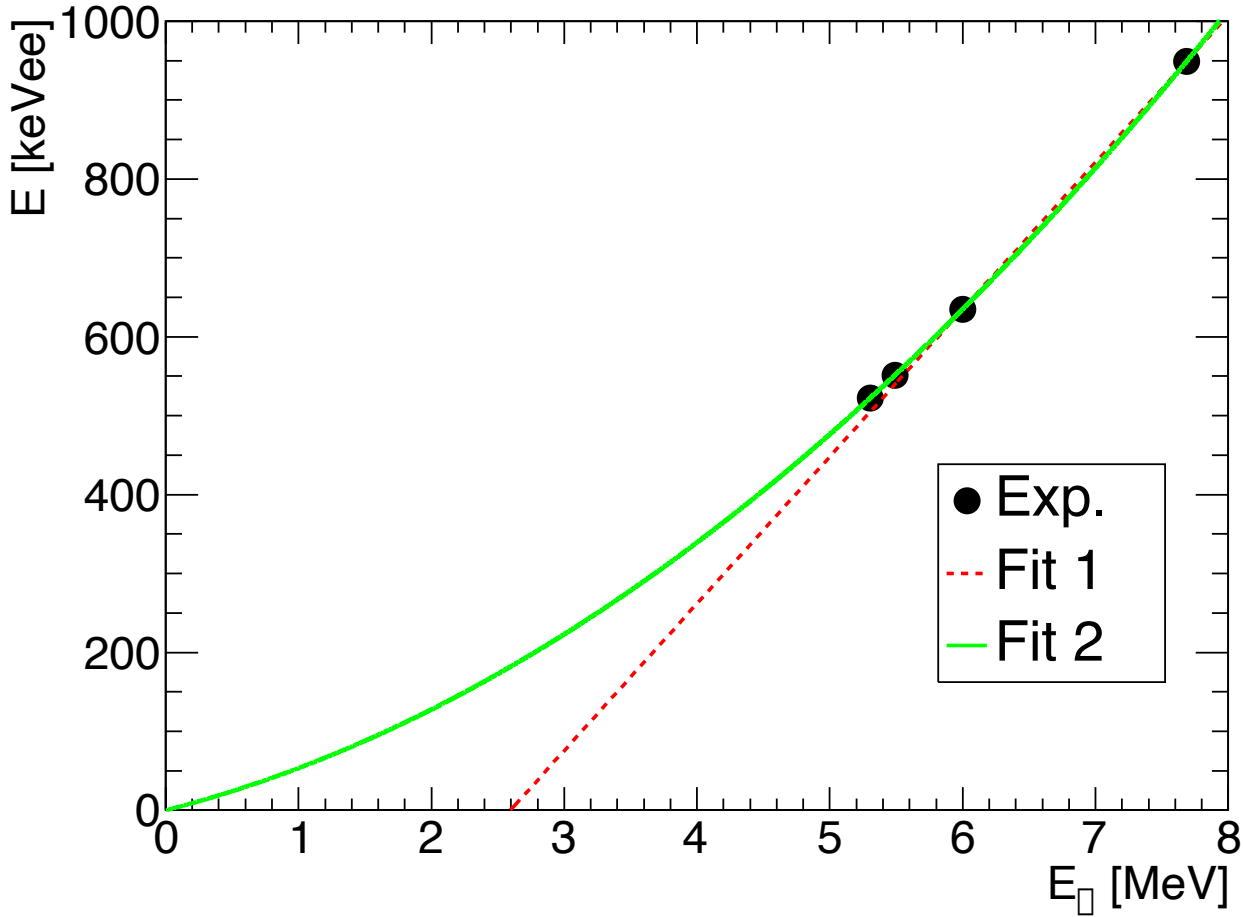
Figure 4.10: Electron equivalent energy vs. α-particle energy. The dots represent the locations of the α-peaks in Figure 4.7(b). Fit 1 (Dashed red line) is a linear fit. Fit 2 (green solid line) is a 2nd order polynomial function fit. Output fit parameters are reported in Table 4.7.

4.5   Contaminant concentration

The energy calibration for the α-energy experimental spectrum allows a direct comparison with a simulated model of the detector's internal α-activity. A set of Monte-Carlo simulations is built assuming a model where the diffusion of ^{222}Rn from the aluminum to the liquid is negligible. Most ^{238}U, ^{232}Th, and their decay products events are considered to occur within the aluminum vessel and only a small fraction ^{222}Rn can reach the liquid. Those latter do, nevertheless, completely dominate the α-spectrum shape at higher energies because of the much higher detection efficiency of decays occurring within the liquid. Also, ^{222}Rn has by definition a different concentration in the detector than ^{238}U. This is due to its shorter half-life compared to this latter while having the same decay rate A(t) because of secular equilibrium. The number of ^{222}Rn nuclei N(t) present in the detector at an instant t is much larger than that of ^{238}U since:

$$A_X(t) = \lambda_X \cdot N_X(t)$$

and (at secular equilibrium):

$$A_{238_U}(t) = A_{222_{Rn}}(t) \text{ with } \lambda_{238_U} < \lambda_{222_{Rn}}.$$

Implying that:

$$N_{238_U}(\Delta t) < N_{222_{Rn}}(t).$$

The contribution of ^{222}Rn and its daughters present in the liquid must also be taken into consideration when building a model that describes the observed α-activity. The shape of the peaks they produce guides the fit, allowing the disentangling of the individual contributions from other isotopes. The simulated α-activity spectra are generated using Geant4 as in Section 3.6. The simulated detector geometry is defined as a ⌀127mm, 127mm height cylinder of EJ-309, an organic liquid composed of 90.6 % carbon and 9.4% hydrogen with a density of 0.959 g·cm^{-3} at a temperature of 293°K. The liquid cell is surrounded by a 2 mm thick aluminum housing (see Figure 4.11) except for the top side where the PMT is placed. The EJ-309 liquid is here the energy-sensitive volume where the energy deposited by incoming α-particles is registered. Those later perform multiple scatterings before losing the totality of their energies. This total energy deposition in the liquid is reconstructed in the post-process analysis summing the energy losses during the different scatterings belonging to the same α-event. The distribution of the obtained values gives the α-emission spectrum later used to fit the experimental data.

Effective thickness

Depending on their initial energy, α-articles generally travel for a relatively short range in materials. This implies that those detected in the liquid originate from a limited sub-volume of the aluminum vessel rather than from the totality of it. To determine the thickness of this effective volume, multiple simulations of the ^{238}U chain decay are performed varying the maximum depth at which α-particles are emitted. The number of events to be generated, G^{Al}, is also scaled to keep considering a constant concentration of ^{238}U and its daughters in the material between the runs. This variable is first set as 1×10^6 events for a 0.01 mm effective volume thickness. The scaling factor applied to G_{Al} at each depth value is the ratio between the vessel volume at this thickness and the original one at d = 0.01 mm. This gives G_d^{Al}, the number of events to be generated for a d = x mm depth simulation as follows :

$$G_d^{Al} = 1 \times 10^6 \times \frac{V_d^{Al}}{V_{0.01}^{Al}} \tag{4.5.1}$$

The initial position from which each α particle is generated is random within the considered vessel thickness (i.e. from 0 to d mm). The momentum direction is also random and follows an isotropic angular distribution. The initial energy of each α-particle is randomly selected from the list of possible E_α values corresponding the each decay chain (see Table 4.4), with a probability $P(E_\alpha)$ defined as :

$$P(E_\alpha) = \frac{B^R(E_\alpha)}{\sum_i B_i^R} \tag{4.5.2}$$

where $P(E_\alpha)$ is the probability of selecting the energy E_α, $B^R(E_\alpha)$ the decay channel branching ratio -which is here equal to its intensity- corresponding E_α and $\sum_i B_i^R$ is
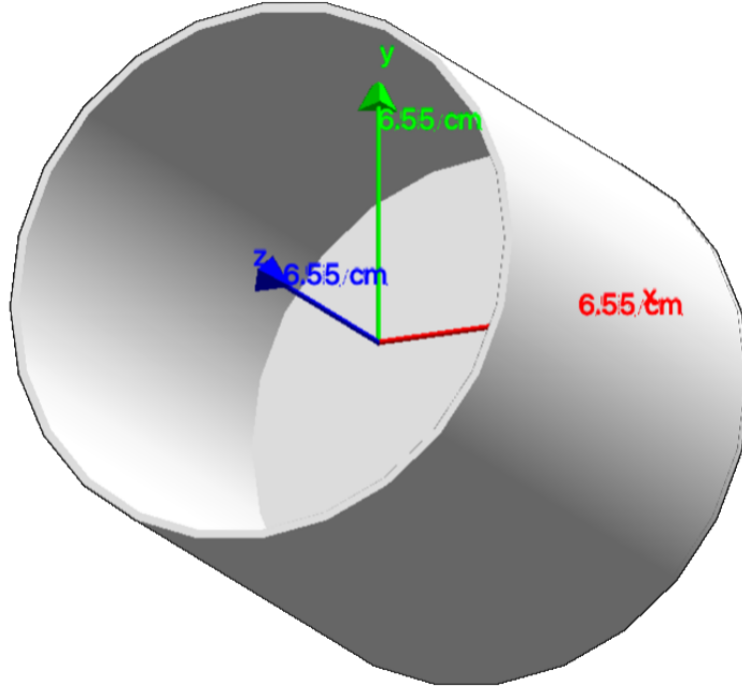
Figure 4.11: Geant4 simulated SHADES liquid scintillator vessel.

the sum of all intensities in the considered decay chain. Both ^{238}U and ^{232}Th decay chains in the vessel are considered in secular equilibrium. All isotopes are therefore assumed to have the same decay rate regardless of their decay time. Generating G_d^{Al} number of events at different vessel thickness values d for both ^{238}U and ^{232}Th, respectively resulted in an average travel range of 37 µm and 46 µm. The green lines in Figure 4.12 represent the aluminum vessel contribution to the detected α-activity depending on the considered thickness d. It is taken from the simulation as $S_d^{Al}(X)$, the number of detected α-particles originating from a d mm thick aluminum vessel layer, that reach the EJ-309 detection liquid. The plateau region reflects the fact that no extra α-particles can reach the liquid from above a certain thickness. Because of the statistical fluctuations of count values in the plateau regions due to the Monte-Carlo nature of the simulation, are considered as average α-chain travel range the depth values that achieve 99.7% of the maximum α-detection coverage (i.e. maximum number of α-particles reaching the liquid). For the rest of this work, the intermediate thickness of 0.08 mm is used instead of the 2 mm actual vessel thickness since all values from the plateau region are sufficient for this purpose (see green curve in Figure 4.12). Using the information from the same set of Monte-Carlo simulations, the aluminum vessel's α-detection efficiency of both chains X (with X = [^{238}U, ^{232}Th]) depending on the wall thickness d is calculated as follows:
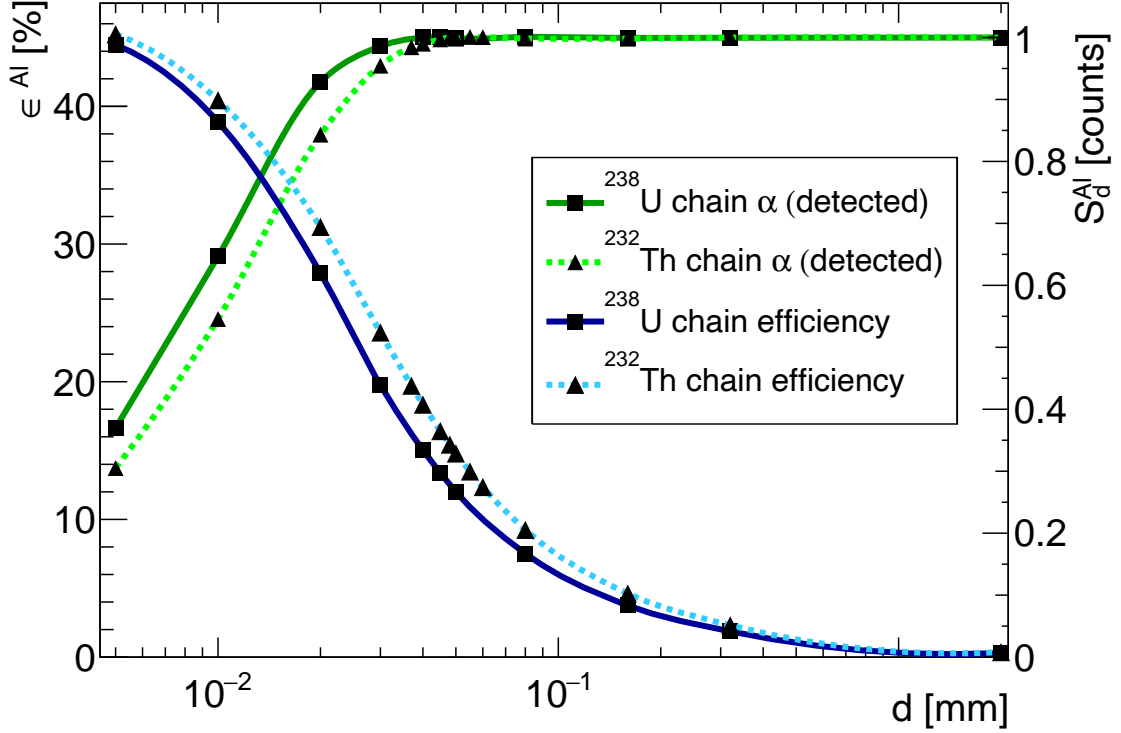
Figure 4.12: The blue curves represent $S_d^{Al}(X)$, the numbers of α-particles (normalized) from the natural decay chain X (X = [^{238}U, ^{232}Th]) reaching the detection liquid using different aluminum vessel thickness d (right Y-axis). The green curves represent the values of ϵ^{Al}, the detection efficiency of α-particles from the natural decay chain X depending on the vessel thickness d (left Y-axis).

$$\epsilon_d^{Al}(X) = \frac{S_d^{Al}(X)}{G_d^{Al}(X)} \tag{4.5.3}$$

The obtained values for $\epsilon_d^{Al}(X)$ values are plotted in the same Figure as for $S_d^{Al}(X)$ (see blue curve in Figure 4.12). Since α-alpha particles from ^{238}U and ^{232}Th decay chains are emitted isotropically, the detection efficiency cannot be > 50%. More often than not,

Emission spectra

Based on the information gathered above, the model reproducing the detectors observed internal α-activity to be fitted to the experimental data is built using the following 3 independent components :

- Component 1 : The ^{238}U to ^{210}Po chain decaying within the aluminum volume.

- Component 2 : The ^{222}Rn to ^{210}Po chain decaying in the detection liquid to produce the α-emission peaks observed in Subfigure 4.7(b).

- Component 3: The ^{232}Th to ^{212}Po decay chain in the aluminum to account for any possible thorium presence in the vessel.

Components 1 and 3 reproduce the ^{238}U and ^{232}Th chains α-emission within 0.08 mm vessel thickness. In contrast, component 2 handles ^{222}Rn atoms that diffuse in the whole volume of detection liquid before decaying into its later daughters. In all 3 components, secular equilibrium is always assumed. The introduction of an adequate detection resolution to the α-energy perfectly resolved simulated spectra is also mandatory before performing any fit on the experimental data. The resolution is obtained fitting the highest α-energy peak in the E_α calibrated spectrum using a decay exponential + Gaussian function. The standard deviation of the Gaussian component, noted σ_{exp}, is then extracted and used to smear all 3 simulations α-spectra following a Gaussian distribution. The energy resolution in liquid scintillators depends on the energy. A different value for σ_{exp} is hence applied at each different E_α following a square root scaling behavior as follows :

$$\sigma_{sim}(E_\alpha) = \sigma_{exp}(7.68 \text{ MeV}) \times \sqrt{\frac{E_\alpha}{7.68}} \tag{4.5.4}$$

where $\sigma_{sim}(E_\alpha)$ represents the local standard deviation value used redistribute the energy E_α events and $\sigma_{exp}(7.68 \text{ MeV})$ is the standard deviation obtained fitting the highest α-energy peak. Adding a resolution to the ^{238}U and ^{232}Th simulated spectra smoothed the sharp edges corresponding to the maximum α-energy emitted by each isotope (see Subfigures 4.13(a) and 4.13(c)). However, the same procedure applied to the ^{222}Rn simulation in the liquid resulted in a 3-peaks spectrum despite the corresponding activity coming from 4 different α-emitters. This is because α-particles from ^{222}Rn and ^{210}Po decays have close energies and cannot be resolved by the EJ-309 liquid scintillator. The two peaks therefore appear merged in the simulated spectrum, forming a single higher-intensity peak centered around an intermediate α-energy (see Subfigure 4.13(b)).

Model fit and uncertainties

The experimental α-energy spectrum to be fitted with the simulations is produced projecting the α-region peak from the 2−dimensional PSD figure into the x-axis as shown in Figure 4.7. The upper and lower limits of the selection PSD range are adapted for each detector to better constrain the α-peaks. Since the α-γseparation is less effective at low energies, the obtained spectra show a significant contribution from the γ-peak's tail. The fit range is therefore set to cover the region between 4.25 and 9 MeV, where a better separation is achieved. However, the ^{238}U and ^{232}Th chains being in secular equilibrium allows the estimation of the amount α-events down to 0 MeV. The fit model is constructed as a linear combination of the 3 α-emission spectra discussed in Subsection 4.5. The fit parameters represent the scaling factors to apply to each simulation to match the experimental spectrum as follows :

$$M(P_1, P_2, P_3) = P_1 \times S^{Al}_{^{238}U} + P_2 \times S^{Liq}_{^{222}Rn} + P_3 \times S^{Al}_{^{232}Th} \tag{4.5.5}$$

where $M(P_1, P_2, P_3)$ is the constructed model. S^{Al}_x the simulated α-emission spectrum of the x natural decay chain, $S^{Liq}_{^{222}Rn}$ is the simulated spectrum of ^{222}Rn family's α-activity in the EJ-309 liquid while P_1, P_2 and P_3 are scaling factors (fit parameters).
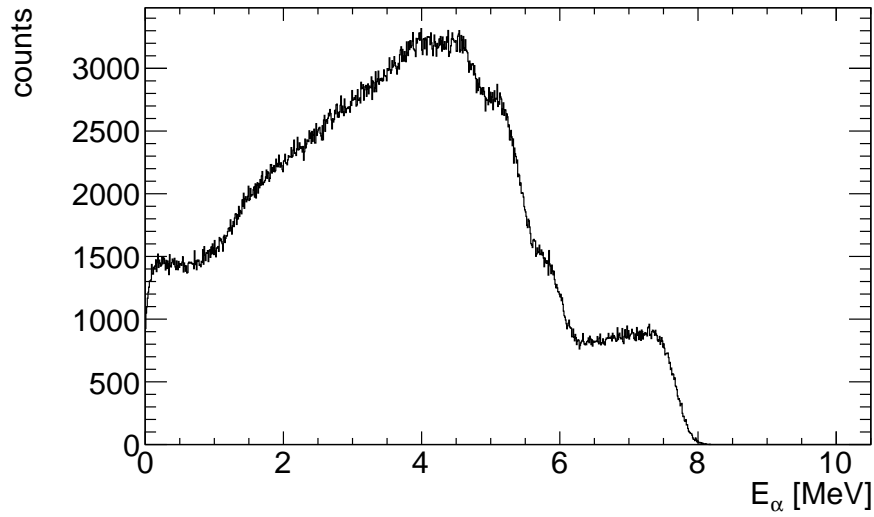
(a)
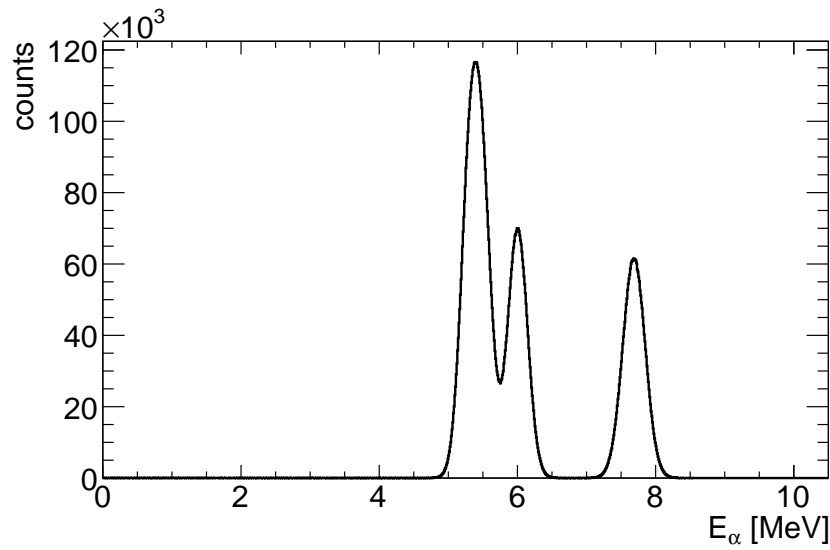
(b)
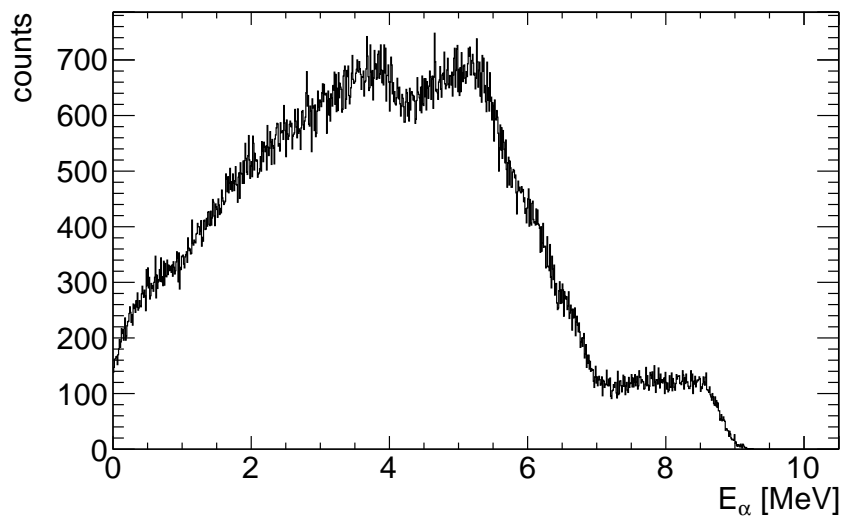
(c)

Figure 4.13: Simulated α-emission spectra in the scintillator using *Geant*4. (a) represents the ^{238}U chain decaying in aluminum housing, (b) the chain starting from^{222}Rn decaying within the EJ-309 liquid, and (c) the ^{232}Th chain decaying in the aluminum housing.
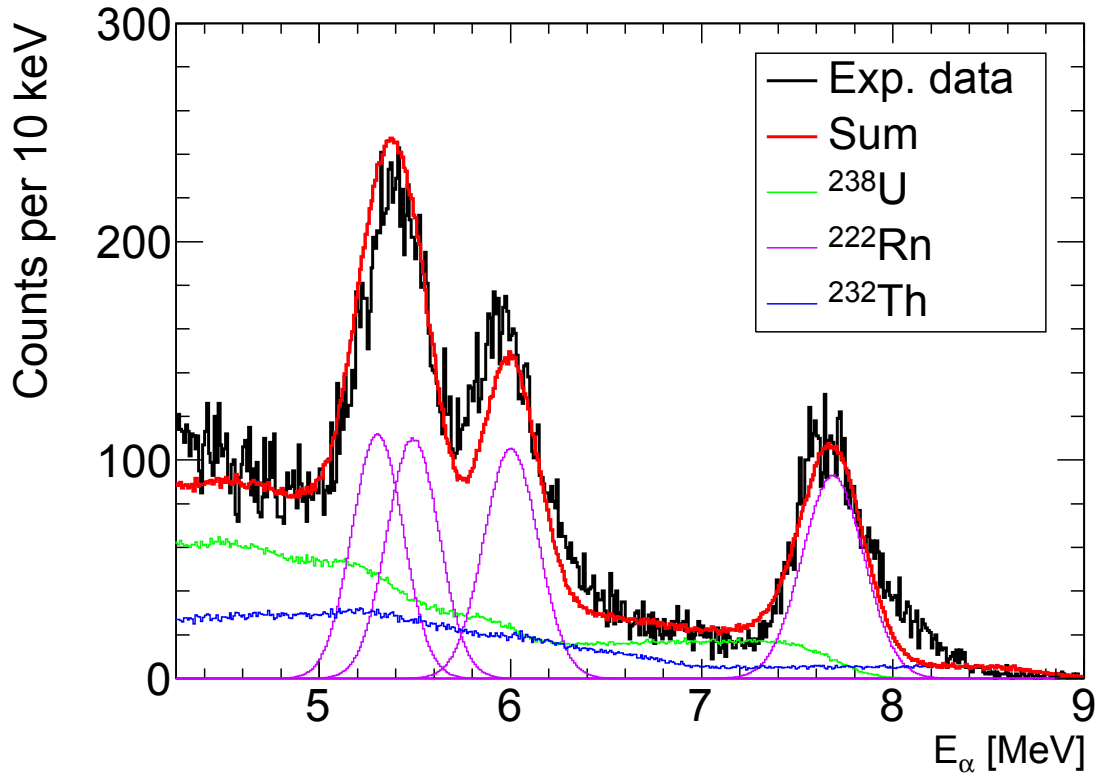
Figure 4.14: Simulated scintillator internal α-emission model $M(P_1, P_2, P_3)$ fitted to experimental α-spectrum (red). The ^{238}U and ^{232}Th decays occurs in the aluminum vessel while that of ^{222}Rn occurs within the EJ-309 liquid.

The model fit to the experimental spectra is performed using ROOT's numerical fitter *Minuit*2, configured to use the log-likelihood method. The results obtained for the full model as well as its components after performing the fit on the experimental data are shown in Figure 4.14. The fit procedure produced the best values for P_1, P_2, and P_3 as well as δP_1, δP_2 and δP_3, their corresponding errors. To estimate the total uncertainty to apply to the model, the distribution residual values are estimated using a normalization over the experimental data as follows :

$$r_i = \frac{M_i - X_i}{X_i} \tag{4.5.6}$$

where r_i, M_i, and X_i are respectively the values of the normalized residual, the fitted model, and the experimental data at bin i. The obtained residuals distribution shows a Gaussian shape centered around the value 0. Its standard deviation noted σ_{r_i}, is obtained through a numerical fit and represents the relative uncertainty of the model $M(P_1, P_2, P_3)$ (see Figure 4.15). This new fit has its own uncertainty $\delta\sigma_{r_i}$ that is here summed to that of σ_{r_i} to avoid underestimating $\frac{\delta M}{M}$, the relative uncertainty of the model, that is calculated as follows :

$$\frac{\delta M}{M} = \sigma_{r_i} + \delta\sigma_{r_i} \tag{4.5.7}$$

The $\frac{\delta M}{M}$ values obtained at the end of this procedure oscillate between 23 and 30% depending on the detector as can be seen in Table 4.8. The Systematic uncertainty of the model is estimated by performing the model to simulation fit considering two
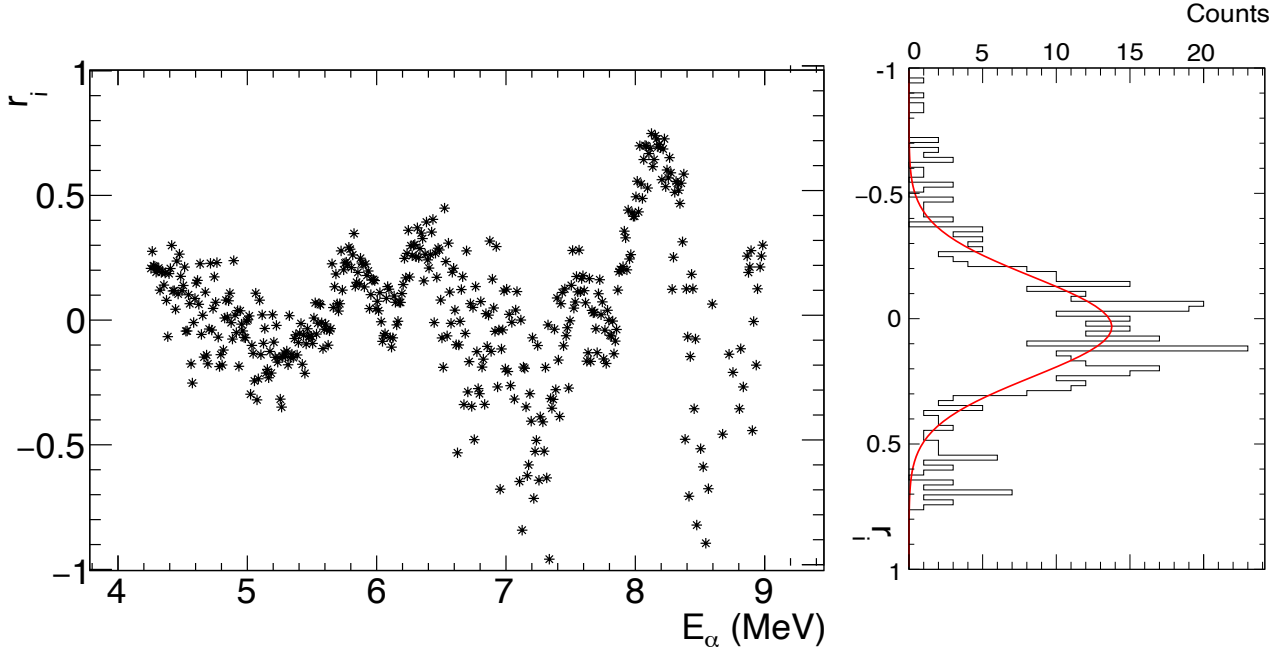
Figure 4.15: Normalized model fit residuals r_i scatter (left) and its corresponding distribution spectrum (right). The standard deviation of the fitted Gaussian (in red) is considered as the model uncertainty.

other energy lower limit α-energies: $E_\alpha = 3.50$ and 5.00 MeV. The first represents the starting of the γ-free region, while the second is the lower energy at which the α-peaks are fully separated. Value of 16% systematic uncertainty for ^{238}U and 2% for ^{232}Th are found.

Detection efficiency for α-particles

The estimation of ^{238}U and ^{232}Th concentration in the aluminum requires information about the detection efficiencies of their corresponding combined decay chains. A task that is possible to achieve using the already generated Monte-Carlo simulations. This full α-chain detection efficiency noted ϵ_X^{Al} for $(X = [^{238}U, ^{232}Th])$, is defined as the ratio between $S_d^{Al}(X)$, the number of detected α-events inside the liquid over $G_{0.08}^{Al}$, the number of the corresponding chain's emitted α-particles within the first 0.08 mm thick layer of the aluminum vessel. $S_d^{Al}(X)$ does only take into account α-particles that deposited energy in the liquid. Those crossing the cell's geometry in the simulation without interacting are considered undetected. The obtained detection efficiencies of the natural decay chains in the EJ-309 liquid scintillator are:

$$\epsilon_{238U}^{Al} = \frac{S_{0.08}^{Al}(^{238}U)}{G_{0.08}^{Al}} = 7.52\% \qquad (4.5.8)$$

Table 4.8: Model uncertainty estimated for each detector using residuals analysis

Detector	σ_{r_i}	Error	$\delta M/M$
1	0.21	0.02	0.23
2	0.28	0.02	0.31
3	0.23	0.01	0.25
4	0.24	0.02	0.25
5	0.30	0.02	0.33
6	0.25	0.02	0.28
7	0.23	0.03	0.26
8	0.25	0.02	0.27
9	0.25	0.02	0.27
10	0.28	0.02	0.30
11	0.23	0.02	0.25
12	0.25	0.02	0.27
13 (Pol)	0.28	0.02	0.30

$$\epsilon_{^{232}\text{Th}}^{\text{Al}} = \frac{S_{0.08}^{\text{Al}}(^{232}\text{Th})}{G_{0.08}^{\text{Al}}} = 9.21\% \tag{4.5.9}$$

α-particles produced in the EJ-309 liquid transfer all their energy in the detection medium. Their limited travel range makes it very unlikely to exit the cell's geometry and the very low concentration of their emitters makes it unlikely to be generated on the external surface. For this reason the number of generated G^{Liq}, and $S_d^{\text{Liq}}(^{222}\text{Rn})$ S^Liq_d(^{222}Rn) the number of α-events in the simulation are equal, thus giving a 100% efficiency as shown in Equation 4.5.10.

$$\epsilon_{^{222}\text{Rn}}^{\text{Liq}} = \frac{S_d^{\text{Liq}}(^{222}\text{Rn})}{G^{\text{Liq}}} = 100\% \tag{4.5.10}$$

The amounts of α-events originating from each decay chain inside the aluminum vessel noted $N_{^{238}\text{U}}^{\text{Al}}$ and $N_{^{232}\text{Th}}^{\text{Al}}$, is deduced from the simulations fit using Equation 4.5.5. They are the total sum of the corresponding simulated component after re-scale as follows :

$$N_{^{238}\text{U}}^{\text{Al}} = S_{^{238}\text{U}}^{\text{Al}} \times P_1 \tag{4.5.11}$$

$$N_{^{232}\text{Th}}^{\text{Al}} = S_{^{232}\text{Th}}^{\text{Al}} \times P_3 \tag{4.5.12}$$

While the uncertainty over them, respectively noted $\delta N_{^{238}\text{U}}^{\text{Al}}$ and $\delta N_{^{232}\text{Th}}^{\text{Al}}$, is assumed to be the same as $\delta M/M$, the relative uncertainty of the model. It is therefore calculated as :

$$\delta N_{^{238}\text{U}}^{\text{Al}} = N_{^{238}\text{U}}^{\text{Al}} \times \frac{\delta M}{M} \tag{4.5.13}$$

$$\delta N_{^{232}\text{Th}}^{\text{Al}} = N_{^{232}\text{Th}}^{\text{Al}} \times \frac{\delta M}{M} \tag{4.5.14}$$

The obtained estimated numbers for the α-decays that occurred in each detector are reported in Table 4.9. Since $S_{^{238}\text{U}}^{\text{Al}}$ and $S_{^{232}\text{Th}}^{\text{Al}}$ have similar overall shapes, it is

Table 4.9: Total number of α-decays and their corresponding statistical uncertainties inside each detector walls during the $\sim 3 \times 10^6$ s long measurement. The contributions of both ^{238}U and ^{232}Th chains are disentangled fitting the simulated model to the experimental spectra. The included uncertainty is estimated using residual analysis.

	N_x^{Al} (counts)	
Detector	^{238}U **chain**	^{232}Th **chain**
1	$2.2(4) \times 10^4$	$2.6(5) \times 10^4$
2	$3.3(6) \times 10^4$	$3.0(6) \times 10^4$
3	$2.7(6) \times 10^4$	$2.0(4) \times 10^4$
4	$2.6(6) \times 10^4$	$1.9(4) \times 10^4$
5	$2.6(5) \times 10^4$	$3.9(7) \times 10^4$
6	$2.5(5) \times 10^4$	$2.0(4) \times 10^4$
7	$3.5(8) \times 10^4$	$1.4(3) \times 10^4$
8	$2.1(4) \times 10^4$	$2.6(5) \times 10^4$
9	$3.1(7) \times 10^4$	$1.6(4) \times 10^4$
10	$2.4(5) \times 10^4$	$1.6(4) \times 10^4$
11	$2.5(5) \times 10^4$	$2.2(5) \times 10^4$
12	$3.6(7) \times 10^4$	$2.6(5) \times 10^4$

important to ensure that the fit minimizer does not use them interchangeably so each feature of the experimental spectrum is always described by the same model component. Achieving this resulted in consistency in N_{232U}^{Al} and N_{232Th}^{Al} values between different detectors, reflecting sufficient stability in the fit procedure. From here it is possible to perform an estimation of ^{238}U and ^{232}Th total activities in the scintillators using the previously established detection efficiency estimation ϵ_x^{Al}. Also, since the simulation accounts for the activity of all isotopes of the chain, all in equilibrium, the father's number of α-events is obtained by dividing over the sum of branching ratios. It is then used to calculate the activity by considering the total run time of the measurement as follows :

$$A_x^{Al} = \frac{1}{8} \times \frac{N_x^{Al}}{\epsilon_x^{Al}} \times \frac{1}{\Delta t} \tag{4.5.15}$$

where x refers to ^{238}U or ^{232}Th, A_x^{Al} the estimated activity of the father x in the aluminum and Δt is the total measurement duration of 3,019,367 s. Similarly, the ^{222}Rn activity in the liquid is estimated as :

$$A_{222Rn}^{Liq} = \frac{1}{4} \times \frac{N_{222Rn}^{Liq}}{\epsilon_{222Rn}^{Liq}} \times \frac{1}{\Delta t} \tag{4.5.16}$$

The preliminary assumption regarding the ^{222}Rn amount diffusing in the liquid can be verified by calculating the ratio between its aluminum and liquid activities. Using ϵ_{222Rn}^{Liq} values from Equations 4.5.8 and 4.5.9 gives its α-activity within 0.08 mm vessel thickness. Since the vessel is 2 mm thick and the α-emitters concentration throughout the volume is assumed to be constant, the ^{222}Rn activity in the whole vessel is scaled using the ratio of the two volumes. Thanks to secular equilibrium the vessel activities of ^{238}U and its daughter ^{222}Rn, respectively noted A_{238U}^{Al} and A_{222Rn}^{Al}, are taken as equal. The ratio between the two activities is therefore calculated as follows :
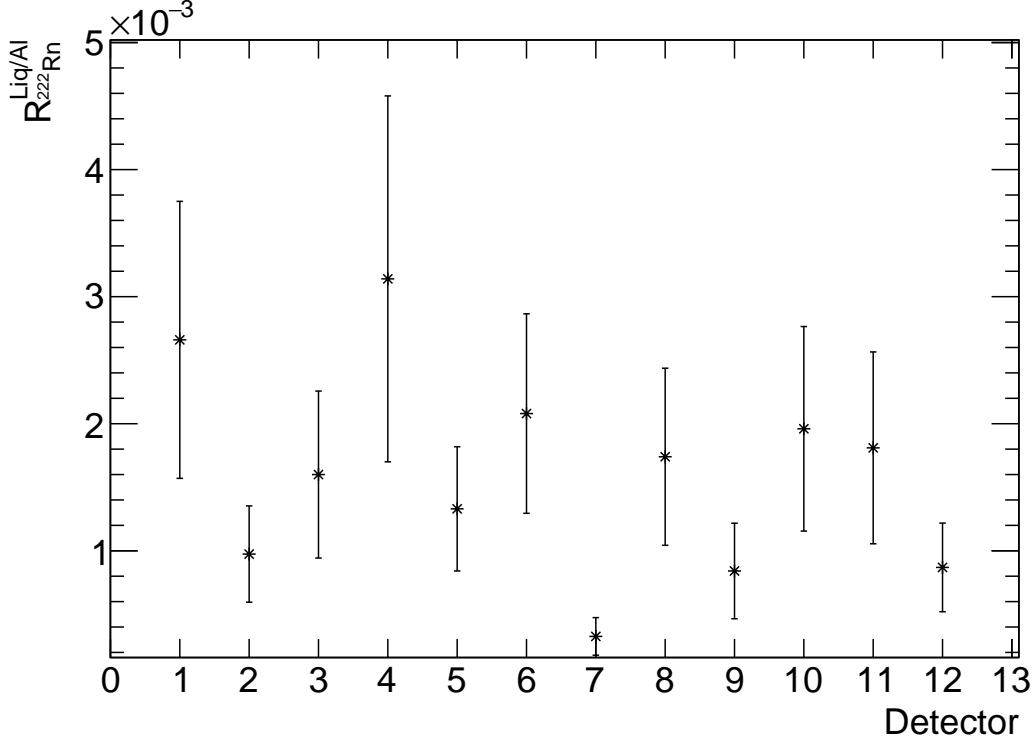
Figure 4.16: Estimated liquid over aluminum ^{222}Rn activity ratio for each detector.

$$R_{^{222}Rn}^{Liq/Al} = \frac{A_{^{222}Rn}^{Liq}}{A_{^{238}U}^{Al}} \times \frac{V_{2.00}^{Al}}{V_{0.08}^{Al}} \tag{4.5.17}$$

where $R_{^{222}Rn}^{Liq/Al}$ is the estimated ratio between ^{222}Rn activity in the liquid and the whole vessel and $V_{0.08}^{Al}$ and $V_{2.00}^{Al}$ are respectively the aluminum vessel volume considering 0.08 and 2 mm thickness. The results obtained repeating the same procedure for all scintillators are plotted in Figure 4.16. They show a ^{222}Rn activity in the liquid 3 to 4 orders of magnitude lower than that coming from the aluminum vessel. A difference that is sufficiently large to confirm the low diffusion assumption made when constructing $M(P_1, P_2, P_3)$ the fit model where the liquid and aluminum activities components are completely independent. Also, the radon concentration in the liquid is estimated to be <1 ppb, justifying the use of the 1/8 factor in Equation 4.5.21.

Concentration estimate results

From the parents α-activity estimated using Equation 4.5.15, it is possible to calculate the number of ^{238}U and ^{232}Th nuclei present in the vessel's effective volume. Using the decay constants and their uncertainties from literature [95][96], the relation between the N_x and A_x in the aluminum is written :

$$N_x = \frac{A_x}{\lambda_x} \tag{4.5.18}$$

where N_x is the estimated number of the x nuclei in a 0.08 mm thick aluminum vessel, N_x its α-activity and λ_x its corresponding decay constant. The number of ^{238}U and ^{232}Th atoms in the 0.08 mm thick sub-volume of the vessel can be

translated into concentration, noted $C^x_{\mu g/g}$; a quantity that facilitates comparison with literature data. The definition used here is that of the mass fraction of the contaminant, expressed in parts per million ppm which is defined throughout this work as $\mu g/g$. The masses of ^{238}U and ^{232}Th present in the considered aluminum volume are calculated using the molar density, as in Equation 4.5.19). Meanwhile, the mass of the vessel sub-volume is calculated using the aluminum volumetric mass density (see Eq.4.5.20). The ^{238}U and ^{232}Th masses are expressed in micrograms (μg) by using a factor 10^6, while the ^{27}Al in grams (g) to directly obtain a concentration value in ppm.

$$M_x = 10^6 \times \frac{N_x \cdot M_u(X)}{N_A} \tag{4.5.19}$$

where M_x is the total mass in μg of ^{238}U or ^{232}Th atoms present in a 0.08 mm thick vessel, $M_u(X)$ is the corresponding atomic mass and N_A is the Avogadro constant.

$$M^{Al}_{0.08} = V^{Al}_{0.08} \times \rho_{Al} \tag{4.5.20}$$

where $M^{Al}_{0.08}$ is the total mass in g of the effective 0.08mm thick aluminum vessel. $V^{Al}_{0.08}$ is its volume and ρ_{Al} is aluminum-27 density. Equations 4.5.8, 4.5.9, 4.5.15, 4.5.19 and 4.5.20 can be congregated into a unique relation linking the number of α-events the model attributes to each decay chain to the corresponding concentration value in the vessel, as follows :

$$C^X_{\mu g/g} = \frac{1}{8} \times \frac{N_x \cdot M_u(X)}{\epsilon_x \cdot \lambda_x \cdot \Delta t \cdot N_A \cdot V \cdot \rho_{Al}} \times 10^6 \tag{4.5.21}$$

where $C^x_{\mu g/g}$ is the parts per million (ppm) concentration of $X = [^{238}U, ^{232}Th]$ in the vessel, N_x the number of its detected α-particles, $M_u(X)$ its atomic mass in amu, ϵ_x the detection efficiency obtained by the simulation, λ_x its respective decay constant, Δt the total measurement time, N_A the Avogadro constant, V the effective volume of the detector aluminum vessel and ρ_{Al} the aluminum-27 density. The values of the constants used in Equation 4.5.21, their corresponding uncertainties, and units are reported in Table 4.10. The individual concentration results obtained for the shielded detectors can be seen in Figure 4.17. Even though the contamination is assumed to be different among detectors since the used aluminum to manufacture the vessel may originate from different locations, an average $C^x_{\mu g/g}$ value is however calculated resulting in 8.4 $(1.8)_{sta}$ $(1.4)_{sys} \times 10^{-2}$ and 1.62 $(0.57)_{sta}$ $(0.03)_{sys} \times 10^{-1}$ ppm for respectively ^{238}U and ^{232}Th. Comparison with values found in the literature is reported in Table 4.11.

4.6 Comparison with the available data

Several prior studies were conducted to quantify the amount of ^{238}U and ^{232}Th present in aluminum using different techniques. For a consistent comparison, results reported in this chapter are mainly compared to measurements performed on commercial aluminum samples, thus discarding those based on raw bauxite. The Nordic nuclear safety research (NKS) report concentration values reported in Table 4.11 and those of Kobayashi et al. [97] are obtained using the neutron activation

Table 4.10: Constants values used in Equation 4.5.21 to estimate ^{238}U and ^{232}Th concentrations in aluminum vessel.

	^{238}U	^{232}Th	
$M_u(X)$	238.050788 (2)	232.03805 (1)	$g \cdot mol^{-1}$
ϵ	7.52	9.21	%
λ	4.92 (1)	1.57 (1)	$10^{-18} \ s^{-1}$
Δt	3,019,367		s
N_{AV}	6.02214		$10^{23} \cdot mol^{-1}$
V	5.07		cm^3
ρ_{Al}	2.7 (1)		$g \cdot cm^{-3}$

method (see reference [98]), while those from the Barton et al. [83] are based on γ-spectrometer measurements performed using a HPGe detector. The α-spectroscopy methodology and ^{238}U and ^{232}Th concentration in aluminum as well as the previous ^{214}Po half-life results found in this thesis have been peer-reviewed and published in the Nuclear Instruments and Methods in Physics Research A scientific journal [93].

It is visible from Table 4.11 that the obtained values in this work are comparable to those found in the literature. This is despite the known dependency of actinide concentration on the geographical origin of the bauxite ore [99]. The results of this work are therefore strong evidence for α-spectroscopy to be a viable actinides concentration measurement alternative technique, producing results of similar quality uncertainty-wise. Regarding the implications of the findings discussed in this chapter on the SHADES ^{22}Ne(α,n)^{25}Mg measurement, it is clear that the α-background in the scintillators hinders the energy reconstruction of incident neutrons. The measured α-activity is around 64 events/h, while only a few neutron events/h are expected from low energy measurement runs. Time discrimination analysis, investigated in the following chapter, may however be a solution to this challenge, allowing α/neutron events discrimination through the use of information from the ^{3}He proportional counters. In any case, this doesn't pose a serious threat to the ^{22}Ne(α,n)^{25}Mg cross-section measurement since the main EJ-309 liquid scintillator detectors purpose is to act as a moderation medium, thermalizing the incident neutrons uncaptured by the ^{3}He counters.

Table 4.11: ^{238}U and ^{232}Th concentration values ranges from literature compared this work.

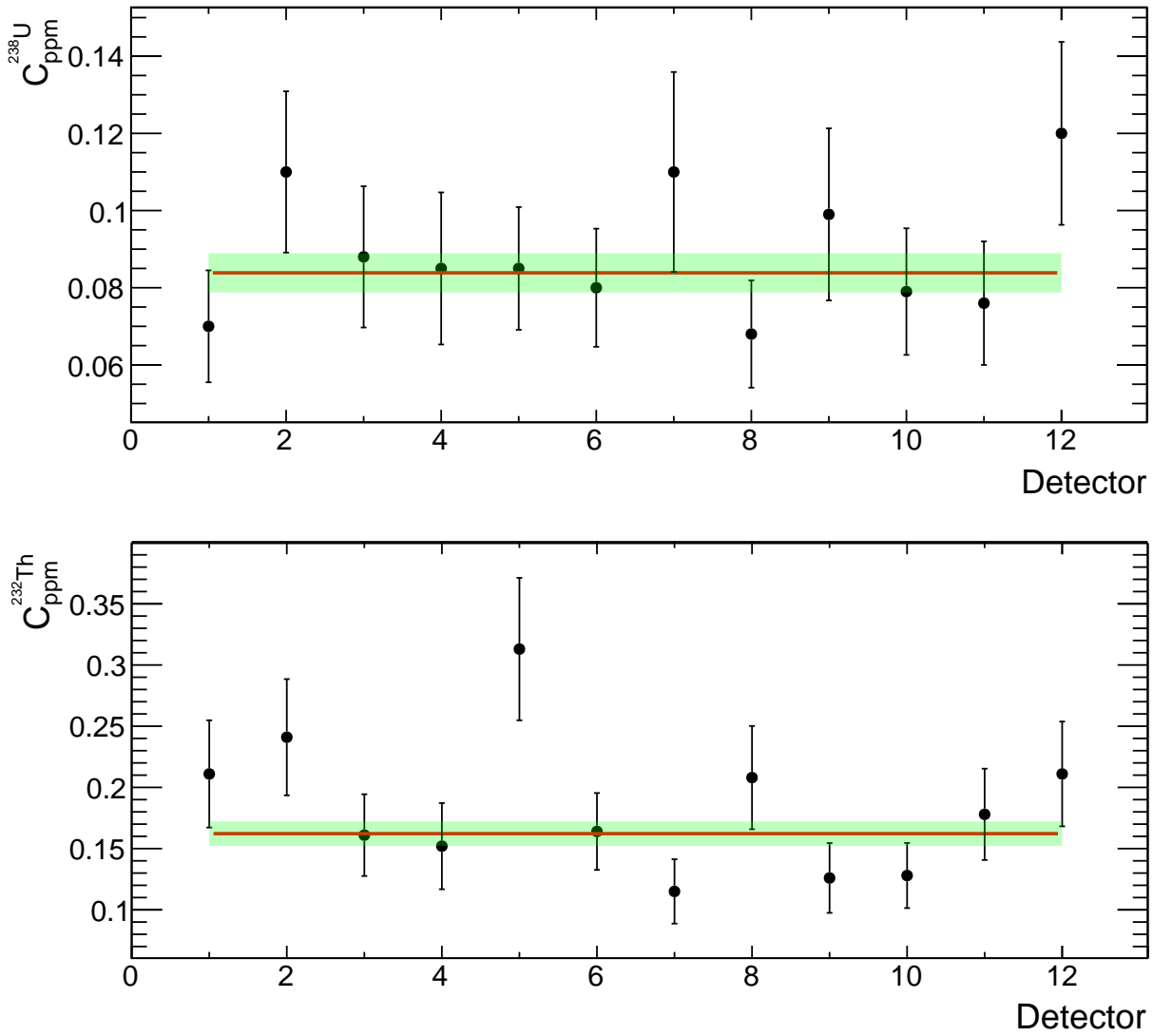| Ref.	$C^{238U}_{\mu g/g}$	$C^{232Th}_{\mu g/g}$
NKS [98]	0.8 - 3.5	0.7
JC BARTON [83]	0.35 - 0.99	N/A
Kobayashi [97]	0.1 - 0.22	N/A
Arpsella [100]	0.09 - 0.10	0.22 - 0.26
Leonard [101]	< 0.01	< 0.05
This Work [93]	0.07 - 0.12	0.11 - 0.31

Figure 4.17: Individual ^{238}U and ^{232}Th concentration in each EJ-309 liquid scintillator. The red line represents the weighted average of all data points and the green band its corresponding uncertainty range.

Chapter 5

EJ-309 neutron response

[3]He proportional counters have a high thermal neutron capture cross-section [61]. Moderators are therefore often used to slow down higher-energy neutrons considerably improving the detection efficiency. In the case of the SHADES project, the array of scintillators acts as a moderator. This increases the setup's overall detection efficiency while sometimes allowing the reconstruction of their initial energies deposited in the EJ-309 scintillating liquid. A proper neutron energy calibration is therefore essential for the understanding of the obtained spectra. In this work, the neutron light response study of SHADES EJ-309 liquid scintillators is investigated shooting several neutron beams of known energies into a single detector. The obtained channel-to-energy association allows the establishment of a proper energy calibration. However, this requires an adapted PSD analysis to identify neutron events, which is challenging at low energies. The resulting energy and PSD information from this analysis is also crucial for the gating of the time coincidence filtering algorithm.

5.1   Experimental apparatus

The energy calibration series of measurements were performed in July 2022 at the Goethe University of Frankfurt[1]. Its nuclear physics facility includes a Van de Graaff accelerator (VdG), able to provide a terminal voltage of 1 to 2.5 MV and a beam current up to 10 µA, specialized in neutron beam production. A wide range of experimental and post-process analysis tools [102] are also available for users, such as a neutron flux estimation Monte-Carlo simulation and a VdG energy calculator, both used in this work. The measurement campaign lasted for a full working week, with the first day dedicated to the experimental setup mounting and testing. A local operator handled the beam tuning for each run following a pre-agreed list of energies to scan, with a targeted measurement time of around 1 hour (see Table 5.1). The investigation of both the neutron energy response of the detector -using the ^{7}Li(p,n)^{7}Be nuclear reaction- and the time coincidence filtering algorithm is performed using a simplified version of the SHADES detection array. This latter consists of one EJ-309 liquid scintillator (unit n°5) surrounded by 6 ^{3}He counters -described in Chapter 3- inside 2 parallel aluminum holders (see Figure 5.1). The center-to-center distance between the scintillator and the counters is 9.76 cm. The data acquisition system relied on the facility's HV module (power supply) while using SHADES' DT5725B digitizer. A remotely accessible DAQ computer -on which

---

[1]This part of the work was supported through Chetech-INFRA, project n° 2574
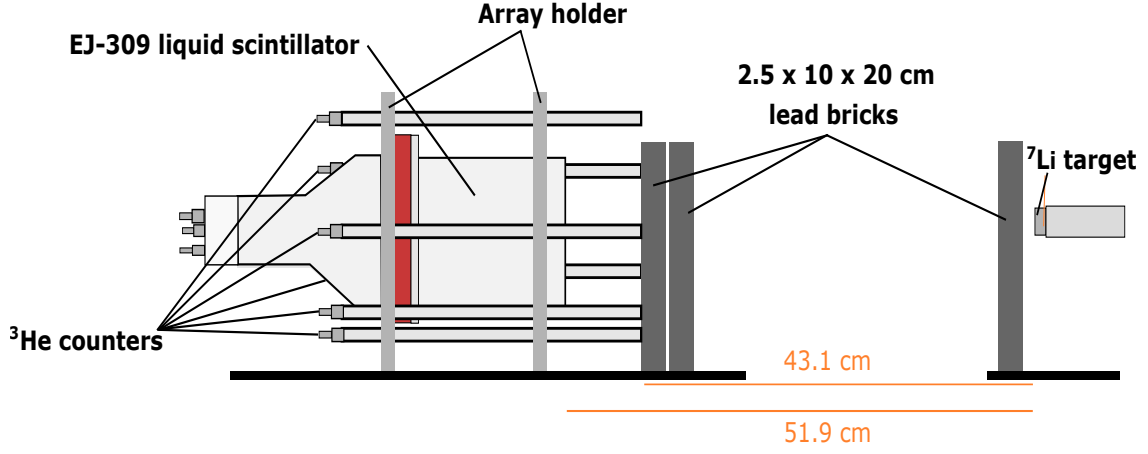
Figure 5.1: Simplified version of the SHADES detection array used for neutron calibration and time coincidence tuning. Distances not in scale.

the CoMPASS software is installed- is used to record and store the measurement data. The ^{3}He-filled counters were plugged into 2 × 4-channels CAEN A1422B preamplifiers [103], applying 750 V for each. The chosen scintillator was directly connected to the digitizer and fed with its corresponding optimal voltage from Table 3.1. The setup is placed such that the bottom of the detectors faces the ^{7}Li target. To reduce the beam-induced γ-rays reaching the detector, 3 lead bricks of 2.5 × 10 × 20 cm were placed in between as can be seen in Figure 5.1.

Since charged particle accelerators cannot directly produce neutron beams, these latter are obtained by inducing the ^{7}Li$(p, n)^7$Be (Q = -1.644 MeV) nuclear reaction [104]. The negative Q-value reflects its endothermic nature, implying a proton energy threshold of :

$$E_p^{th} = -Q \cdot \frac{(m_n + m_{^7Be})}{m_n + m_{^7Be} - m_p} = 1.88 \text{MeV}. \tag{5.1.1}$$

where E_p^{th} is the proton energy threshold, m_n the mass of a neutron, and $m_{^7Be}$ the mass of Beryllium-7. At the threshold energy E_p^{th}, the reaction produces 30 keV neutrons at a forward 0° angle. For $1.88 < E_p < 1.92$ MeV, neutrons are emitted in a narrow forward peaked cone, with two possible values for the neutron energy E_n at each angle. For $E_p > 1.92$ MeV, only one E_n value is permitted at each emission angle. However, increasing E_p enlarges the emission cone, widening the neutron emission energy spectrum. The energy resolution of the neutron beam depends on many parameters such as the beam spread of the proton beam and the target dimensions (thickness, radius).

The facility's VdG accelerator induces the ^{7}Li$(p, n)^7$Be reaction by bombarding a 3.1 μm thin layer of ^{7}Li on copper (see Figure 5.2). As discussed above, the neutron energies depend on the emission angle because of the reaction's kinematics. For this reason, the experimental setup was placed as far as possible from the target to limit the angle exposure and thus the energy dispersion of neutrons reaching the detector. This latter is determined using the PINO[2] Monte-Carlo-based simulation tool [105] and taken in consideration when performing the neutron energy calibration (see

---

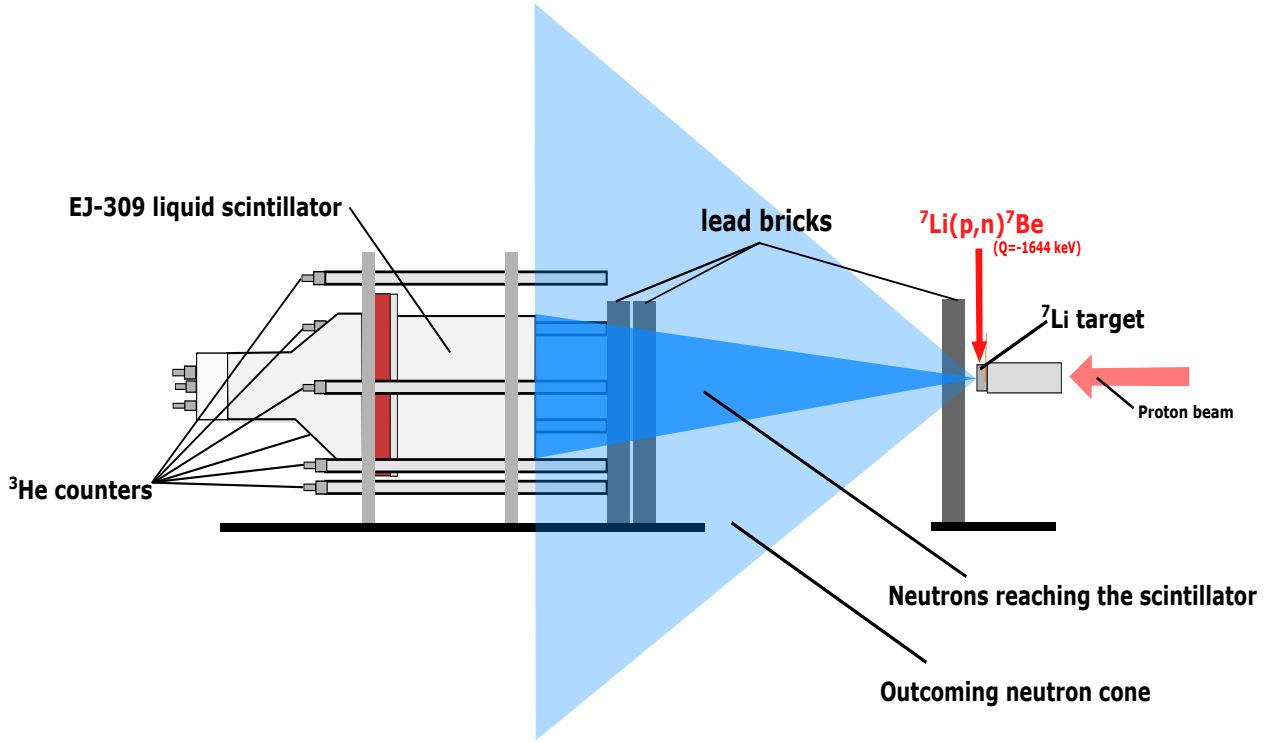[2]Protons In Neutrons Out - Tool available at `exp-astro.de/pino/` - Reference [105]

**Figure 5.2:** Emitted neutron cone. Distances and angles not in scale.

Section 5.5). The neutron energy spectrum from a 1912 keV proton beam covers all energies up to 106 keV. Nevertheless, since the scintillator is located 51.9 cm from the target, the actual spectrum of neutrons reaching its geometry is mostly located between 45 and 106 keV (see Subfigure 5.3(a)). This is because the detector's bottom surface only covers 8.4° out of the 67.7° total emission angle. The simulation also provides an estimation of the $^7\mathrm{Li}(\mathrm{p,n})^7\mathrm{Be}$ yield which is, at this E_p energy, 4.06×10^{-6} neutrons per proton from which 1.24×10^{-7} do reach the scintillator. An important piece of information to acknowledge regarding the facility's VdG accelerator is that, for example, to produce a proton beam of the standard energy E_p = 1.912 MeV, an energy of 1.889 MeV must be targeted on the control software. This is because the machine relies on the magnet calibration reading, therefore requiring calculating the correct VdG energy corresponding to the wanted proton energy E_p. The facility offers an online tool [106] to perform the conversion that is based on the following linear relation :

$$E_p^{\mathrm{VdG}}[\mathrm{keV}] = ((1 - 0.023) \cdot E_p - 21.971)[\mathrm{keV}] \tag{5.1.2}$$

where E_p^{VdG} represents the input proton beam energy in keV targeted by the VdG and E_p is the actual obtained proton energy, also in keV.

5.2 Neutron beam measurements

To establish the neutron energy calibration, a series of measurements are performed on the detection array using different proton beam energies in 50 keV steps. The covered range extends from the near-threshold E_p = 1900 keV energy up to 2450 keV where both $^7\mathrm{Li}(\mathrm{p,n})^7\mathrm{Be}$ and $^7\mathrm{Li}(\mathrm{p,n_1})^7\mathrm{Be}$ are activated. This latter generates a second neutron population n_1 from the first excited level of $^7\mathrm{Be}$ (E_x = 0.43 MeV).
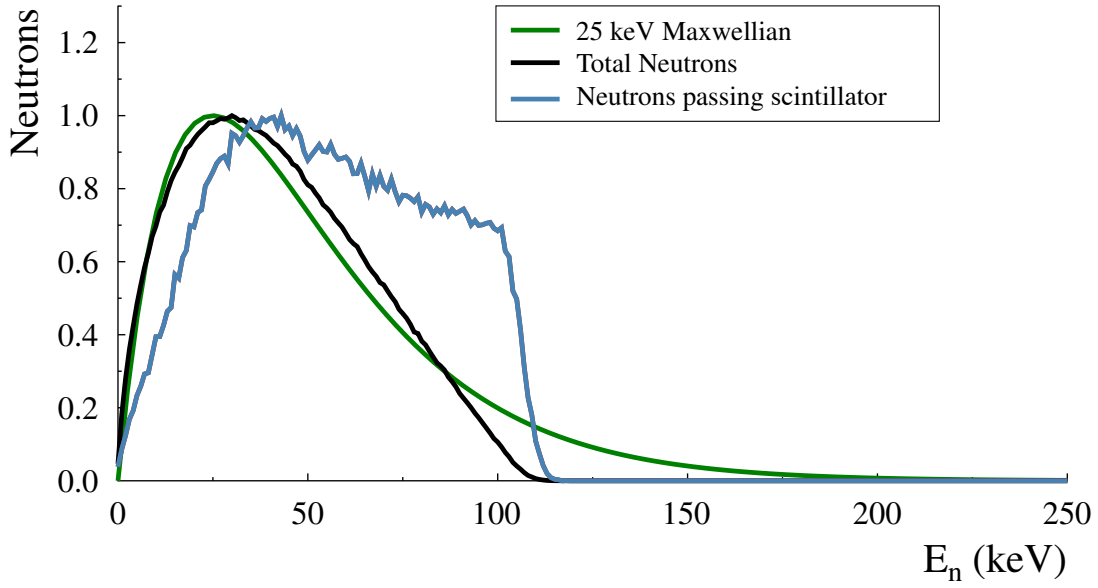
(a)
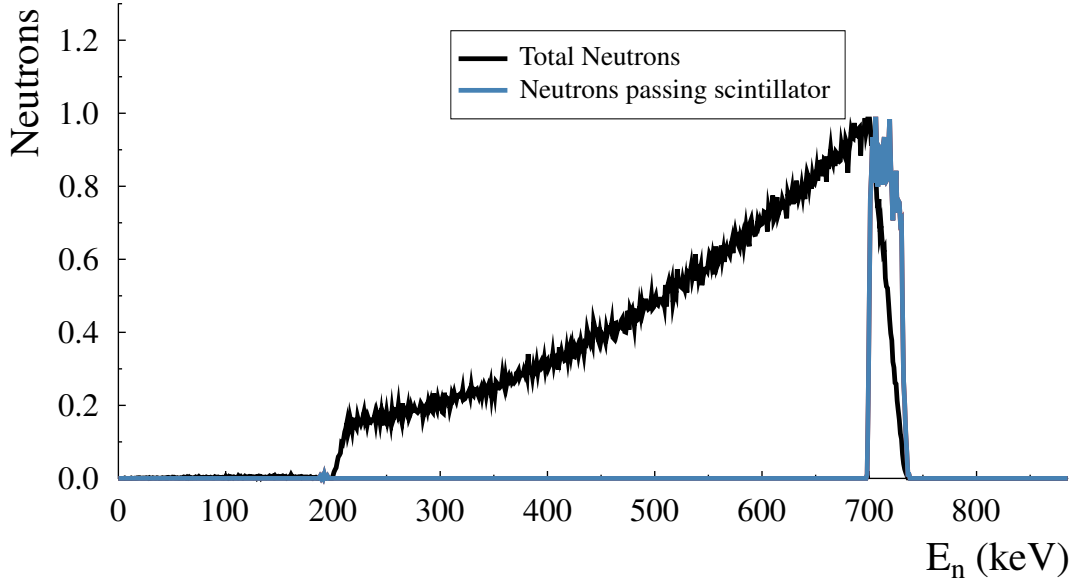
(b)

Figure 5.3: Expected energy spectrum, according to PINO simulation, of neutrons reaching the EJ-309 liquid scintillator in the Frankfurt measurement. In panel (a) is the proton beam energy at $E_p = 1912$ keV while in panel (b) is that at $E_p = 2450$ keV.

A beam current of 150 - 200 nA was targeted throughout the majority of runs and the current reading information was saved for more precise efficiency and time coincidence analyses. Some measurements were however purposely reconducted using a lower current to cross-check some experimental conditions such as the possible effect of high current beams on DAQ dead time. The full list of used beam energies and their associated current value is reported in Table 5.1.

Three other beamless runs were conducted to respectively measure the γ-background, ^{60}C and ^{137}Cs radioactive sources spectra to build a γ-energy calibration useful for the study of neutron energy quenching in EJ-309. The gathered data from all detectors is saved in ROOT format for each measurement and named after the corresponding VdG energy. Each event contains information about the waveform, timestamp, board number, channel, and flag. Saving the individual pulses resulted in a very large amount of data to be processed (from 10 to 60 GB per run depending on the chosen detection threshold). This information is however crucial to later perform a PSD analysis and identify the neutron signals region. The waveform length was extended to 4992 ns allowing more PSD long gate values to be investigated for the figure of merit optimization. The CoMPASS DAQ software used to record and save the data also outputs information about the dead time. Contrary to the underground measurement discussed in Section 4.1, the events rate is here high enough to provoke a non-negligible detector dead time (up to 10%) that must be taken into consideration when analyzing the data. In total, 19 runs were accomplished following a decreasing VdG energy order. It is important to mention that the first run at E_p^{VdG} = 2414 keV was performed applying a 975 V voltage on the scintillator, 50 V lower than the optimized value. This was corrected for the rest of the campaign starting from the following run. All other runs were therefore conducted with the optimized voltage value, including background and radioactive sources measurements. Data from run 10 performed at E_p^{VdG} = 2150 keV was also lost because of unnoticed accelerator valve closure. Nevertheless, the saved file could be used as an extra background measurement.

5.3 PSD analysis

Other than an AmBe source that emits neutrons in a large energy continuum, the energy range covered by the produced neutron beam is more restricted and of a similar order of magnitude to the detector resolution. It is therefore expected to produce a localized circular spot in the bi-dimensional PSD figure, instead of a long horizontal peak as in Figure 3.15. The generated neutrons during the measurement are of low energy and fall in the region where the γ/n separation becomes less effective. A corresponding optimised PSD parameters must therefore be established for this data set. Similarly to previous analyses discussed in Chapters 3 and 4, this is done by maximizing the FoM value using different short/long gate combinations (see Equation 3.5.3). Ideally, the PSD analysis must be performed using data from the lowest neutron energy run. The neutron/γ separation is however there completely lost requiring a compromise. In this work, the intermediary proton beam energy E_p = 2198 keV run is chosen since it is the lowest to produce a complete separation suitable for FoM analysis. A conclusion based on the PSD analysis results of data from all runs using the previously established optimized short and long gate values for the AmBe source (see Figure 5.4). To better focus the separation on the low energy part in the upcoming FoM analysis, only events with an Energy < 200 keVee
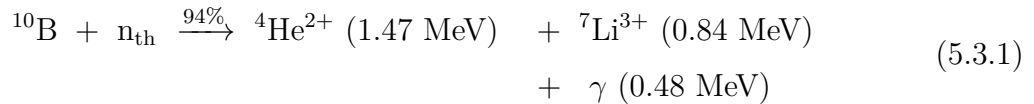
Table 5.1: Investigated proton beam energies. The first column reports the targeted proton energy on the VdG. In between parentheses is reported whether a low current is used during the run. Column 2 is the proton energy according to Equation 5.1.2 and column 3 is the targeted beam intensity and column 4 is the measurement time.

E_p^{vdg} [keV]	E_p [keV]	I_{tar} [nA]	runtime [s]
1878	1900.5	30	3495
1926	1949.6	120	2416
1975	1999.8	150	3301
2024	2050	150	3357
2072	2099.1	250	3651
2122	2150.3	150	3760
2169	2198.5	150	2498
2171 (lowI)	2200	35	3488
2219	2249.7	200	2000
2268	2299.8	200	5407
2317	2350	200	4506
2366	2399	200	5605
2414	2449	200	1239
2415 (lowI)	2450	35	3546

are considered. A region that includes the whole neutron activity while limiting the influence of high energy γ-rays. The investigated short gate values extend from 56 up to 144 ns, while the long gate can be found in the 360 to 2000 ns range. The results of this procedure, plotted in Figure 5.5, show a maximized FoM value at S = 80 ns and L = 640 ns. PSD, energy calibration, and ^{3}He-Scintillator time coincidence analysis of data from all different measurements are then performed with those parameters using 100% of the available data. The FoM is then calculated for all measured beam energies using the newly established short/long combination. The obtained values in each case are reported in Table 5.2).

Boron contamination

In addition to the expected neutron signal, the PSD analysis shows a less-intense mono-energetic population around PSD = 0.3 and Energy = 100 keVee usually populated by neutron and α-events. It is visible from measurements performed at $E_p \leq 2200$ keV and below that this activity does not depend on the proton beam energy (see Figure 5.6). It is reasonable to assume that it is due to thermal neutron capture by boron present in the liquid. The detector manufacturer does also produce boron-doped EJ-309 liquid scintillators with a high thermal neutrons capture yield. In nature, boron is present in two stable forms: ^{11}B at 80.1(7)% and ^{10}B at 19.9(7)% [107]. The capture of slow neutrons n_{th} by ^{10}B mostly occurs as follows :

$$^{10}\text{B} + n_{th} \xrightarrow{94\%} {}^4\text{He}^{2+} (1.47 \text{ MeV}) + {}^7\text{Li}^{3+} (0.84 \text{ MeV})$$
$$+ \gamma (0.48 \text{ MeV}) \tag{5.3.1}$$

Even though the measurements are performed with a non-doped model, the presence of boron traces is not to be excluded inside the scintillator due to cross-contamination
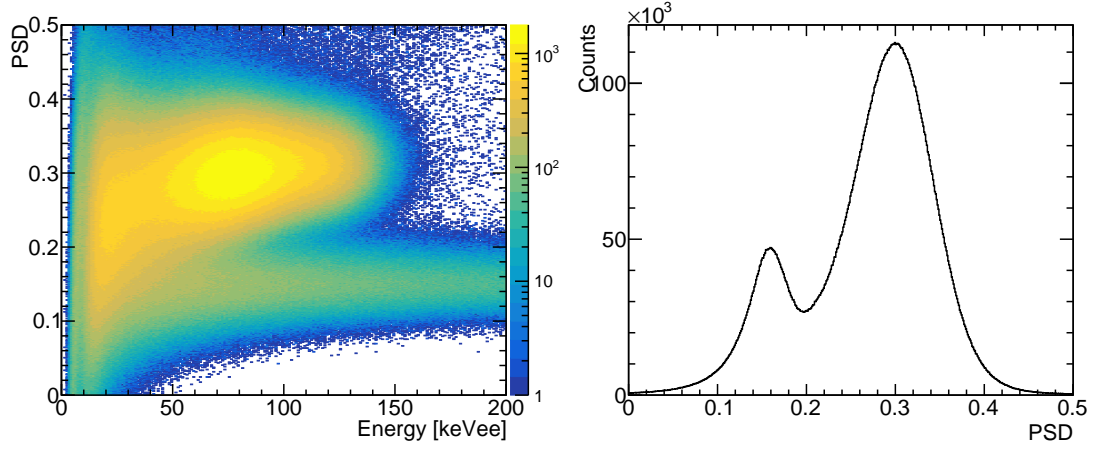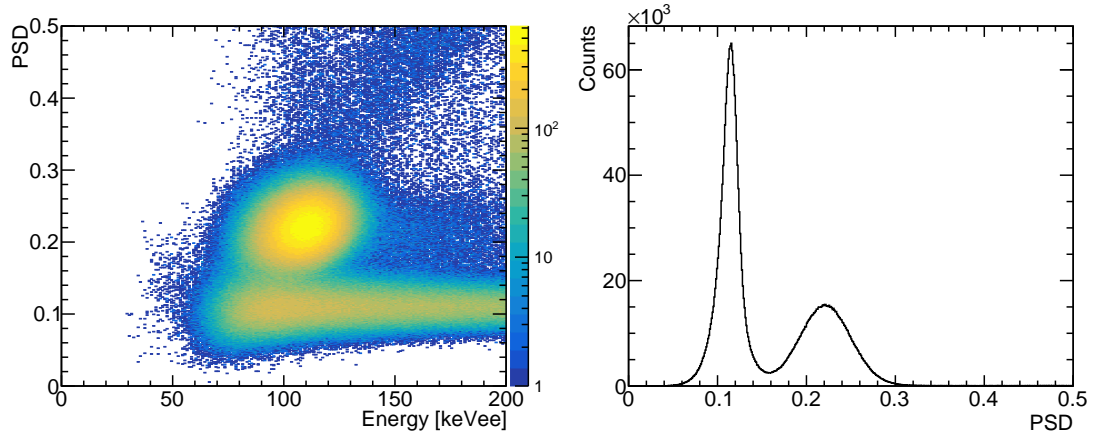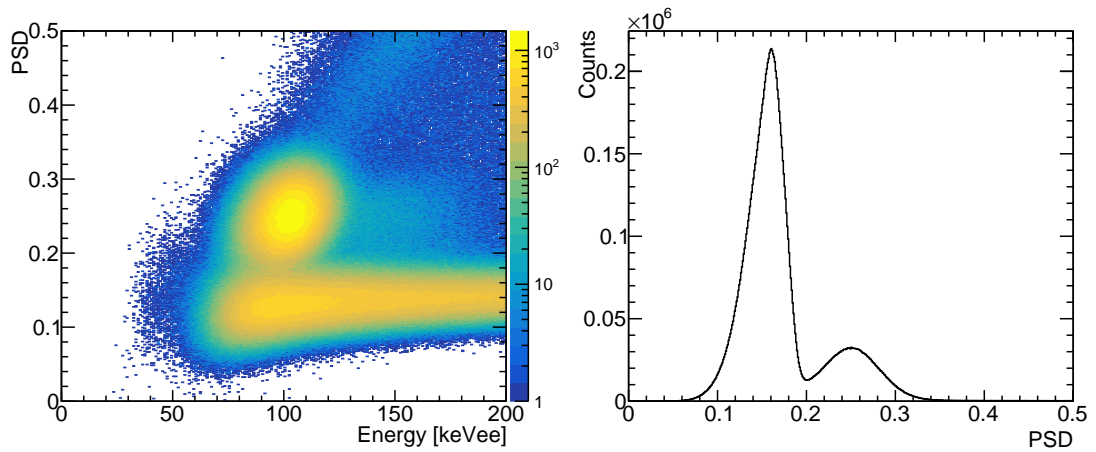
(a) E_p = 2450 keV (low current and threshold)

(b) E_p = 2449 keV

(c) E_p = 2400 keV

Figure 5.4: Plotted neutron beam on EJ-309 bi-dimensional PSD analysis result (left) and their projections on the y-axis (right) obtained using short and long gates values optimized for an AmBe source.
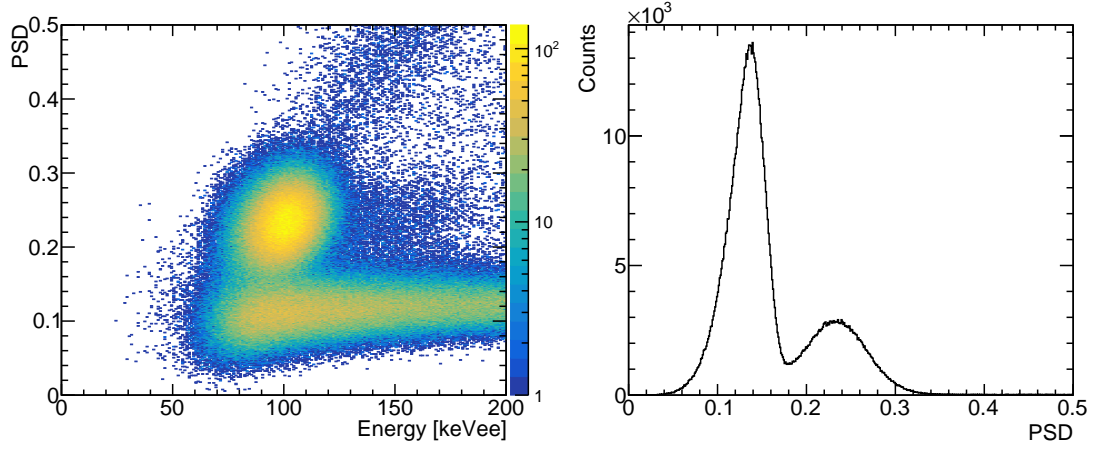
(d) $E_p = 2350$ keV

(e) $E_p = 2300$ keV

(f) $E_p = 2250$ keV

Figure 5.4: Plotted neutron beam on EJ-309 bi-dimensional PSD analysis result (left) and their projections on the y-axis (right) obtained using short and long gates values optimized for an AmBe source.
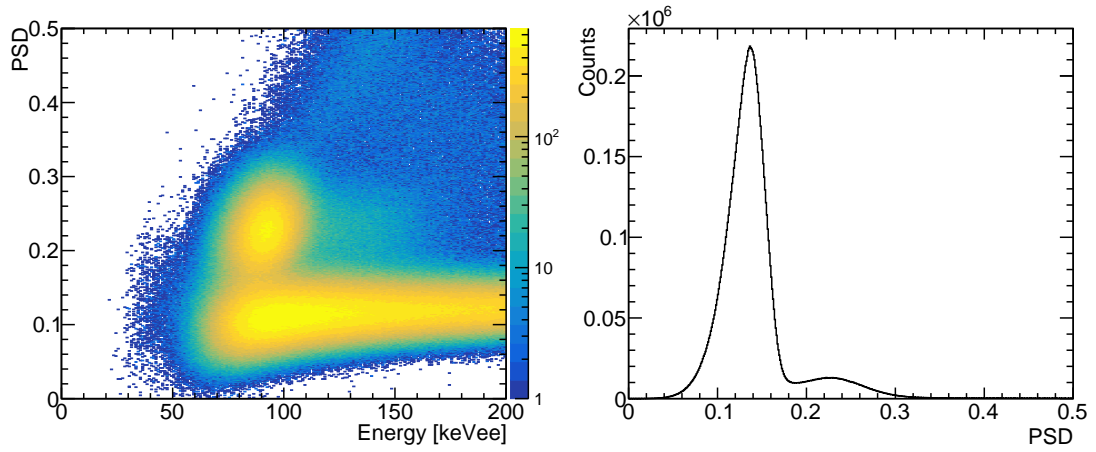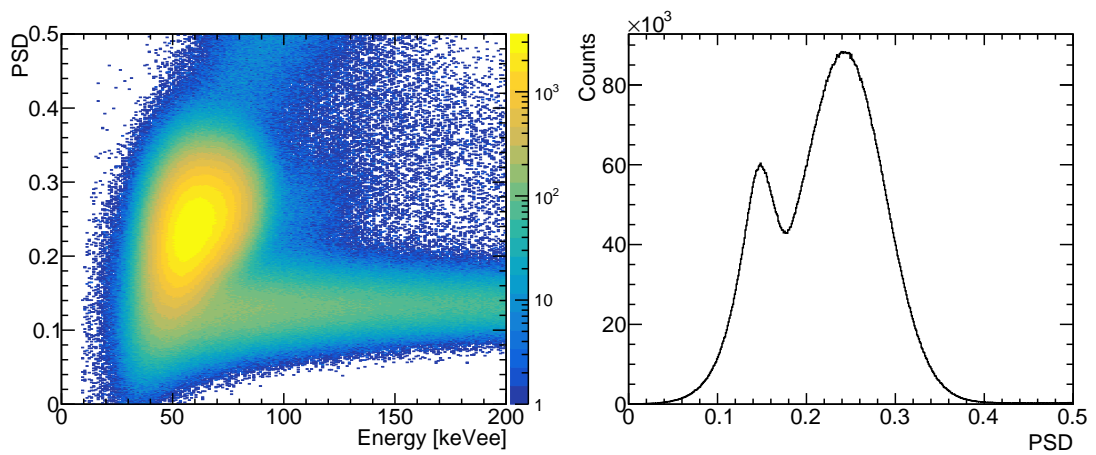
(g) $E_p = 2200$ keV (low current and threshold)

(h) $E_p = 2198$ keV

(i) $E_p = 2150$ keV

Figure 5.4: Plotted neutron beam on EJ-309 bi-dimensional PSD analysis result (left) and their projections on the y-axis (right) obtained using short and long gates values optimized for an AmBe source.

(j) $E_p = 2100$ keV

(k) $E_p = 2050$ keV

(l) $E_p = 2000$ keV

Figure 5.4: Plotted neutron beam on EJ-309 bi-dimensional PSD analysis result (left) and their projections on the y-axis (right) obtained using short and long gates values optimized for an AmBe source.
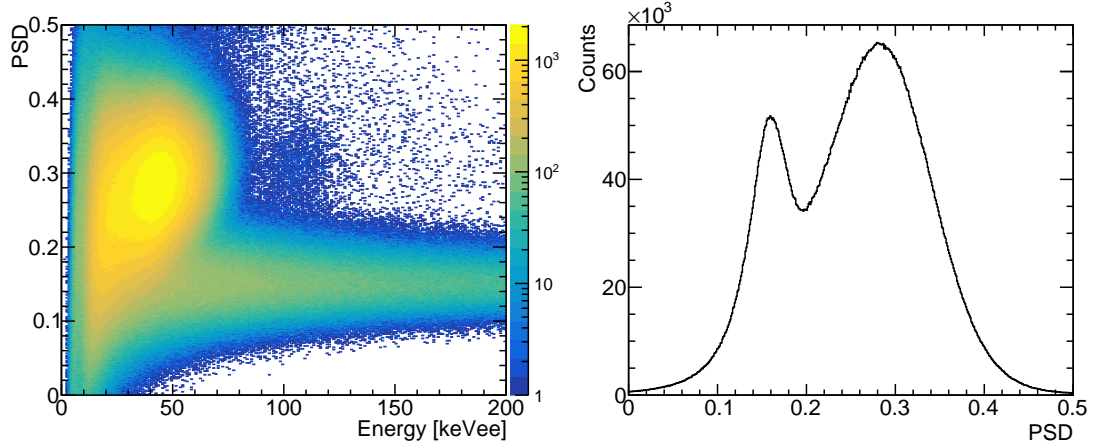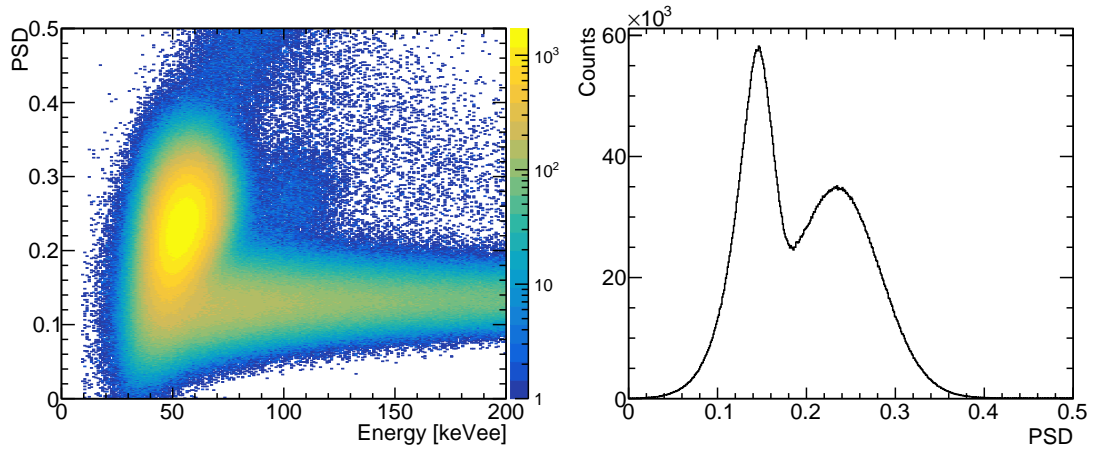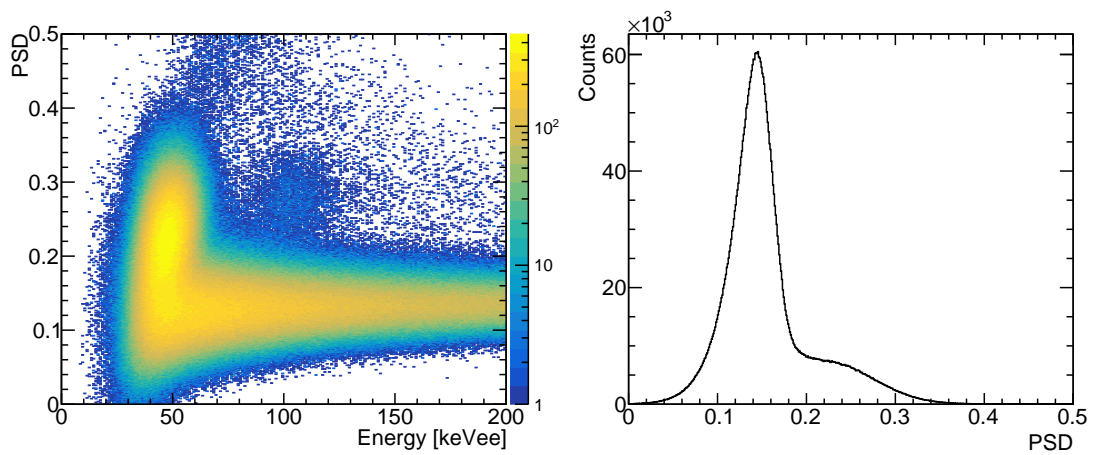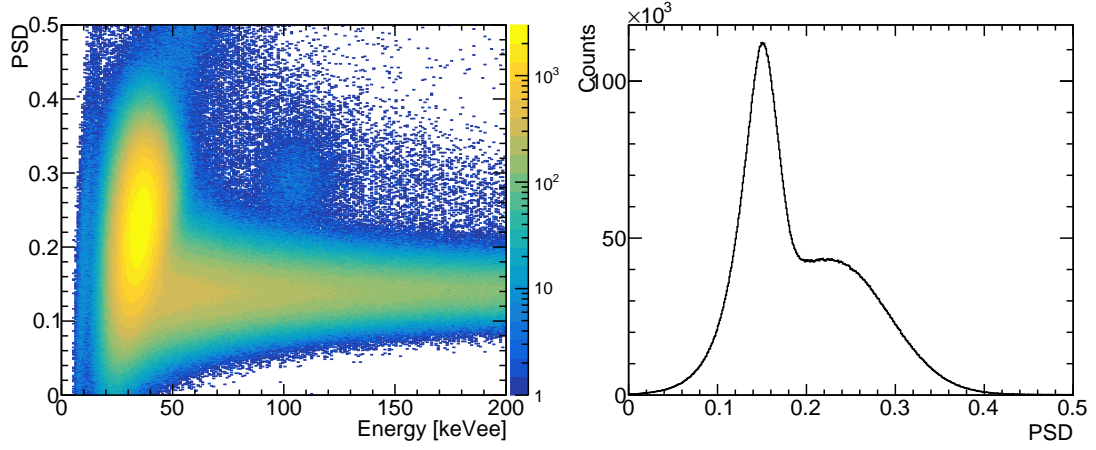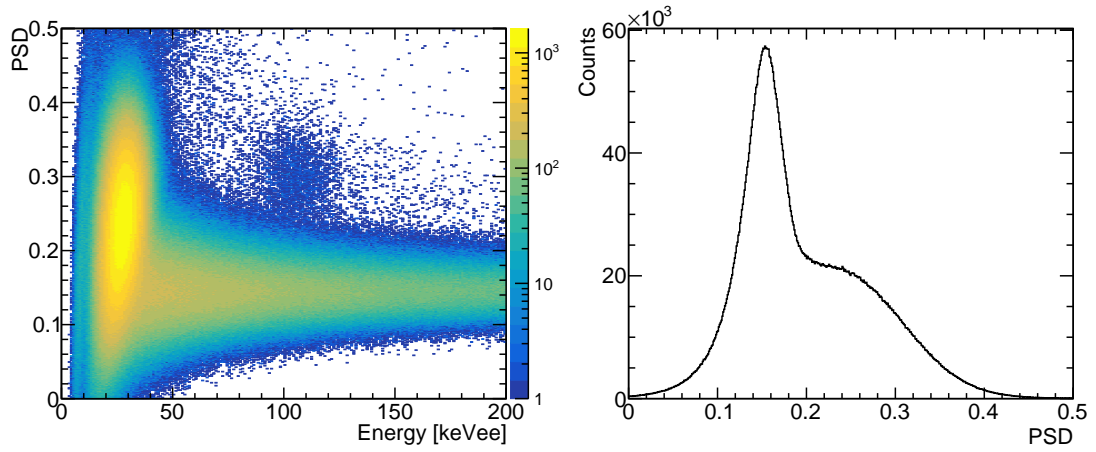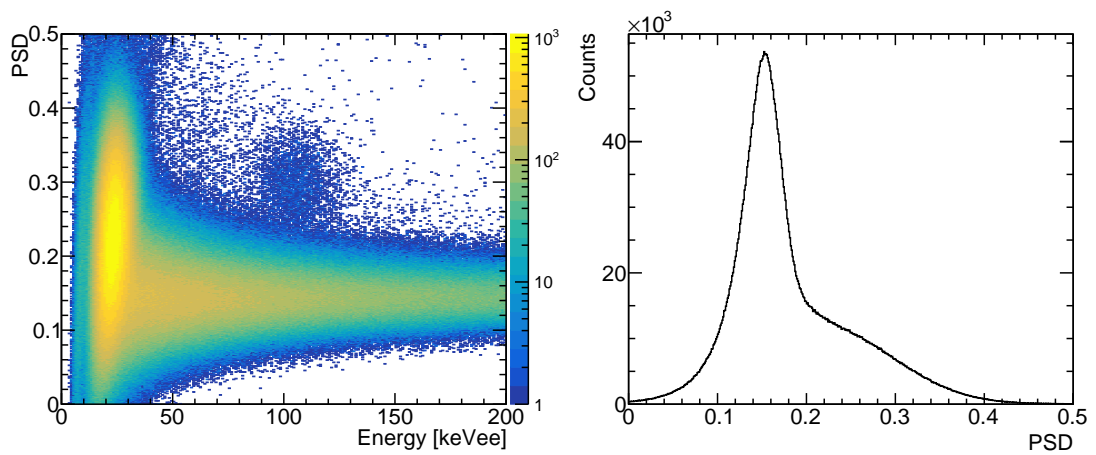
Table 5.2: Achieved γ/neutron separation for at all measured proton beam energies. The PSD distribution used to calculate the FoM uses the short/long combination optimized for the run at $E_p \approx 2200$ keV (i.e. S = 80 ns and L = 640 ns) and an upper energy cut at 200 keVee.

E_p (keV)	FoM
1900	0.10
1950	0.30
2000	0.27
2050	0.37
2100	0.43
2150	0.44
2200	0.60
2250	0.66
2300	0.72
2350	0.83
2400	0.89
2449	0.95

that may have occurred during the manufacturing process. According to the detector application note produced by the manufacturer [108], the activity from this capture reaction is expected at around 100 keVee for EJ-309-based liquid scintillators. The fact that the observed activity in the above measurements is located around the same energy further supports this assumption. Furthermore, α-particles produced from the thermal neutron capture reaction (see Equation 5.3.1) have an energy of 1.47 MeV which translates to around 100 keVee following the quadratic α-energy quenching relation previously established using the underground measurement data (see Figure 4.10). It is then safe to conclude that the observed is indeed due to boron contamination in the detector. This latter result represents an important piece of information that must be taken into consideration when measuring the ^{22}Ne(α,n)^{25}Mg reaction cross-section. This is because it accounts for the thermalized neutrons that are captured by boron instead of reaching one of the ^{3}He counters.

5.4   Neutron events quantification

Despite targeting a constant proton current value in the VdG accelerator, output data showed that its value has been varying throughout each measurement (see Subfigure 5.8(a)). To estimate the number of neutrons reaching the detector, this variation is taken into account by using the total accumulated charge (Q) in the target together with ^{7}Li(p,n)^{7}Be cross-section and neutrons angular distribution in the cone at the specific beam energy. This latter quantity is obtained from the PINO simulation, expressed as the number of produced neutrons reaching the scintillator per proton, thus also accounting for the geometrical efficiency of the setup. The intrinsic neutron detection efficiency of the ^{3}He counters array and that of the EJ-309 liquid scintillator can then be established by quantifying the number of neutrons measured in both types of detectors. For measurement using proton beams with an energy under 2200 keV in the scintillator, γ and neutron distributions overlap as can be seen in Figures 5.6. The individual contributions must therefore be disentangled to estimate the number of events in the detector that can be associated
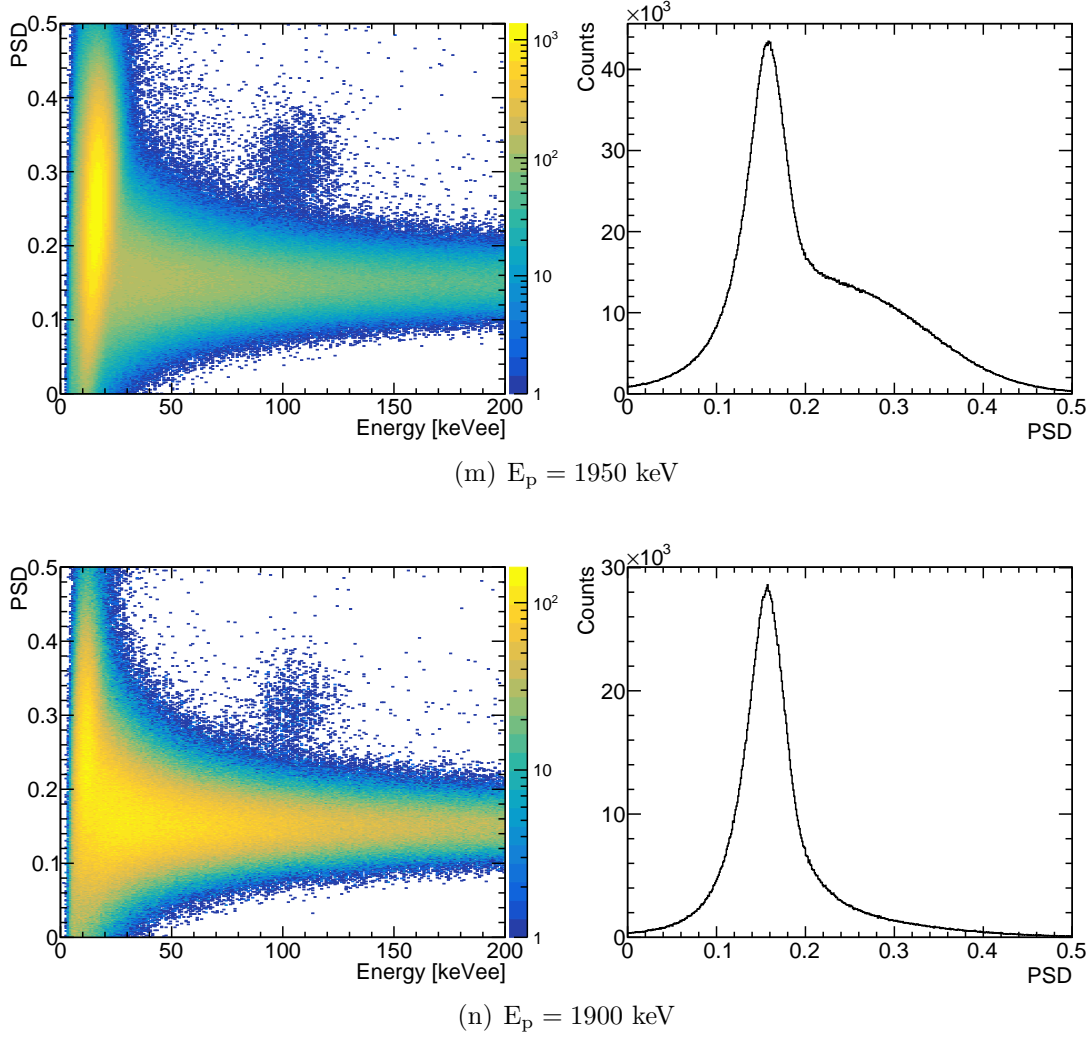
(m) $E_p = 1950$ keV

(n) $E_p = 1900$ keV

Figure 5.4: Plotted neutron beam on EJ-309 bi-dimensional PSD analysis result (left) and their projections on the y-axis (right) obtained using short and long gates values optimized for an AmBe source.

with neutrons. This is here achieved by fitting the PSD distribution with a sum of two Gaussian functions as in the FoM analysis. The number of detected neutrons is then considered as the total integral of the corresponding Gaussian (see Figure 5.7). This method of estimating the number of detected neutrons applied to all runs resulted in efficiencies of less than 6% which is compatible with previous works such as [109]. This efficiency is, of course, very dependent on the chosen minimum energy detection threshold which did here vary depending on the proton beam energy for several technical reasons (minimizing dead time, saving storage, filtering low energy events...).

Distinguishing neutron events in the ^{3}He counters is a more straightforward process thanks to the properties of their corresponding energy spectra (see Figure 3.4). It is indeed sufficient to perform a numerical integration between channels 150 and 3500 in the uncalibrated spectra (see Figure 5.14) to obtain the number of detected thermal neutrons. As previously stated in Section 3.2, ^{3}He counters have a very low detection efficiency for non-thermal neutrons. Since those are not directly expected from the ^{7}Li source, their origin is therefore attributed to thermalization in the EJ-309 liquid cell. The efficiency calculated using the counts number from
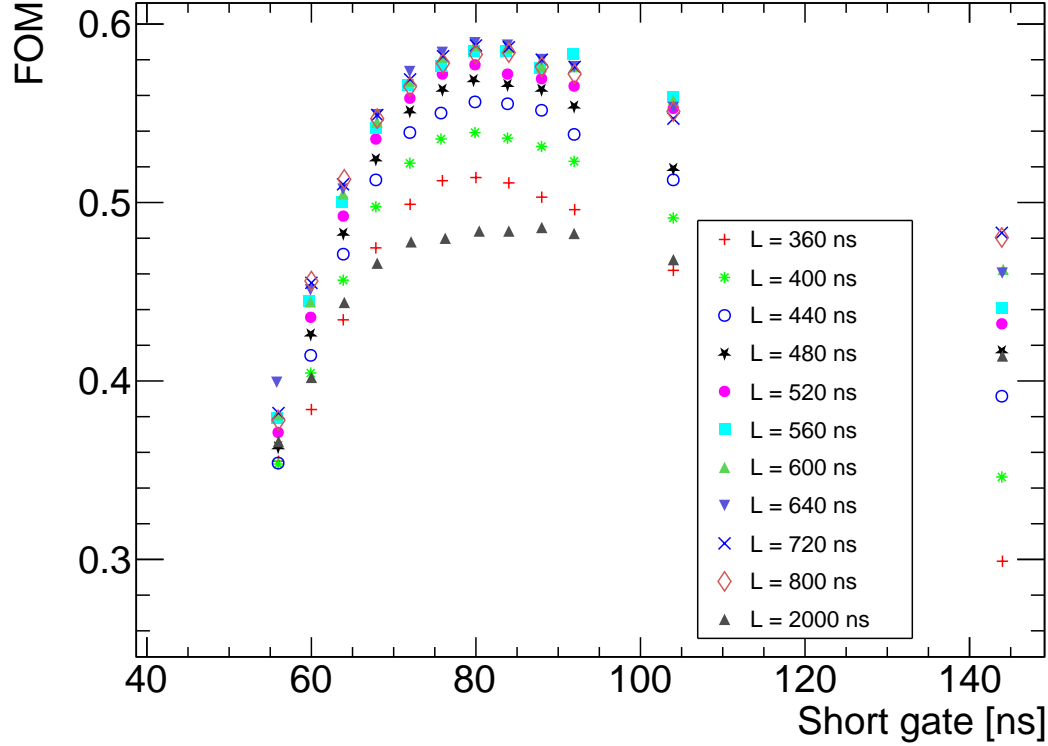
Figure 5.5: Figure of merit value at different short/long combinations for the ~2200 keV proton beam energy data.

the ^{3}He counters energy spectra does therefore refer to that of the thermalization and geometrical coverage of the tubes around the scintillator rather than that of the detection efficiency of the ^{3}He tubes ring facing the ^{7}Li target.

5.5   Neutron energy quenching

Contrary to α-particles detection discussed in Section 4.4, the neutron beam in this measurement is not strictly mono-energetic. Simulation using the PINO tool shows neutron distributions 40 to 95 keV wide, for proton beam energies of respectively E_p = 2450 and E_p = 1900 keV, producing the observed neutron PSD signature. The experimental energy spectrum of the corresponding region (2σ around the mean) shows a Gaussian-like shape that is a consequence of the detector's limited resolution for such close neutron energies (see Subfigure 5.9(a)). A way to overcome this complication is to establish the light output to neutron energy correlation according to the centroids of both experimental and simulation of the neutron beam spectra. A unique neutron beam energy E_n is attributed to each, calculated as the mean energy of the distribution predicted by the PINO simulation (see Subfigure 5.9(b)). The results of this procedure, performed on all measurements, are shown in Table 5.3. The PINO tool is built to handle activation samples of very negligible thicknesses [105]. Using a scintillator with a cylindrical 5"×5" energy-sensitive liquid cell may have introduced an uncertainty on the determination of E_n using the simulation result since its front, center and back cover slightly different angles of the neutron emission cone (8.5°, 7.3° and 6.7° respectively). Another source of potential uncertainty is the ^{7}Li target thickness. The quoted 3.1μm may have been subject to

(a) $E_p = 2450$ keV (lowI)

(b) $E_p = 2449$ keV

(c) $E_p = 2399$ keV

(d) $E_p = 2350$ keV

(e) $E_p = 2300$ keV

(f) $E_p = 2250$ keV

(g) $E_p = 2200$ keV

(h) $E_p = 2199$ keV
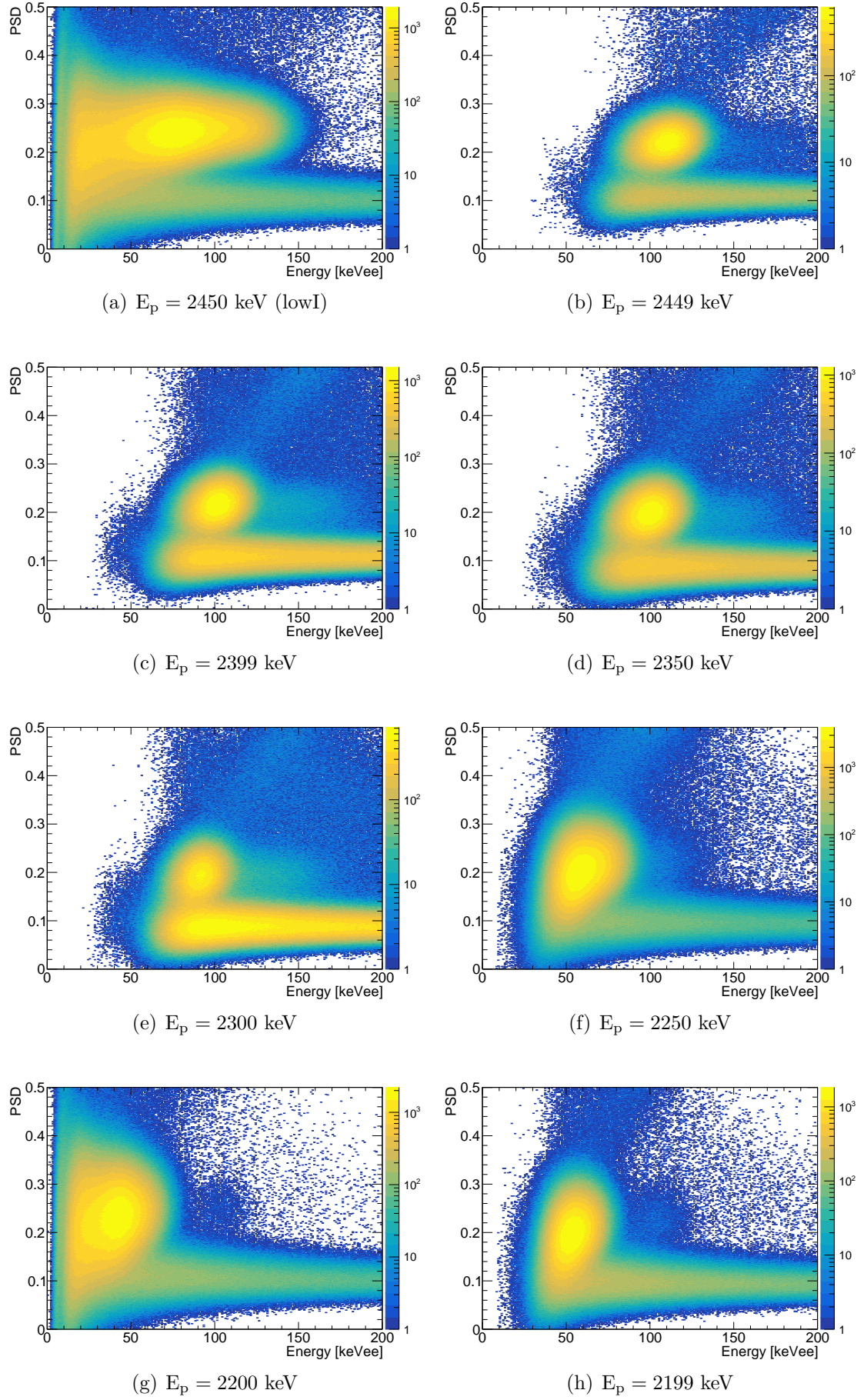
Figure 5.6: EJ-309 scintillator neutron/γ PSD performance using neutron beam optimized gates parameters.

(i) $E_p = 2150$ keV

(j) $E_p = 2099$ keV

(k) $E_p = 2050$ keV

(l) $E_p = 2000$ keV

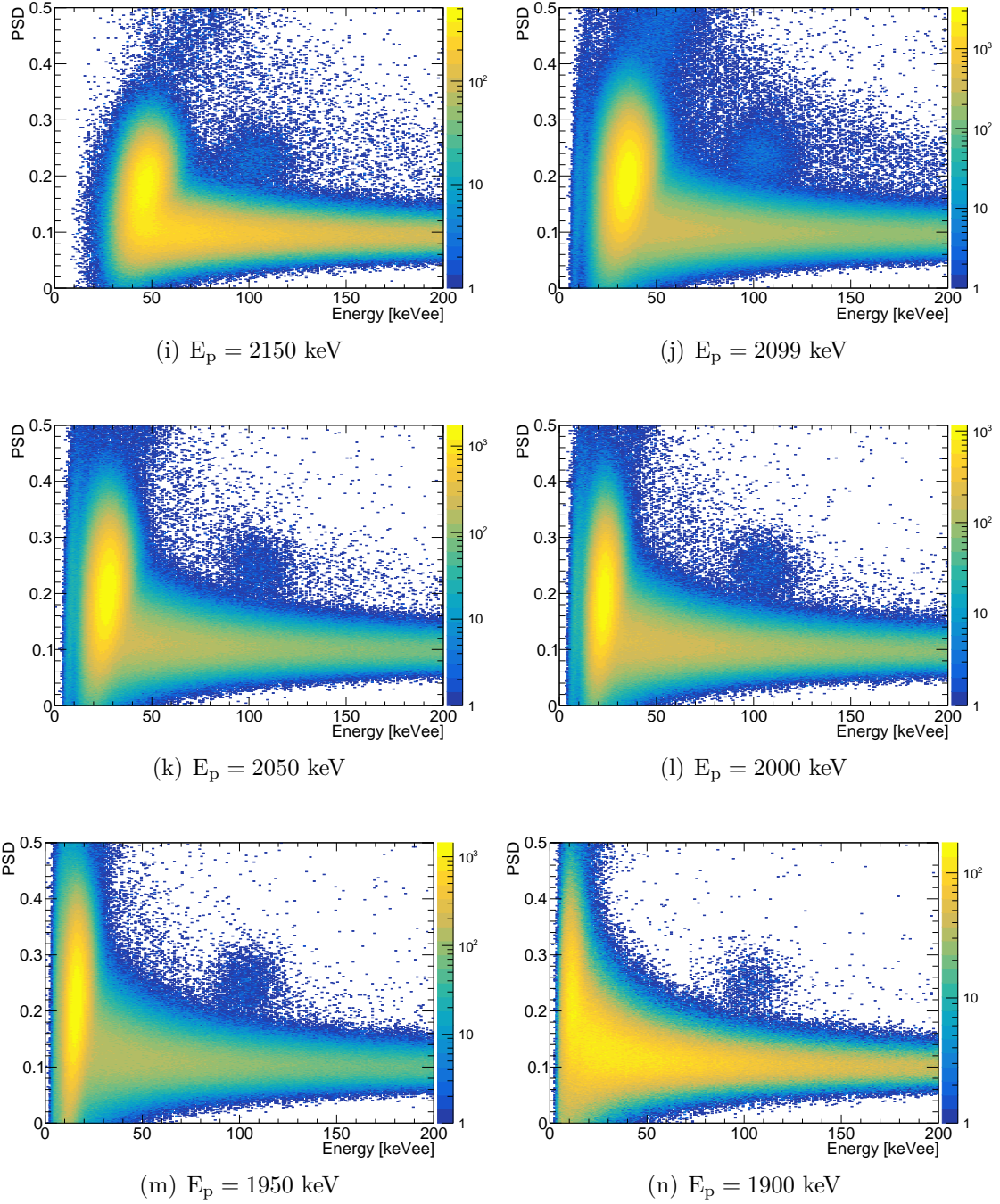(m) $E_p = 1950$ keV

(n) $E_p = 1900$ keV

Figure 5.6: EJ-309 scintillator neutron/γ PSD performance using neutron beam optimised gates parameters.
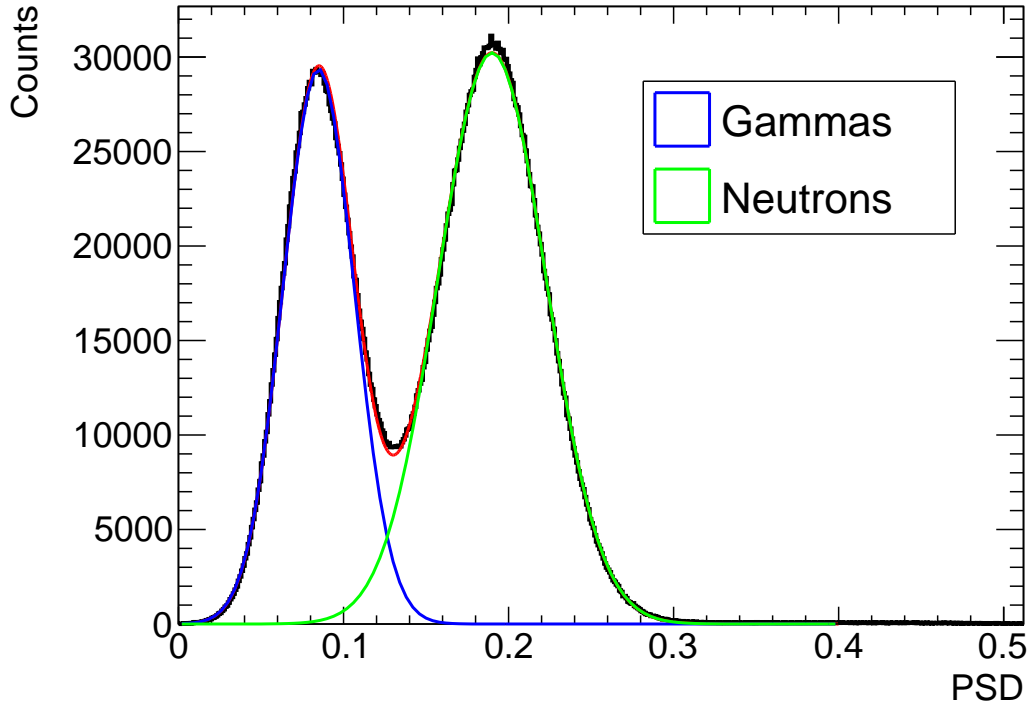
Figure 5.7: Estimation of the number of neutron and γ events in the scintillator. In black is the PSD parameter distribution with an energy < 150 keVee for neutron beam measurement at E_p = 2400 keV. The red line is the fit result using a sum of two Gaussian and in respectively green and blue the resulting distributions associated with neutrons and γ events.

measurement uncertainty, and/or to -most probably- time and usage degradation. For those reasons, the simulation is repeated for all significant energies varying those two quantities (i.e. Distance to target and target thickness). For this latter quantity, a 10% variation is investigated (2.8 and 3.4 µm). In both cases, the results show a 1 to 2 keV difference compared to the reference values. Even though those may also be due to the Monte-Carlo nature of the simulation, this uncertainty is associated with the value of E_n when establishing the energy calibration.

The neutron energy calibration is accomplished by matching each value of E_n to the mean value of the corresponding experimental neutron beam distribution. This latter is obtained fitting the region of interest in the spectra shown in Figure 5.6 with a bi-dimensional Gaussian function covering distinguishable neutron events having a PSD > 0.15 and an energy coverage of > 95% of the distribution. The FWMH of its projection on the energy axis is associated with the central energy value as a confidence bound. The fit performed this way rather than using a 1-dimensional Gaussian distribution contributed to better assessing the neutron region in lower energy runs where the γ/neutron separation is less pronounced. This approach indirectly implies that the waveform produced by each neutron event is assumed to result from total energy deposition. Even though neutrons do scatter multiple times before losing 100% of their energy, the performed simulation shows that the majority are thermalized within a time window compatible with the width of the produced ADC signals at the corresponding energy (see Figure 5.10). In any case, the considered neutron signature region in the PSD vs Energy spectra does only contain
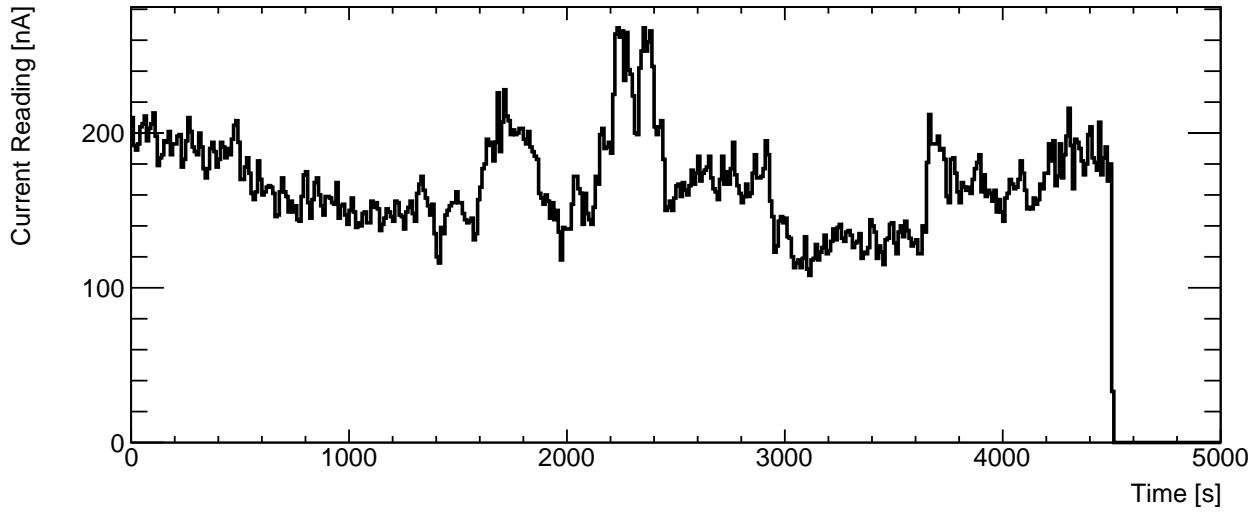
(a)
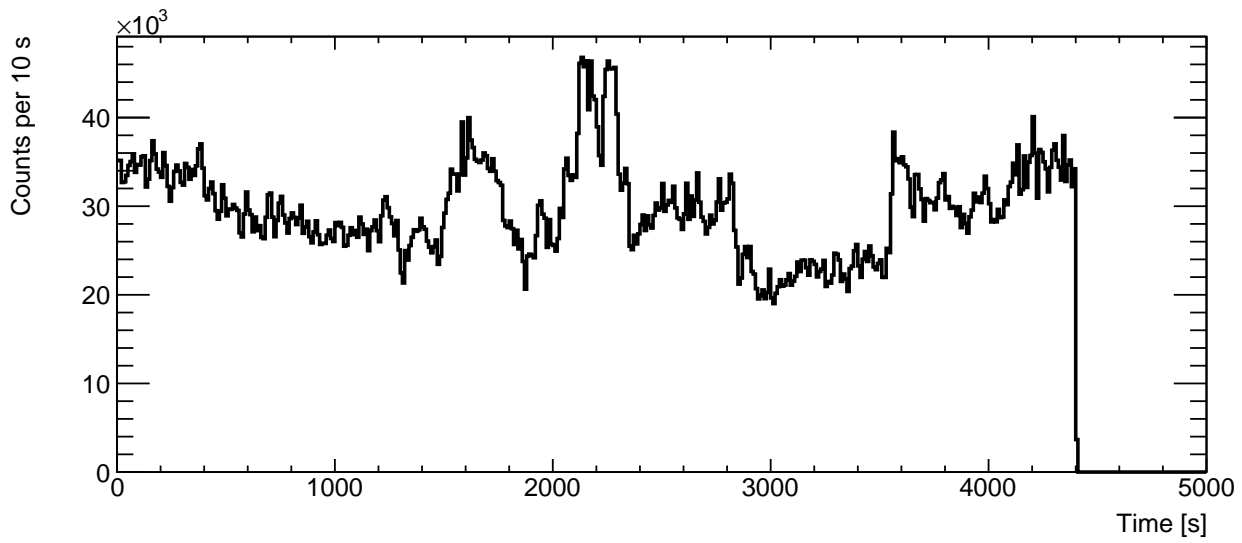
(b)
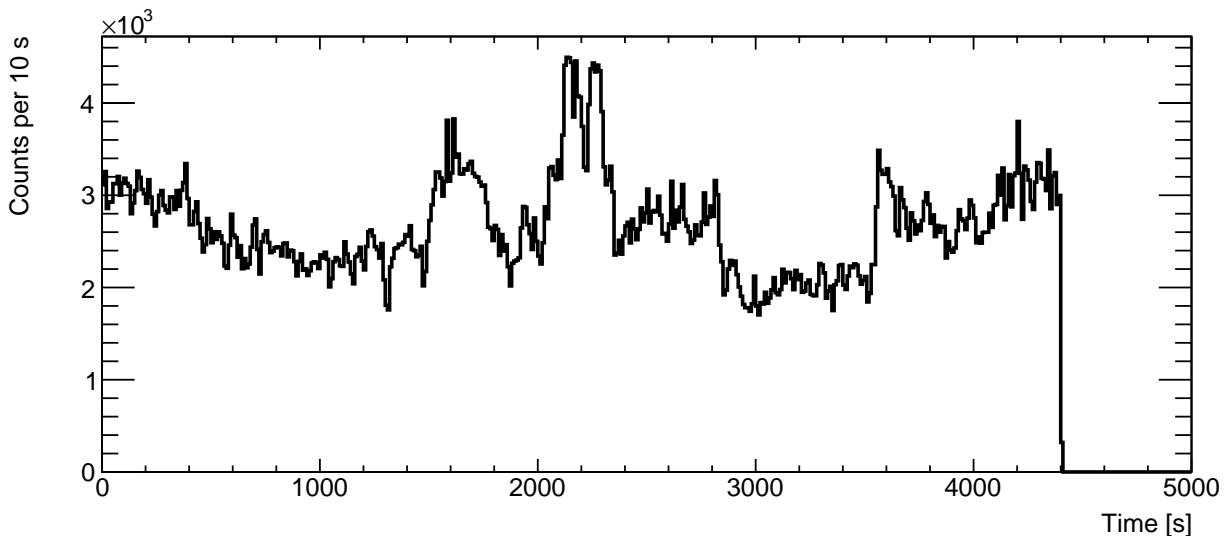
(c)

Figure 5.8: Measured neutron rate dependency on the beam current. In panel (a) is the VdG experimental beam current reading. In panel (b) is the incoming neutron flux from all ^{3}He counters. In panel (c) is the measured neutron flux in the EJ-309 scintillator. Data from run at proton beam energy E_p = 2449 keV.

Table 5.3: Average neutron energy produced by each measured proton beam energy.

E_p [keV]	E_n [keV]
1900	51
1949	139
1999	210
2050	272
2099	332
2150	391
2198	448
2249	504
2299	557
2350	610
2399	664
2449	717

events where the neutron multiple scatterings signals overlap forming a waveform single peak. When those latter are well-distinct, the PSD value increases shifting those events up-right in the aforementioned spectra and therefore not considered when determining the centroid.

(a)   (b)
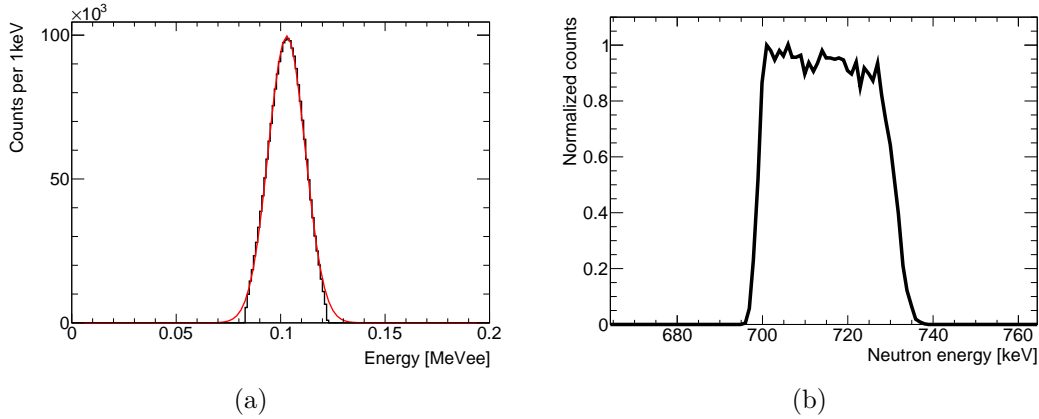
Figure 5.9: In Panel (a) is the neutron energy spectrum from the EJ-309 liquid scintillator corresponding to the run using the proton beam at E_p = 2450 keV.. Data obtained by selecting events within 2σ around the center of the corresponding region. In red is a fit of the energy spectrum using a Gaussian distribution. In panel(b) is the simulated neutron energy spectrum reaching the liquid scintillator. Data from PINO using a proton beam of the same energy.

The neutron energy to electron equivalent light output correspondence is fitted using 3 different parametrization models that were proven to work on higher neutron energies: a rational of a polynomial [110], an exponential [111][110] and a quadratic function defined as follows :

Rational of a polynomial

$$E(E_n) = P_0 \cdot \frac{E_n^2}{E_n + P_1} \tag{5.5.1}$$
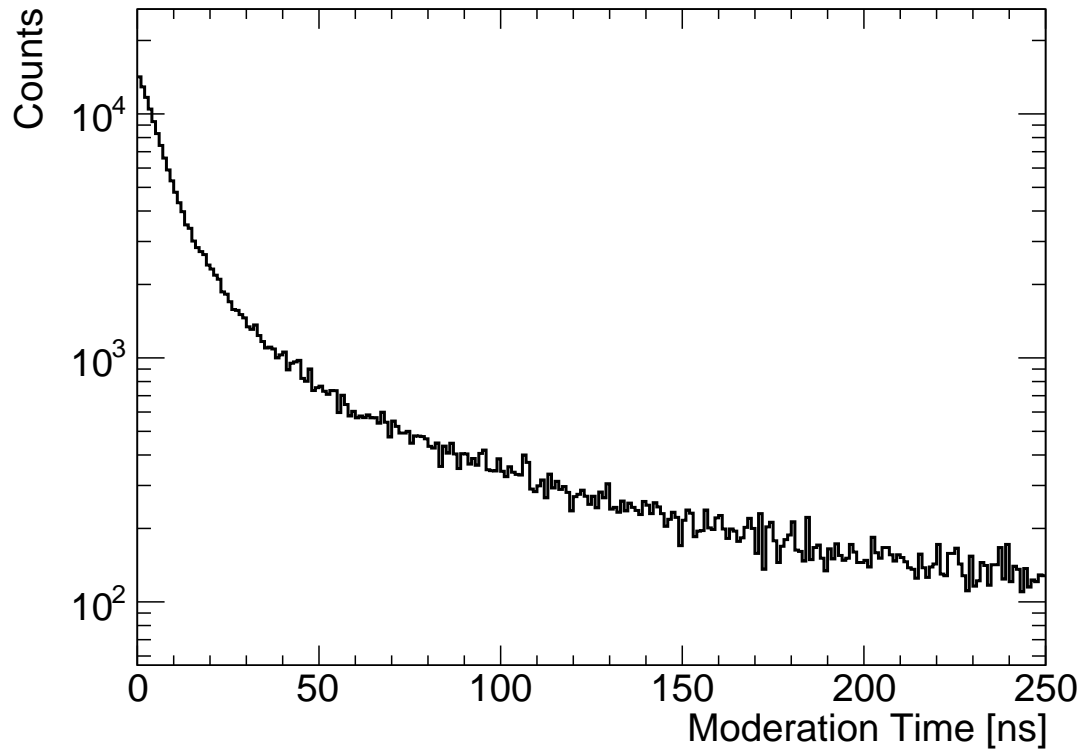
(a)
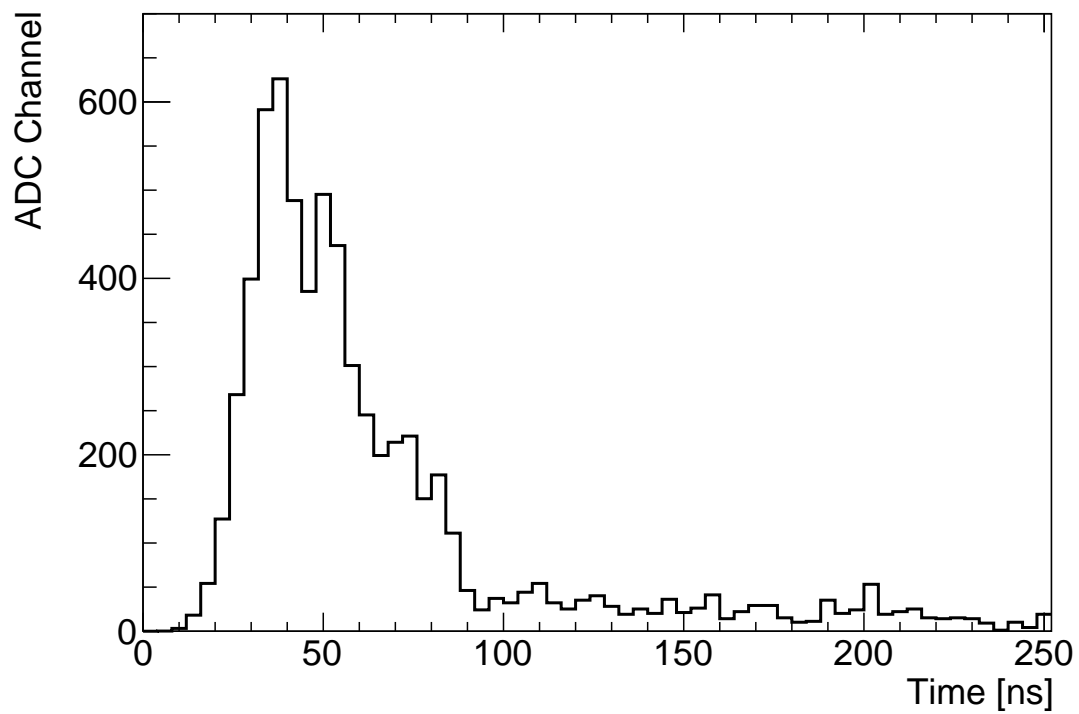
(b)

Figure 5.10: Comparison between expected neutron moderation time and the neutron pulse width produced by the DAQ. In panel (a) is the simulated 714 keV neutrons moderation time in EJ-309 liquid scintillator. In panel (b) is a typical waveform for neutrons of the same energy.

Exponential

$$E(E_n) = P_0 \cdot E_n - P_1 \cdot [1 - e^{-P_2 \cdot E_n^{P_3}}] \tag{5.5.2}$$

Quadratic

$$E(E_n) = P_0 \cdot E_n^2 + P_1 \cdot E_n + P_2 \tag{5.5.3}$$

The results of the fits performed using this work's data as well as others found in the literature[112][113] are plotted in Figure 5.11. As for the α-particles, the quadratic quenching effectively reproduces the observed trend. The same can also be stated about the exponential and rational polynomial models, especially since the confidence margin is considered within 1σ of the light output distribution. It is also demonstrated in the *Norsworthy et al.* article[114] that most extrapolations of literature fit models diverge at lower energies because of the experimental data lack, thus the importance of this work focusing on the < 1 MeV region relevant for the ^{22}Ne(α,n)^{25}Mg measurement.

Table 5.4: Neutron energy calibration fit parameters for light output taken in MeVee and neutron energy in MeV.

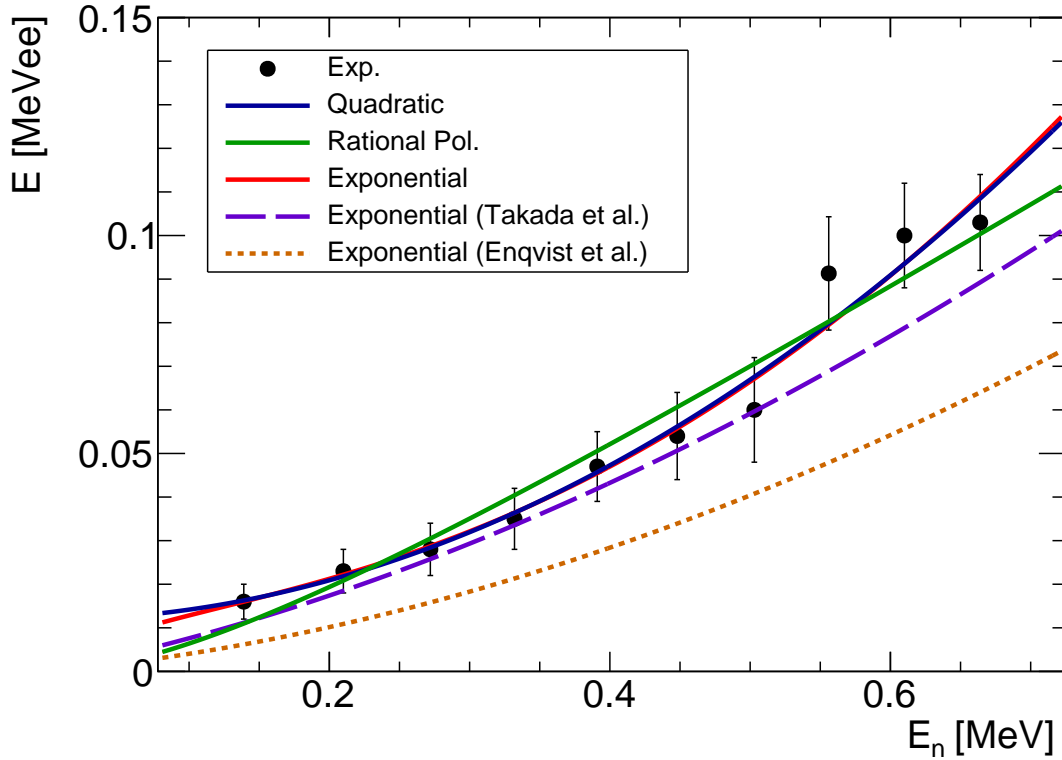|	P_0	P_1	P_2	P_3
Rational	2.0×10^{-1}	2.1×10^{-1}	/	/
Quadratic	2.2×10^{-1}	2.6×10^{-3}	1.2×10^{-2}	/
Exponential	1.3×10^{0}	2.5×10^{0}	5.7×10^{-1}	1.0×10^{0}

Figure 5.11: Different fit models applied on the low energy neutron calibration experimental data compared to that of Takada et al. [113] and Enqvist et al. [112].
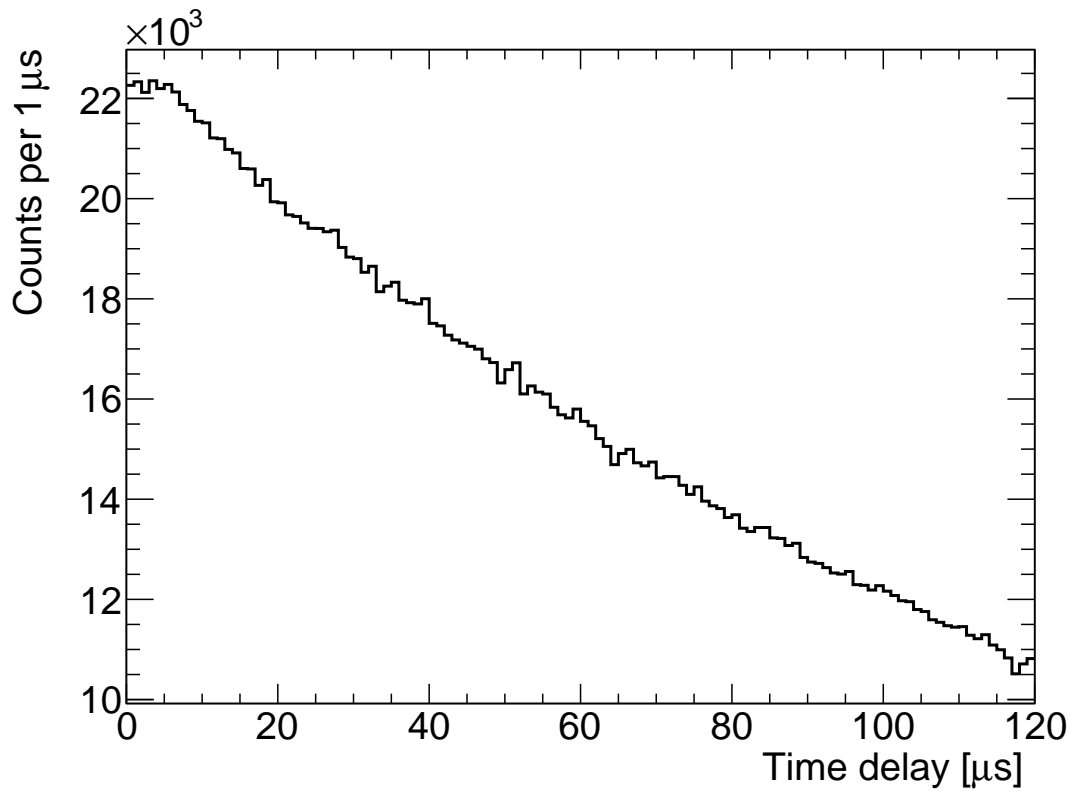
5.6 Scintillator-^{3}He time coincidence

The measurement performed at the Goethe University of Frankfurt discussed in this chapter does also serve to test the filtering capabilities of the setup through time coincidence/anti-coincidence analysis. The origin of neutrons detected in the ^{3}He counters can be identified using this method, thus helping to discard those not resulting from the ^{22}Ne(α,n)^{25}Mg nuclear reaction for the SHADES experiment. The experimental setup used for the direct neutron beam measurement, which is a simplified version of the SHADES full setup, allows such time delay analysis thanks to the available timestamp information for each detected event. Combining this information with that of PSD, it is possible to investigate possible correlations between neutrons and γ-rays identified in the scintillators and those measured in the ^{3}He counters. Further efficiencies such as that of neutron detection in EJ-309 and Scintillator-^{3}He coincidence can also be assessed using the resulting information as discussed in Section 5.4.

Monte-Carlo simulation reproducing the behavior of sub 1 MeV neutrons in EJ-309 scintillating liquid shows that almost all their energy is lost within a few hundred nanoseconds (see Figure 5.10). The resulting thermal neutrons then escape the scintillator's geometry and might be absorbed inside one of the surrounding ^{3}He proportional counters. Even though thermal neutrons velocity is $\simeq 2.2 \times 10^3$ m.s^{-1}, the traveling time from the scintillator to one of the counters cannot be directly calculated. This is because neutrons continue scattering at an even greater pace, making it very unlikely to travel following a straight path between the two detector types. The distribution of this quantity (i.e. travel or delay time) can, nevertheless, be assessed by constructing a coincidence algorithm. It is here set to sequentially read the detected events from the gathered experimental data in a reverse time order gating on the ^{3}He proportional counters. This means that when an event from one of them (i.e ^{3}He counters) is encountered, it verifies that the direct preceding entry is a neutron event from the EJ-309 scintillator and then calculates Δt, the time delay between the two events. Neutron events are defined similarly as discussed in Section 5.5 (i.e. within 2σ of the bi-dimensional Gaussian function used to fit the Energy-PSD spectrum). The obtained values are then used to fill 1µs bin width histograms such as in Subfigure 5.12(a). For comparison, another variation of the same coincidence procedure is investigated: Performing coincidences between neutrons in the counters and γ-events in the scintillator to reproduce the expected behavior from random coincidences. This latter produced a decay exponential-like shape that is expected from a randomly occurring phenomenon (see Subfigure 5.12(b)).

Independently from the selected neutron beam energy, the coincidence delay time spectra do always show a peak at around 4 to 5 µs, a signature that is absent in the case of purely random coincidences (see Figure 5.12). Further investigation using the same data showed that this peak becomes more distinguishable from the exponential background when constraining the coincidence to events that are mostly neutrons (i.e. around the neutron peak in the bi-dimensional PSD spectrum). This result supports that it is indeed due to thermalized neutrons reaching the counters. It is possible to double-check this assumption by plotting scintillator events that are gated by the ^{3}He counters within a Δt around the time delay peak (i.e. 3 to 9 µs). This procedure showed a clear change in the γ/neutrons counts ratio in the favor of latter quantity as can be seen in Figure 5.13). This result is however to only be taken
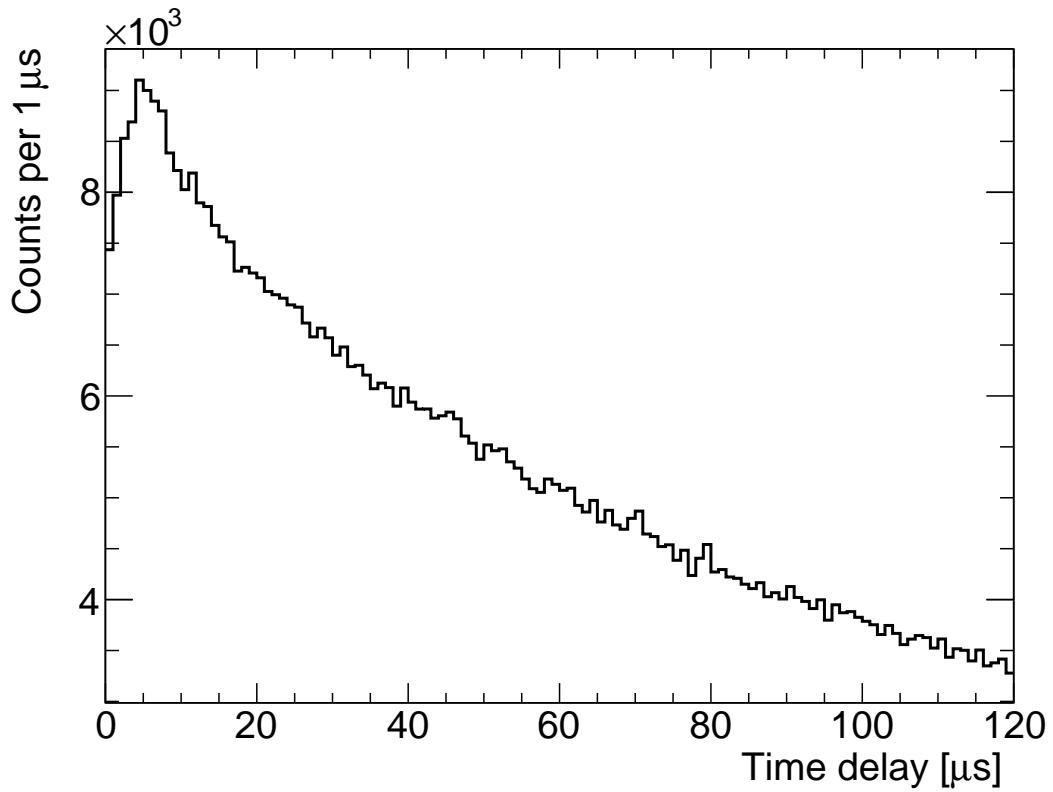
(a)

(b)

Figure 5.12: ^{3}He gated coincidence time spectra with events from the EJ-309 liquid scintillator. In panel (a) is that of ^{3}He neutron events with all EJ-309 events < 150 keVee (γ + neutron). In panel (b) is that of ^{3}He neutron events with only EJ309 γ events. This latter is assumed to reproduce the shape of expected random coincidences.
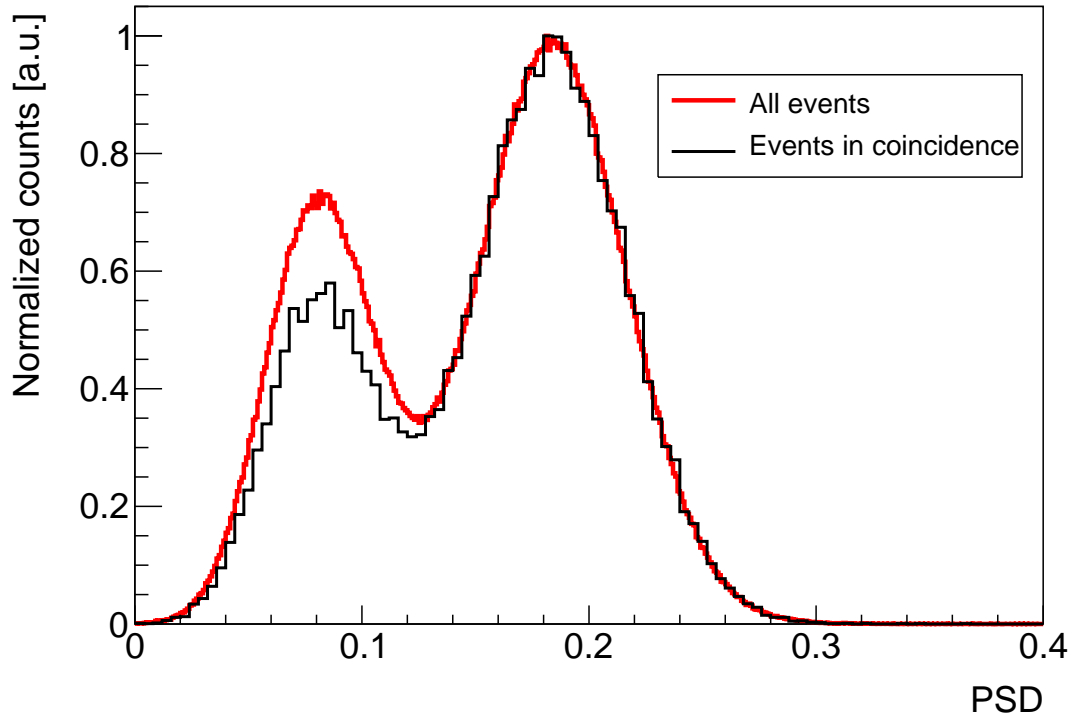
Figure 5.13: γ-to-neutron events ratio evolution in the EJ-309 scintillator using optimized delay time information from the coincidence analysis for the measurement at $E_p = 2350$ keV. In red is the PSD distribution of all events under 100 keVee and in black that of events validated by a ^{3}He counters with a ΔT between 3 to 9 μs. Count number normalized to the neutron peak.

qualitatively since it is achieved at the high cost of more than 97% of the statistics being lost because of the very short integration time window that is considered. Similarly, the coincidence procedure impact on the ^{3}He counters spectra can be noticed for gated events. All events in coincidence are here considered, not only those within a certain delay time window, and a clear suppression of events in the γ-region is also noticed (see Figure 5.14). This last result represents further evidence that the filtering is able to achieve neutron/γ discrimination while the impact on the global statistics is still minimal with an overall reduction of only around 54%. It is of course not possible to apply the same procedure for the bi-dimensional PSD spectrum is the events rate in the scintillator is often much higher than in the counters, increasing the probability of random coincidences.

Filtering efficiency

The main purpose of the liquid scintillators in the SHADES experiment is to act as a moderator, increasing the number of neutrons detected by the counters due to their higher cross-section at lower energy. A precise estimate of their neutron detection efficiency is therefore not mandatory to assess the targeted experiment. This quantity is anyway not possible to estimate using the available data. This is due to the minimum detection threshold being set at high ADC values during certain measurement runs, thus cutting a large part of the neutron beam statistics as can be seen in Subfigure 5.17(a). Exploiting the same data from measurements performed in Frankfurt, another feature that is possible to investigate is the ^{3}He-
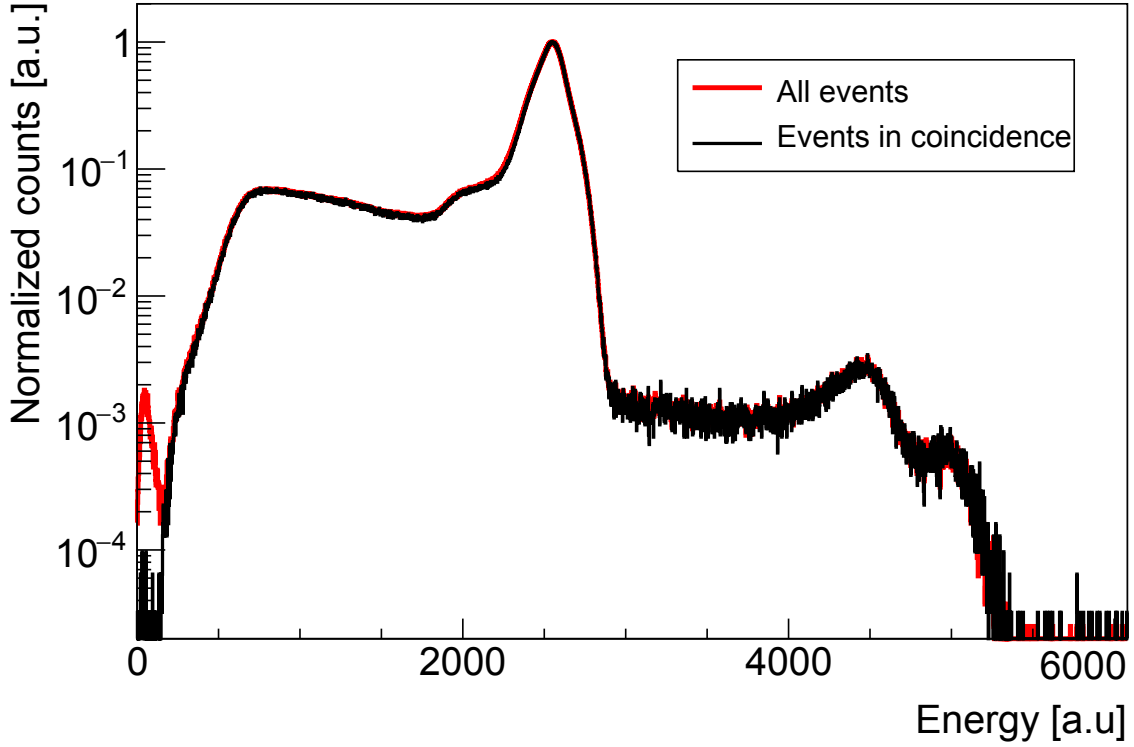
Figure 5.14: Uncalibrated ^{3}He counters energy spectrum evolution. In red is the full distribution containing all events from all counters. In black are only represented events in coincidence with scintillator events. The count number is normalized to the full energy deposition peak.

EJ309 coincidence efficiency. This refers to the amount of neutrons registered in the scintillator that is scattered back to one of the counters. A quantity directly linked to the geometrical coverage of the ^{3}He around the scintillator. An acceptable estimation of its value is obtained by scaling the angular coverage of 1 counter considering the point from the central axis of the EJ-309 liquid scintillator that is equidistant from the ^{3}He counter's top and bottom edges (see Figure 5.15). An approximation of the geometrical coincidence efficiency is then assumed to be 6 times the product of the covered angles ratio of one counter in the xy and xz planes, as follows :

$$\epsilon_{\text{geo}} = 6 \times \frac{103.14°}{360°} \times \frac{14.55°}{360°} \simeq 7\% \tag{5.6.1}$$

The array's experimental neutron coincidence efficiency is the number of neutrons that are thermalized in the scintillator and then captured by one of the ^{3}He counters. An intuitive way to quantify the number of neutrons in coincidence with less uncertainties is by subtracting the random coincidences from the total coincidence time delay spectrum. A distribution is built considering the Δt of all events from the scintillator regardless of their particle type. Conversely, the γ/neutron coincidences spectrum (see Subfigure 5.12(b)) reproduces the behavior of random coincidences. It is scaled to the total coincidence spectrum to represent the number of random coincidences due to both γ and environmental/delayed neutron events. The scaling factor is obtained through a fit of the random coincidence distribution to that of total coincidences at higher delay time values. Indeed, events with a Δt > 500 ns are assumed to be mostly random coincidences, and the difference between
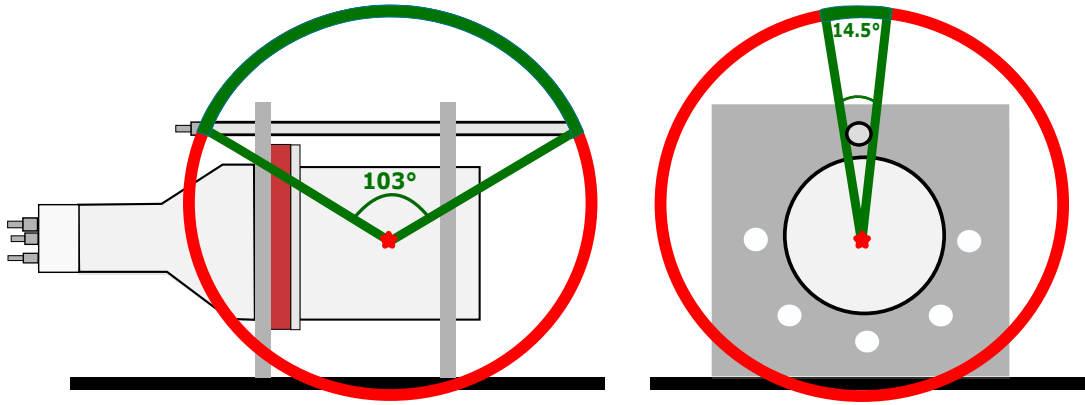
Figure 5.15: Average angular coverage achieved by $1 \times {}^3$He counter on a point within the EJ-309 organic liquid cell. The side view (left) is parallel to the xz plane and the front view (right) is parallel to the xy plane.

the two spectra is therefore representing the number of neutron coincidences between the two types of detectors free from the contribution of random coincidences (see Figure 5.16). For example, the run performed at $E_p = 1900$ keV is very close to the ^{7}Li(p,n)^{7}Be threshold. Relatively few neutrons are generated and therefore most coincidences are random. Nevertheless, the coincidence procedure can still quantify the number of good neutron events (i.e. thermalized by the scintillator and then captured by a counter) as can be seen in Subfigure 5.16(a) providing further support for the previous assumption. The procedure is repeated for all beam energies using 3 different time delay ranges 500 - 4000 ns, 750 - 4000 ns, and 1000 - 4000 ns. This allows the extraction of an uncertainty around the central value obtained fitting at 750 ns. Table 5.5 reports the obtained number of counts in each case. The average coincidence efficiency is then calculated by fitting the values from runs where the threshold includes most of the neutron beam statistics (see Figure 5.18). The resulting average coincidence efficiency obtained is about 7±1 %, which is similar to the previously approximated geometrical efficiency of the EJ-309 thermalized neutrons detection by a ^{3}He, and therefore retrieving the ∼100% thermal neutron detection efficiency of ^{3}He proportional counters [115]. This last result can be considered as proof that time coincidence filtering as performed in this work can identify and quantify the amount of neutrons moderated by the scintillator increasing the SHADES full setup neutron detection efficiency during the ^{22}Ne(α,n)^{25}Mg measurement campaigns. The obtained information about the energy deposited by individual neutron events will also give a hint about its origin allowing the exclusion of α-induced reactions from possible contaminant present in the beam-line (see Table 2.1).
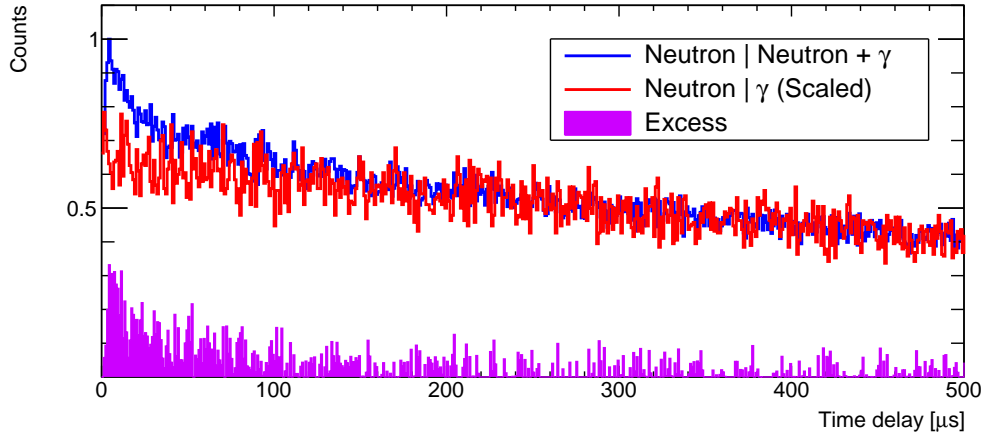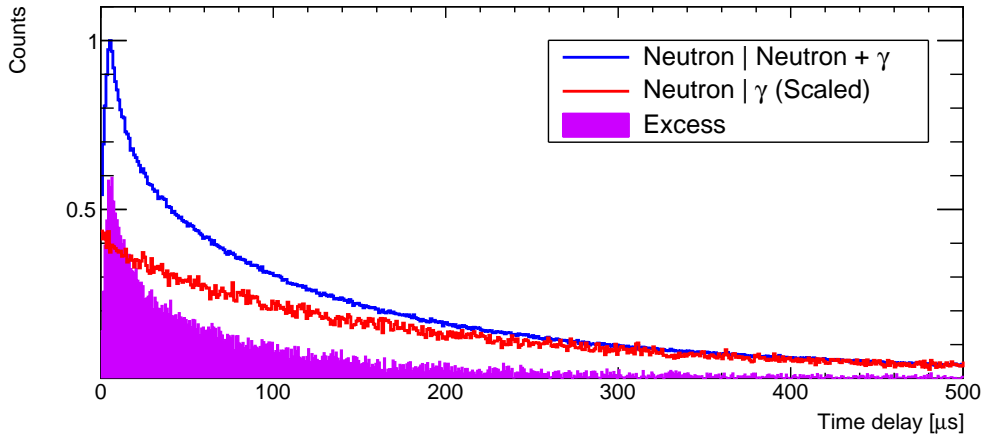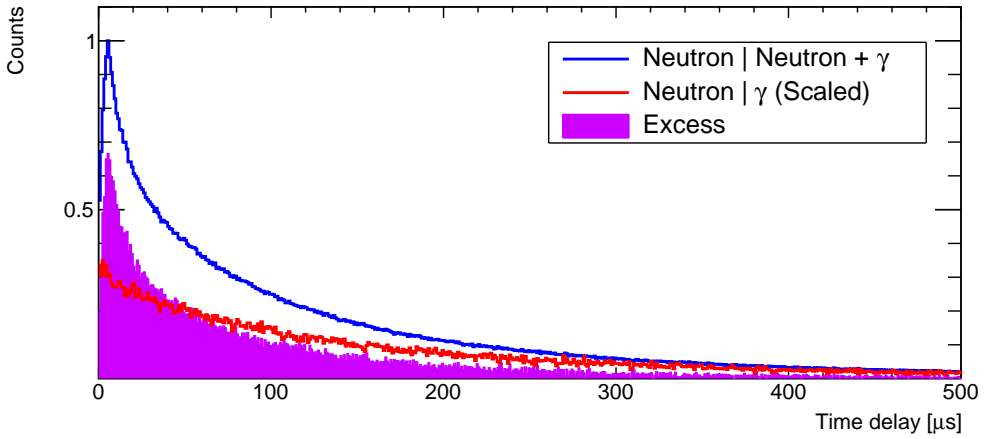
Figure 5.16: Normalized time delay spectra of neutron events in coincidence between the EJ-309 liquid scintillator and the ^{3}He counters obtained at E_{p} = 1900 keV in panel (a), at 2000 keV in panel (b), and at 2450 keV in panel (c). In blue is the total Δt distribution of coincidence events between a neutron from a ^{3}He counter and any event from the scintillator (i.e. both neutron and γ events). In red is the Δt distribution of ^{3}He neutron events in coincidence with a γ from the scintillator representing random coincidences, scaled to fit the total distribution. The purple distribution is the excess above the random distribution model representing the neutron events thermalized by the scintillator then captured by one of the ^{3}He counters.
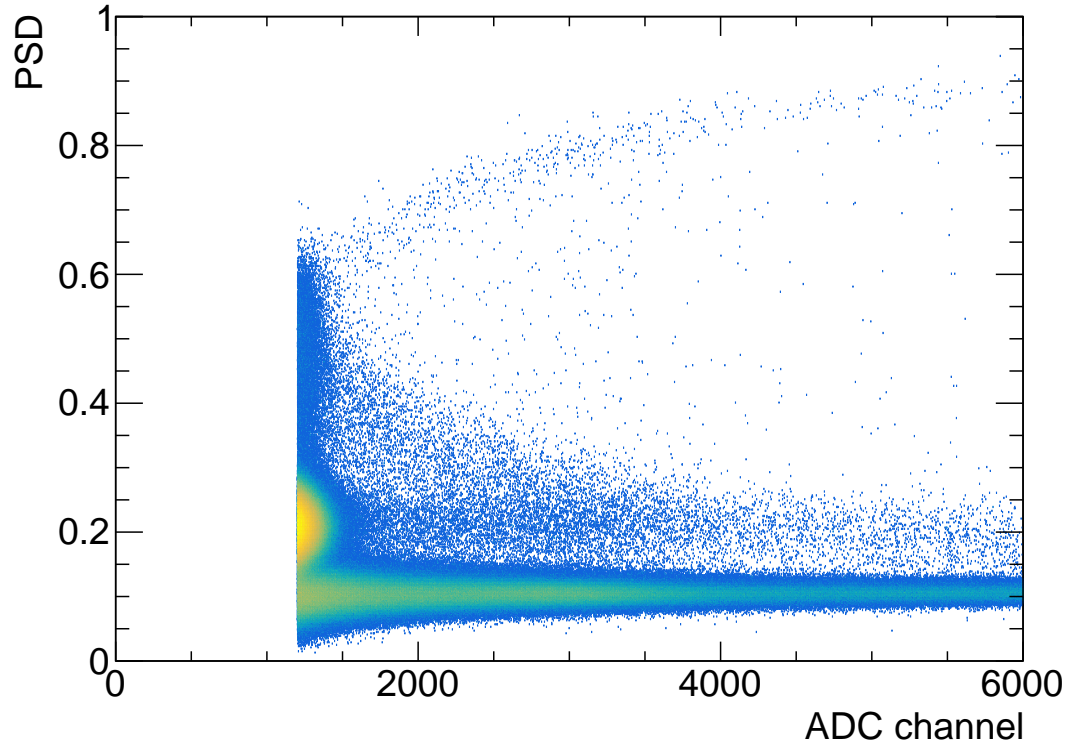
(a)
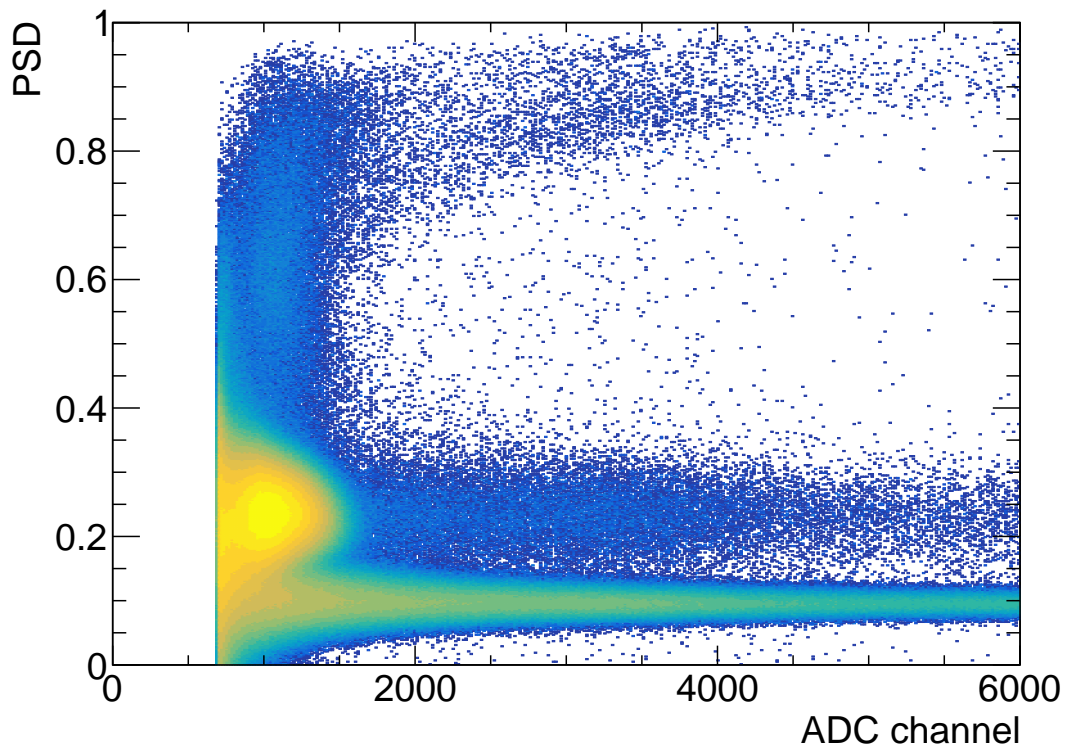
(b)

Figure 5.17: PSD vs ADC channel bi-dimensional spectra comparison between the two runs conducted with a proton beam of E_p = 2450 keV using different current and DAQ low energy threshold values. In panel (a) targeting a 200 µA current with a cut at ADC channel 1200 and in panel (b) targeting a 35 µA current with a threshold cut at ADC channel 690.
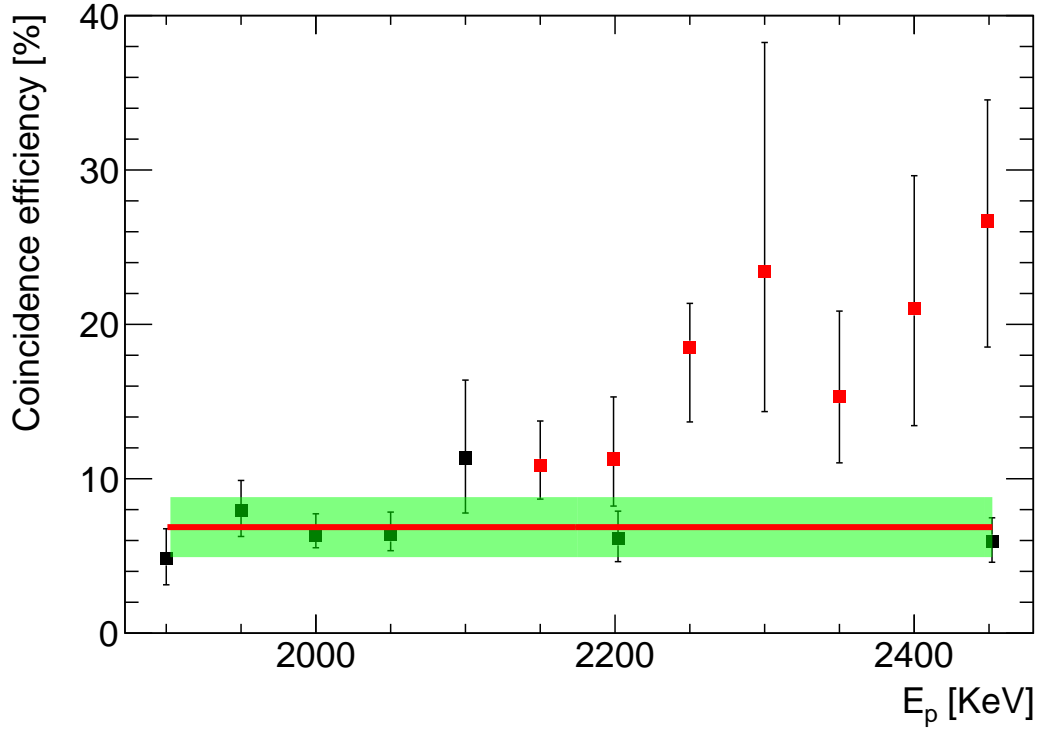
Figure 5.18: Coincidence efficiency of the Frankfurt Array estimated for each proton beam energy E_p. The ratio shown in the Y-axis represents the number of thermalized neutron events identified by coincidence analysis over the number of neutrons registered in the EJ-309 liquid scintillator. The red line represents the average efficiency value of data points in black corresponding to low threshold measurements and its uncertainty is represented through the green band. Data points shown in red are not considered in the fit procedure since they belong to measurement runs with an inadequate ADC channel minimum threshold preventing the estimation of the number of neutrons registered in the scintillator such as in Subfigure 5.17(a).

Table 5.5: Count number of neutron events in coincidence obtained fitting the random delay time distribution to the total coincidence spectrum at different Δt ranges.

	Fit range [ns]		
E_p[keV]	500 - 4000	750 - 4000	1000 - 4000
1950	2.01×10^5	2.54×10^5	3.17×10^5
2000	1.34×10^5	1.54×10^5	1.86×10^5
2050	2.17×10^5	2.59×10^5	3.19×10^5
2099	5.60×10^5	8.16×10^5	1.18×10^6
2150	6.77×10^4	8.48×10^4	1.07×10^5
2198	3.54×10^5	4.84×10^5	6.58×10^5
2200	4.61×10^5	6.08×10^5	7.86×10^5
2250	1.43×10^6	1.93×10^6	2.23×10^6
2300	1.65×10^5	2.69×10^5	4.39×10^5
2350	1.33×10^5	1.84×10^5	2.51×10^5
2399	1.31×10^5	2.04×10^5	2.88×10^5
2449	3.66×10^4	5.27×10^4	6.82×10^4
2450	5.91×10^5	7.68×10^5	9.63×10^5

Conclusion

A full characterization of EJ-309 organic liquid scintillator detectors is performed and discussed in this thesis. Their triple use in the SHADES detection array for neutron moderation medium, energy reconstruction, and coincidence filtering alongside ^{3}He proportional counters makes them a powerful experimental tool for investigating the astrophysically relevant ^{22}Ne(α,n)^{25}Mg nuclear cross-section. This reaction represents the main source of neutron production in massive stars that feeds the weak component of the s process, allowing the nucleosynthesis of intermediate-mass elements (A = $\sim$60 - 90). ^{22}Ne(α,n)^{25}Mg is also an important neutron source of the main component of the s process alongside ^{13}C(α,n)^{16}O. The main s process exclusively takes place during the helium shell explosive flash in AGB stars, producing elements of an atomic mass A = $\sim$90 - 209. The origin of the two s process components as well as the stellar environment in which they are found are discussed in more detail in the 1st chapter of this work. The main technical challenge regarding the measurement of ^{22}Ne(α,n)^{25}Mg is its low cross-section leading to a neutron production that is much below the environmental neutron background. The SHADES experiment novelty is the conduction of the measurement in a deep-underground environment (LNGS - Italy) where the neutron flux is up to 3 orders of magnitude lower than on surface laboratories in which previous attempts to measure the reaction took place. This is added to its experimental setup hybrid design taking advantage of two different types of detectors to achieve further background suppression as demonstrated in this work.

After having discussed theoretical and experimental concepts of nuclear reactions study that are relevant to the aim of this work, ^{3}He proportional counters and EJ-309 scintillators design and functioning principles are discussed in the 2nd. The 3rd chapter reports the details of the characterization work done on these latter beginning from performing a gain match of each one of the 13 units with the rest of the array. This latter procedure allowed the investigation and then the establishment of optimal DAQ parameters to use for upcoming measurements involving the same scintillators. An adequate γ-energy calibration is then established using data from ^{60}Co and ^{137}Cs radioactive sources measurements conducted in the Nuclear Astrophysics laboratory of the University of Naples "Federico II" with an EJ-309 scintillator placed inside a thick lead shielding. Several Pulse Shape Discrimination methods were then tested and optimized for the scintillators leading to the selection of charge integration as a main PSD technique for future data analysis. The second part of the characterization -discussed in the 4th chapter- took place in the deep-underground laboratory of Gran Sasso (AQ) where PSD analysis of one-month-long background acquisition using the liquid scintillators shielded by a lead castle allowed the discovery and quantification of their internal α-activity that averaged $\sim$64 cph. This latter is due to ^{238}U and ^{232}Th presence in the aluminum housing surrounding the EJ-309 liquid cell of the detectors. A model using Monte-Carlo simulation has

been constructed allowing the quantification of each isotope concentration in the aluminum, resulting in respectively $8.4(1.8)_{sta}(1.4)_{sys} \times 10^{-2}$ and $1.62(0.57)_{sta}(0.03)_{sys} \times 10^{-1}$ ppm. Time coincidence analysis between events from the α and γ (or β⁻) PSD peaks allowed the estimation of a new ^{214}Po isotope half-life value that is $163.7(1.1)$ µs. Results from both ^{238}U and ^{232}Th concentrations, and ^{214}Po half-life have been published in a scientific article [93].

The investigation done on the setup response to neutrons is discussed in the 5th chapter. A reduced version of the SHADES detection array consisting of 1 EJ-309 scintillator surrounded by 6 ^{3}He counters is built and exposed to a direct neutron beam at different energies. This later is produced through the ^{7}Li(p, n)^{7}Be nuclear reaction by a proton beam from the Goethe University of Frankfurt Van De Graaff accelerator hitting a thin ^{7}Li target. New PSD parameters are then generated for the measured data in such a way as to maximize γ/neutron separation at low neutron energies. The neutron region of scintillator spectra obtained at each energy was then isolated and matched with the average neutron energy produced by the ^{7}Li. This latter step led to the establishment of a neutron energy calibration that is adapted for the energy region of interest ($E_n < 1$ MeV). The last part of the work performed in the framework of this thesis consists of the construction of an events-filtering algorithm based on time coincidence between the two types of detectors composing the setup. Indeed, taking advantage of its hybrid design, it is possible to discard neutron events that do not directly originate from the ^{22}Ne(α,n)^{25}Mg reaction during the final measurement. The time coincidence ^{3}He-EJ-309 filtered was tested using the experimental data from the Frankfurt measurement. It led to the discovery of a neutron signature in the time delay spectra. A specific analysis procedure is then conceived to take advantage of it, allowing the quantification of the amount of neutrons thermalized by the scintillator and therefore the filtering capabilities of the array.

Bibliography

[1] H. A. Bethe et al. "The Formation of Deuterons by Proton Combination". In: *Phys. Rev.* 54 (4 Aug. 1938), pp. 248–254. DOI: `10.1103/PhysRev.54.248`.

[2] E. M. Burbidge et al. "Synthesis of the Elements in Stars". In: *Rev. Mod. Phys.* 29 (4 Oct. 1957), pp. 547–650. DOI: `10.1103/RevModPhys.29.547`.

[3] A. G. W. Cameron. "New Neutron Sources of Possible Astrophysical Importance." In: *Astronomical Journal* 65 (Jan. 1960), p. 485. DOI: `10.1086/108085`.

[4] M. Goeppert-Mayer. "The Shell Model". In: *Science* 145.3636 (Sept. 1964), pp. 999–1006. DOI: `10.1126/science.145.3636.999`.

[5] C. Ananna et al. "The SHADES neutron detection array". In: *EPJ Web Conf.* 260 (2022), p. 11043. DOI: `10.1051/epjconf/202226011043`.

[6] P. Prati and on behalf of the LUNA Collaboration. "The LUNA-MV facility at Gran Sasso". In: *Journal of Physics: Conference Series* 1342.1 (Jan. 2020), p. 012088. DOI: `10.1088/1742-6596/1342/1/012088`.

[7] C. Hayashi et al. "Evolution of the Stars". In: *Progress of Theoretical Physics Supplement* 22 (Feb. 1962), pp. 1–183. ISSN: 0375-9687. DOI: `10.1143/PTPS.22.1`.

[8] C. Hayashi. "Evolution of Protostars". In: *Annual Review of Astronomy and Astrophysics* 4.1 (1966), pp. 171–192. DOI: `10.1146/annurev.aa.04.090166.001131`.

[9] J. Iben Icko. "Stellar Evolution. I. The Approach to the Main Sequence." In: *Astrophysical Journal* 141 (Apr. 1965), p. 993. DOI: `10.1086/148193`.

[10] J. Iben Icko. "Stellar Evolution. VII. The Evolution of a 2.25 M{sun} Star from the Main Sequence to the Helium-Burning Phase". In: *Astrophysical Journal* 147 (Feb. 1967), p. 650. DOI: `10.1086/149041`.

[11] I. Iben. "Globular-Cluster Stars". In: *Scientific American* 223.1 (1970), pp. 26–39. ISSN: 00368733, 19467087. URL: `http://www.jstor.org/stable/24925847` (visited on 09/25/2023).

[12] N. Prantzos. "Stellar nucleosynthesis and γ-ray line astronomy." In: *Astronomy and Astrophysics Supplement* 120 (Dec. 1996), pp. 303–310. URL: `https://ui.adsabs.harvard.edu/abs/1996A&AS..120C.303P`.

[13] F. X. Timmes. URL: `https://cococubed.com/images/net_ppcno/ppcno_sdot.pdf`.

[14] M. Busso et al. "Nucleosynthesis in Asymptotic Giant Branch Stars: Relevance for Galactic Enrichment and Solar System Formation". In: *Annual Review of Astronomy and Astrophysics* 37.1 (1999), pp. 239–309. DOI: `10.1146/annurev.astro.37.1.239`.

[15] M. Schwarzschild et al. "Red Giants of Population II. II." In: *Astrophysical Journal* 136 (July 1962), p. 158. DOI: 10.1086/147361.

[16] W. Deinzer et al. "Models for carbon-burning stars". In: *Astrophysical Journal* 142 (1965), pp. 813–823. DOI: 10.1086/148355.

[17] C. Rolfs et al. *Cauldrons in the Cosmos: Nuclear Astrophysics*. Theoretical Astrophysics. University of Chicago Press, 1988. ISBN: 9780226724577. URL: https://ui.adsabs.harvard.edu/abs/1988ccna.book.....R.

[18] F. Hoyle et al. "Nucleosynthesis in Supernovae." In: *Astrophysical Journal* 132 (Nov. 1960), p. 565. DOI: 10.1086/146963.

[19] W. A. Fowler et al. "Neutrino Processes and Pair Formation in Massive Stars and Supernovae." In: *Astrophysical Journal Supplement* 9 (Dec. 1964), p. 201. DOI: 10.1086/190103.

[20] C. Iliadis. "Nuclear Physics of Stars". In: *Nuclear Physics of Stars*. John Wiley & Sons, Ltd, 2007. ISBN: 9783527618750. DOI: 10.1002/9783527618750.ch2.

[21] E. Anders et al. "Abundances of the elements: Meteoritic and solar". In: *Geochimica et Cosmochimica Acta* 53.1 (1989), pp. 197–214. ISSN: 0016-7037. DOI: https://doi.org/10.1016/0016-7037(89)90286-X.

[22] N. Prantzos et al. "Neutron Capture Nucleosynthesis during Core Helium Burning in Massive Stars". In: *Astrophysical Journal* 315 (Apr. 1987), p. 209. DOI: 10.1086/165125.

[23] D. D. Clayton et al. "Termination of the s-process". In: *Astrophysical Journal* 148 (Apr. 1967), p. 69. DOI: 10.1086/149128.

[24] J. G. Peters. "Nucleosynthesis by the s-process in Stars of 9 and 15 Solar Masses". In: *Astrophysical Journal* 154 (Oct. 1968), p. 225. DOI: 10.1086/149753.

[25] Y. Fenner et al. "The Chemical Evolution of Magnesium Isotopic Abundances in the Solar Neighbourhood". In: *Publications of the Astronomical Society of Australia* 20.4 (Jan. 2003), pp. 340–344. DOI: 10.1071/AS03042.

[26] E. Vassiliadis et al. "Evolution of Low- and Intermediate-Mass Stars to the End of the Asymptotic Giant Branch with Mass Loss". In: *Astrophysical Journal* 413 (Aug. 1993), p. 641. DOI: 10.1086/173033.

[27] F. Herwig. "Evolution of Asymptotic Giant Branch Stars". In: *Annual Review of Astronomy and Astrophysics* 43.1 (Sept. 2005), 435ˇ479. DOI: 10.1146/annurev.astro.43.072103.150600.

[28] O. Straniero et al. "s-process in low-mass asymptotic giant branch stars". In: *Nucl. Phys A* 777 (2006), p. 311. ISSN: 0375-9474. DOI: 10.1016/j.nuclphysa.2005.01.011.

[29] J. D. Cummings et al. "Initial-final mass relation for 3 to 4 $M_\odot$ progenitors of white dwarfs from the single cluster ngc 2099". In: *The Astrophysical Journal* 807.1 (July 2015), p. 90. DOI: 10.1088/0004-637X/807/1/90.

[30] K. Gesicki et al. "The mysterious age invariance of the planetary nebula luminosity function bright cut-off". In: *Nature Astronomy* 2 (June 2018), pp. 580–584. DOI: 10.1038/s41550-018-0453-9.

[31] R. Reifarth et al. "Neutron Reactions in Astrophysics". In: *Journal of Physics G: Nuclear and Particle Physics* 41 (Mar. 2014). DOI: 10.1088/0954-3899/41/5/053101.

[32] W. D. Arnett et al. "Carbon-Burning Nucleosynthesis at Constant Temperature". In: *Astrophysical Journal* 157 (July 1969), p. 339. DOI: 10.1086/150072.

[33] C. M. Raiteri et al. "S-Process Nucleosynthesis in Massive Stars and the Weak Component. I. Evolution and Neutron Captures in a 25 M$_{sun}$ Star". In: *Astrophysical Journal* 367 (Jan. 1991), p. 228. DOI: 10.1086/169622.

[34] M. Pignatari et al. "The Weak s-Process in Massive Stars and its Dependence on the Neutron Capture Cross Sections". In: *The Astrophysical Journal* 710 (Feb. 2010), p. 1557. DOI: 10.1088/0004-637X/710/2/1557.

[35] I. J. Sackmann et al. "The Creation of Superrich Lithium Giants". In: *Astrophysical Journal Letters* 392 (June 1992), p. L71. DOI: 10.1086/186428.

[36] J. Lattanzio et al. "Hot bottom burning in intermediate-mass stars". In: *Memorie della Società Astronomia Italiana* 67 (Jan. 1996), p. 729. URL: https://ui.adsabs.harvard.edu/abs/1996MmSAI..67..729L.

[37] D. Yong et al. "Magnesium Isotopic Abundance Ratios in Cool Stars". In: *The Astrophysical Journal* 599.2 (Dec. 2003), p. 1357. DOI: 10.1086/379369.

[38] D. Yong et al. "Mg isotopic ratios in giant stars of the globular cluster NGC 6752". In: *Astronomy & Astrophysics* 402 (May 2003), pp. 985–1001. DOI: 10.1051/0004-6361:20030296.

[39] A. I. Karakas et al. "The Uncertainties in the ^{22}Ne+$\alpha-$Capture Reaction Rates and the Production of the Heavy Magnesium Isotopes in Asymptotic Giant Branch Stars of Intermediate Mass". In: *The Astrophysical Journal* 643.1 (May 2006), pp. 471–483. ISSN: 1538-4357. DOI: 10.1086/502793.

[40] P. E. Koehler. "Constraints on the ^{22}Ne$(\alpha, n)^{25}$Mg s-process neutron source from analysis of ^{nat}Mg+n total and ^{25}Mg(n, γ) cross sections". In: *Phys. Rev. C* 66 (5 Nov. 2002), p. 055805. DOI: 10.1103/PhysRevC.66.055805.

[41] C. Angulo et al. "A compilation of charged-particle induced thermonuclear reaction rates". In: *Nuclear Physics A* 656.1 (Aug. 1999), pp. 3–183. DOI: 10.1016/S0375-9474(99)00030-5.

[42] J. José et al. "Nucleosynthesis in Classical Novae: CO versus ONe White Dwarfs". In: *Astrophysical Journal* 494.2 (Feb. 1998), pp. 680–690. DOI: 10.1086/305244.

[43] C. Iliadis et al. "Proton-induced Thermonuclear Reaction Rates for A = 20 - 40 Nuclei". In: *The Astrophysical Journal Supplement Series* 134.1 (May 2001), p. 151. DOI: 10.1086/320364.

[44] C. Iliadis et al. "Charged-particle thermonuclear reaction rates: III. Nuclear physics input". In: *Nuclear Physics A* 841 (Oct. 2010). DOI: 10.1016/j.nuclphysa.2010.04.010.

[45] L. Csedreki et al. "Characterization of the LUNA neutron detector array for the measurement of the ^{13}C$(\alpha, n)^{16}$O reaction". In: *Nuclear Instruments and Methods in Physics Research Section A: Accelerators, Spectrometers, Detectors and Associated Equipment* 994 (2021), p. 165081. ISSN: 0168-9002. DOI: 10.1016/j.nima.2021.165081.

[46] Z. Hu et al. "Measurements of cosmic ray induced background neutrons near the ground using a Bonner sphere spectrometer". In: *Nuclear Instruments and Methods in Physics Research Section A: Accelerators, Spectrometers, Detectors and Associated Equipment* 940 (2019), pp. 78–82. ISSN: 0168-9002. DOI: 10.1016/j.nima.2019.06.004.

[47] M. Shahmohammadi Beni et al. "Monte Carlo studies on neutron interactions in radiobiological experiments". In: *PLOS ONE* 12.7 (July 2017), pp. 1–17. DOI: 10.1371/journal.pone.0181281.

[48] P. Belli et al. "Deep underground neutron flux measurement with large BF3 counters". In: *Il Nuovo Cimento A* 101.6 (1989), pp. 959–966. DOI: 10.1007/bf02800162.

[49] G. Alimonti et al. "Ultra-low background measurements in a large volume underground detector". In: *Astroparticle Physics* 8.3 (1998), pp. 141–157. ISSN: 0927-6505. DOI: 10.1016/S0927-6505(97)00050-9.

[50] A. Best et al. "Study of the beam-induced neutron flux and required shielding for DIANA". In: *Nuclear Instruments and Methods in Physics Research Section A: Accelerators, Spectrometers, Detectors and Associated Equipment* 727 (2013), pp. 104–108. ISSN: 0168-9002. DOI: 10.1016/j.nima.2013.06.032.

[51] C. Massimi et al. "Neutron spectroscopy of ^{26}Mg states: Constraining the stellar neutron source ^{22}Ne$(\alpha, n)^{25}$Mg". In: *Physics Letters B* 768 (Feb. 2017). DOI: 10.1016/j.physletb.2017.02.025.

[52] V. Harms et al. "Properties of ^{22}Ne(α,n)^{25}Mg resonances". In: *Phys. Rev. C* 43 (6 June 1991), pp. 2849–2861. DOI: 10.1103/PhysRevC.43.2849.

[53] H. W. Drotleff et al. "New ^{22}Ne(α,n)^{25}Mg resonances at very low energies relevant for the astrophysical s-process". In: *Zeitschrift fur Physik A Hadrons and Nuclei* 338.3 (Sept. 1991), pp. 367–368. DOI: 10.1007/BF01288203.

[54] M. Jaeger et al. "^{22}Ne(α,n)^{25}Mg: The Key Neutron Source in Massive Stars". In: *Phys. Rev. Lett.* 87 (20 Oct. 2001), p. 202501. DOI: 10.1103/PhysRevLett.87.202501.

[55] A. Best et al. "Direct ^{13}C $(\alpha$,n)^{16}O Cross Section Measurement at Low Energies". In: *Nuclei in the Cosmos XV*. Vol. 219. Aug. 2019, pp. 215–218. DOI: 10.1007/978-3-030-13876-9_35.

[56] A. Best. "Scintillator-He3 Array for Deep-underground Experiments on the S-process". In: *ERC Starting Grant 2019 Research proposal - Grant agreement ID: 852016* (2019). DOI: 10.3030/852016.

[57] Shahina et al. "Direct measurement of the low-energy resonances in ^{22}Ne$(\alpha,\gamma)^{26}$Mg reaction". In: *Physical Review C* 106.2, 025805 (Aug. 2022), p. 025805. DOI: 10.1103/PhysRevC.106.025805.

[58] R. Talwar et al. "Probing astrophysically important states in the ^{26}Mg nucleus to study neutron sources for the s process". In: *Physical Review C* 93.5, 055803 (May 2016), p. 055803. DOI: 10.1103/PhysRevC.93.055803.

[59] R. Longland et al. "Reaction rates for the *s*-process neutron source ^{22}Ne + α". In: *Phys. Rev. C* 85 (6 June 2012), p. 065809. DOI: 10.1103/PhysRevC.85.065809.

[60]   Rapagnani, David et al. "Shades - ^{22}Ne(α,n)^{25}Mg reaction rate in the Gamow window". In: *EPJ Web Conf.* 260 (2022), p. 11031. DOI: 10.1051/epjconf/202226011031.

[61]   Piscitelli, Francesco et al. "Verification of He-3 proportional counters fast neutron sensitivity through a comparison with He-4 detectors - He-3 and He-4 proportional counters fast neutron sensitivity and evaluation of the cosmic neutron fluxes at ESS". In: *Eur. Phys. J. Plus* 135.7 (2020), p. 577. DOI: 10.1140/epjp/s13360-020-00600-8.

[62]   R. W. Stoughton et al. *Effective Cadmium Cutoff Energies.* Oak Ridge National Laboratory, Mar. 1960. DOI: 10.2172/4183816.

[63]   G. F. Ciani et al. "Direct Measurement of the ^{13}C(α,n)^{16}O Cross Section into the *s*-Process Gamow Peak". In: *Phys. Rev. Lett.* 127 (15 Oct. 2021), p. 152701. DOI: 10.1103/PhysRevLett.127.152701.

[64]   T. Langford et al. "Event identification in 3He proportional counters using risetime discrimination". In: *Nuclear Instruments and Methods in Physics Research Section A: Accelerators, Spectrometers, Detectors and Associated Equipment* 717 (2013), pp. 51–57. ISSN: 0168-9002. DOI: https://doi.org/10.1016/j.nima.2013.03.062.

[65]   G. F. Knoll. *Radiation detection and measurement.* John Wiley & Sons, 1979. URL: https://ui.adsabs.harvard.edu/abs/1979nyjw.book.....K.

[66]   A. Best et al. "Low energy neutron background in deep underground laboratories". In: *Nuclear Instruments and Methods in Physics Research, Section A: Accelerators, Spectrometers, Detectors and Associated Equipment* 812 (2016), pp. 1–6. DOI: 10.1016/j.nima.2015.12.034.

[67]   CAEN S.p.A. *UM5960 Compass User Manual - rev22.* URL: https://www.caen.it/products/compass/.

[68]   F. Brooks. "A scintillation counter with neutron and gamma-ray discriminators". In: *Nuclear Instruments and Methods* 4.3 (1959), pp. 151–163. ISSN: 0029-554X. DOI: 10.1016/0029-554X(59)90067-9.

[69]   D. Cester et al. "Experimental tests of the new plastic scintillator with pulse shape discrimination capabilities EJ-299-33". In: *Nuclear Instruments and Methods in Physics Research Section A: Accelerators, Spectrometers, Detectors and Associated Equipment* 735 (2014), pp. 202–206. ISSN: 0168-9002. DOI: 10.1016/j.nima.2013.09.031.

[70]   J. Heltsley et al. "Particle identification via pulse-shape discrimination with a charge-integrating ADC". In: *Nuclear Instruments and Methods in Physics Research Section A: Accelerators, Spectrometers, Detectors and Associated Equipment* 263.2 (1988), pp. 441–445. ISSN: 0168-9002. DOI: https://doi.org/10.1016/0168-9002(88)90984-9.

[71]   Y. Kaschuck et al. "Neutron/-ray digital pulse shape discrimination with organic scintillators". In: *Nuclear Instruments and Methods in Physics Research Section A: Accelerators, Spectrometers, Detectors and Associated Equipment* 551.2 (2005), pp. 420–428. ISSN: 0168-9002. DOI: https://doi.org/10.1016/j.nima.2005.05.071.

[72]   A. C. Olivieri et al. "Chapter 6 - Analytical Figures of Merit". In: *Practical Three-Way Calibration.* Boston: Elsevier, 2014, pp. 93–107. ISBN: 978-0-12-410408-2. DOI: 10.1016/B978-0-12-410408-2.00006-5.

[73] S. Marrone et al. "Pulse shape analysis of liquid scintillators for neutron studies". In: *Nuclear Instruments and Methods in Physics Research Section A: Accelerators, Spectrometers, Detectors and Associated Equipment* 490.1 (2002), pp. 299–307. ISSN: 0168-9002. DOI: https://doi.org/10.1016/S0168-9002(02)01063-X.

[74] S. Marrone. "A new method for signal acquisition and analysis in high radiation environment". In: *Nuclear Instruments and Methods in Physics Research Section B: Beam Interactions with Materials and Atoms* 213 (2004). 5th Topical Meeting on Industrial Radiation and Radioisotope Measurement Applications, pp. 246–249. ISSN: 0168-583X. DOI: https://doi.org/10.1016/S0168-583X(03)01597-0.

[75] D. Takaku et al. "Development of neutron-gamma discrimination technique using pattern-recognition method with digital signal processing". In: *Progress in Nuclear Science and Technology* 1 (2011), pp. 210–213. DOI: 10.15669/pnst.1.210.

[76] H. Sakai et al. "New pulse-shape analysis method with multi-shaping amplifiers". In: *Nuclear Instruments and Methods in Physics Research Section A: Accelerators, Spectrometers, Detectors and Associated Equipment* 421.1 (1999), pp. 316–321. ISSN: 0168-9002. DOI: https://doi.org/10.1016/S0168-9002(98)01259-5.

[77] J. Allison et al. "Recent developments in Geant4". In: *Nuclear Instruments and Methods in Physics Research Section A: Accelerators, Spectrometers, Detectors and Associated Equipment* 835 (2016), pp. 186–225. ISSN: 0168-9002. DOI: 10.1016/j.nima.2016.06.125.

[78] F. Potenza. "Monitoring and Maintenance of Customized Structures for Underground Environments: The Case of Gran Sasso National Laboratory". In: *Mechatronics for Cultural Heritage and Civil Engineering*. Ed. by E. Ottaviano et al. Cham: Springer International Publishing, 2018, pp. 357–373. ISBN: 978-3-319-68646-2. DOI: 10.1007/978-3-319-68646-2_16.

[79] A. Formicola et al. "The LUNA II 400kV accelerator". In: *Nuclear Instruments and Methods in Physics Research Section A: Accelerators, Spectrometers, Detectors and Associated Equipment* 507.3 (2003), pp. 609–616. ISSN: 0168-9002. DOI: 10.1016/S0168-9002(03)01435-9.

[80] S. Ahlen et al. "Study of penetrating cosmic ray muons and search for large scale anisotropies at the Gran Sasso Laboratory". In: *Physics Letters B* 249.1 (1990), pp. 149–156. ISSN: 0370-2693. DOI: 10.1016/0370-2693(90)90541-D.

[81] J. Balibrea-Correa et al. "Improved pulse shape discrimination for high pressure ^{3}He counters". In: *Nuclear Instruments and Methods in Physics Research Section A: Accelerators, Spectrometers, Detectors and Associated Equipment* 906 (2018), pp. 103–109. ISSN: 0168-9002. DOI: 10.1016/j.nima.2018.07.086.

[82] Y. Morishita et al. "Organic scintillator-based alpha/beta detector for radiological decontamination". In: *Nuclear Instruments and Methods in Physics Research Section A: Accelerators, Spectrometers, Detectors and Associated Equipment* 935 (2019), pp. 207–213. ISSN: 0168-9002. DOI: 10.1016/j.nima.2019.04.024.

[83]   J. Barton. "Studies with a low-background germanium detector in the Holborn Underground laboratory". In: *Nuclear Instruments and Methods in Physics Research Section A: Accelerators, Spectrometers, Detectors and Associated Equipment* 354.2 (1995), pp. 530–538. ISSN: 0168-9002. DOI: `10.1016/0168-9002(94)01068-4`.

[84]   G. Von Dardel. "A precision determination of the half-life of radium C'". In: *Physical Review* 79.4 (1950), pp. 734–735. DOI: `10.1103/PhysRev.79.734.2`.

[85]   R. Ballini. "Contribution à l'étude expérimentale de l'isomérie nucléaire". In: *Annales de Physique* 12.8 (June 1953), pp. 441–488. DOI: `10.1051/anphys/195312080441`.

[86]   K. W. Ogilvie. "The Half-value Period of Radium C'". In: *Proceedings of the Physical Society* 76.2 (Aug. 1960), p. 299. DOI: `10.1088/0370-1328/76/2/414`.

[87]   T. Dobrowolski et al. "The determination of the half-life of RaC' [6]". In: *Proceedings of the Physical Society* 77.6 (1961), pp. 1219–1220. DOI: `10.1088/0370-1328/77/6/121`.

[88]   A. Erlik et al. "Lifetime measurements of alpha emitters in the millisecond region". In: *Nuclear Instruments and Methods* 92.1 (1971), pp. 45–49. ISSN: 0029-554X. DOI: `10.1016/0029-554X(71)90221-7`.

[89]   J. Zhou et al. "Advances towards fast thermal detectors of intermediate mass with high resolution and large dynamic range". In: *Nuclear Instruments and Methods in Physics Research Section A: Accelerators, Spectrometers, Detectors and Associated Equipment* 335.3 (1993), pp. 443–452. ISSN: 0168-9002. DOI: `10.1016/0168-9002(93)91229-G`.

[90]   S. C. Wu. "Nuclear Data Sheets for A = 214". In: *Nuclear Data Sheets* 110.3 (2009), pp. 681–748. ISSN: 0090-3752. DOI: `10.1016/j.nds.2009.02.002`.

[91]   G. Suliman et al. "Measurements of the half-life of 214Po and 218Rn using digital electronics". In: *Applied Radiation and Isotopes* 70.9 (2012). Proceedings of the 18th International Conference on Radionuclide Metrology and its Applications, pp. 1907–1912. ISSN: 0969-8043. DOI: `10.1016/j.apradiso.2012.02.095`.

[92]   L. Miramonti et al. "Lifetimes of 214Po and 212Po measured with Counting Test Facility at Gran Sasso National Laboratory". In: *Journal of Environmental Radioactivity* 138 (2014), pp. 444–446. ISSN: 0265-931X. DOI: `10.1016/j.jenvrad.2014.02.025`.

[93]   C. Ananna et al. "Intrinsic background of EJ-309 liquid scintillator detectors". In: *Nuclear Instruments and Methods in Physics Research Section A: Accelerators, Spectrometers, Detectors and Associated Equipment* (2023), p. 169036. ISSN: 0168-9002. DOI: `10.1016/j.nima.2023.169036`.

[94]   J. S. Lee et al. "Pulse shaping analysis with LAB-based liquid scintillators". In: *Journal of the Korean Physical Society* 60.3 (Feb. 2012), pp. 554–557. DOI: `10.3938/jkps.60.554`.

[95]   E. Browne et al. "Nuclear Data Sheets for A = 234". In: *Nuclear Data Sheets* 108.3 (2007), pp. 681–772. ISSN: 0090-3752. DOI: `10.1016/j.nds.2007.02.003`.

[96] K. Abusaleem. "Nuclear Data Sheets for A=228". In: *Nuclear Data Sheets* 116 (2014), pp. 163–262. ISSN: 0090-3752. DOI: 10.1016/j.nds.2014.01.002.

[97] M. Kobayashi et al. "Analysis of Trace Elements in Aluminium by Neutron Activation". In: *Radioisotopes* 14.1 (1965), pp. 8–12. DOI: 10.3769/radioisotopes.14.8.

[98] K. Brodén et al. "Radioactivity in commercially available metals". In: *Radioactivity in commercially available metals*. Vol. 49. Nordisk kernesikkerhedsforskning, Dec. 2001, p. 19. URL: https://inis.iaea.org/collection/NCLCollectionStore/_Public/33/043/33043450.pdf?r=1.

[99] J. A. S. Adams et al. *Thorium, uranium and zirconium concentrations in bauxite*. Dec. 1960. DOI: 10.2113/gsecongeo.55.8.1653.

[100] C. Arpesella et al. "Measurements of extremely low radioactivity levels in BOREXINO". In: *Astroparticle Physics* 18.1 (2002), pp. 1–25. ISSN: 0927-6505. DOI: 10.1016/S0927-6505(01)00179-7.

[101] D. Leonard et al. "Systematic study of trace radioactive impurities in candidate construction materials for EXO-200". In: *Nuclear Instruments and Methods in Physics Research Section A: Accelerators, Spectrometers, Detectors and Associated Equipment* 591.3 (2008), pp. 490–509. ISSN: 0168-9002. DOI: 10.1016/j.nima.2008.03.001.

[102] Goethe Universtät - Frankfurt Am Main. *Experimental astrophysics tools list*. URL: https://exp-astro.de/index.php?id=tools&lang=en.

[103] CAEN S.p.A. *A1422 Low Noise Fast Rise Time Charge Sensitive Preamplifiers (Boxed)*. URL: https://www.caen.it/products/a1422/.

[104] A. O. Hanson et al. "Monoergic Neutrons from Charged Particle Reactions". In: *Rev. Mod. Phys.* 21 (4 Oct. 1949), pp. 635–650. DOI: 10.1103/RevModPhys.21.635.

[105] R. Reifarth et al. "PINO a tool for simulating neutron spectra resulting from the 7Li(p,n) reaction". In: *Nuclear Instruments and Methods in Physics Research Section A: Accelerators, Spectrometers, Detectors and Associated Equipment* 608.1 (2009), pp. 139–143. ISSN: 0168-9002. DOI: 10.1016/j.nima.2009.06.046.

[106] Goethe Universtät - Frankfurt Am Main. *FRANZ 0.1 VdG Energy Calibration*. URL: https://exp-astro.de/vdg_calib/.

[107] Brookhaven National Laboratory - National Nuclear Data Center (NNDC). *NuDat 3 database*. URL: https://www.nndc.bnl.gov/nudat3/.

[108] Scionix Holland B.V. *EJ-309 and EJ-309:B5 application note*. URL: https://scionix.nl/wp-content/uploads/2017/07/High-flashpoint-EJ-309-liquid-scintillation-detectors.pdf.

[109] F. Pino et al. "The light output and the detection efficiency of the liquid scintillator EJ-309". In: *Applied Radiation and Isotopes* 89 (2014), pp. 79–84. ISSN: 0969-8043. DOI: 10.1016/j.apradiso.2014.02.016.

[110] N. Kornilov et al. "Total Characterization of Neutron Detectors with a ^{252}Cf Source and a New Light Output Determination". In: *Nuclear instruments & methods in physics research section a-accelerators SP* 599.2-3 (2009), pp. 226–233. ISSN: 0168-9002. DOI: 10.1016/j.nima.2008.10.032.

[111] R. Katz et al. "Response of nuclear emulsions to ionizing radiations". In: *Nuclear Instruments and Methods* 130.1 (1975), pp. 105–119. ISSN: 0029-554X. DOI: 10.1016/0029-554X(75)90162-7.

[112] A. Enqvist et al. "Neutron light output response and resolution functions in EJ-309 liquid scintillation detectors". In: *Nuclear Instruments and Methods in Physics Research Section A: Accelerators, Spectrometers, Detectors and Associated Equipment* 715 (2013), pp. 79–86. ISSN: 0168-9002. DOI: 10.1016/j.nima.2013.03.032.

[113] M. Takada et al. "Simulated Neutron Response Functions of Phoswich-Type Neutron Detector and Thin Organic Liquid Scintillator". In: *Progress in Nuclear Science and Technology* 2 (Oct. 2011), pp. 274–279. DOI: 10.15669/pnst.2.274.

[114] M. A. Norsworthy et al. "Evaluation of neutron light output response functions in EJ-309 organic scintillators". In: *Nuclear Instruments and Methods in Physics Research Section A: Accelerators, Spectrometers, Detectors and Associated Equipment* 842 (2017), pp. 20–27. ISSN: 0168-9002. DOI: 10.1016/j.nima.2016.10.035.

[115] G. Mauri et al. "Fast neutron sensitivity for 3He detectors and comparison with Boron-10 based neutron detectors". In: *EPJ Techniques and Instrumentation* 6 (Dec. 2019). DOI: 10.1140/epjti/s40485-019-0052-x.